

**Spectral Energy Distributions, Dust, and Black Hole Properties: A Statistical,  
Multi-Wavelength Quasar Analysis**

A Thesis  
Submitted to the Faculty  
of  
Drexel University  
by  
Coleman M. Krawczyk  
in partial fulfillment of the  
requirements for the degree  
of  
Doctor of Philosophy  
September 2014

© Copyright 2014  
Coleman M. Krawczyk.

## Dedications

This thesis is dedicated to my family  
whose love and support made this work possible

## Acknowledgments

This work would not have been possible without the support of my advisor, Dr. Gordon Richards. His guidance helped to shape and provided much needed focus to my work. I would like to thank my dissertation committee of Dr. Michael Vogeley, Dr. David Goldberg, Dr. Adam Lidz, and Dr. Shyamalendu Bose for their support and insight throughout my research.

I would also like to thank my fellow graduate students for all the help and support they provided. During data analysis Micholas Smith and David Lioi spent countless hours listening to me talk about my research, helping me flesh out my ideas. And a special thinks to Erica Smith for proofreading all of my work and for encouraging me throughout my graduate work.

## Table of Contents

LIST OF TABLES . . . . .	vii
LIST OF FIGURES . . . . .	viii
ABSTRACT . . . . .	x
1. INTRODUCTION . . . . .	1
1.1 Accretion Disk . . . . .	1
1.1.1 $\alpha$ -Disk Model . . . . .	2
1.1.2 Eddington Luminosity . . . . .	2
1.2 Spectral Energy Distributions . . . . .	3
1.3 Dust Reddening . . . . .	4
1.4 Black Hole Masses . . . . .	6
1.5 Outline . . . . .	7
2. DATA . . . . .	8
2.1 Near-Infrared . . . . .	8
2.2 Mid-Infrared . . . . .	10
2.3 Ultraviolet . . . . .	11
2.4 X-Ray . . . . .	12
2.5 The Dust Reddening Sample . . . . .	13
2.6 Black Hole Masses . . . . .	15
3. MULTI-WAVELENGTH SEDs . . . . .	17
3.1 Corrections . . . . .	17
3.1.1 Lyman Forest and Limit . . . . .	17
3.1.2 Emission Lines . . . . .	18
3.1.3 Host Galaxy . . . . .	20
3.1.4 Gap Repair . . . . .	21

3.2	Mean SEDs . . . . .	22
3.2.1	Overall Mean SED . . . . .	22
3.2.2	Sub-sampled Mean SEDs . . . . .	25
3.3	Bolometric Corrections . . . . .	32
3.3.1	Limits of Integration . . . . .	32
3.3.2	Normalization Wavelength . . . . .	33
3.3.3	Integrated Luminosities and Bolometric Corrections . . . . .	33
3.4	Discussion: The Unseen EUV Continuum . . . . .	37
3.5	Conclusions . . . . .	40
4.	DUSTY QUASARS . . . . .	42
4.1	Fitting Reddening Models to Quasar Photometry . . . . .	42
4.1.1	Modal Colors . . . . .	42
4.1.2	Red vs. Reddened: Photometry . . . . .	44
4.1.3	Monte Carlo Parameter Estimation . . . . .	47
4.1.4	MCMC Results: Population Parameters . . . . .	47
4.1.5	MCMC Results: Individual Parameters . . . . .	51
4.1.6	What Reddening Law Fits Better? . . . . .	55
4.2	Composite Spectra . . . . .	56
4.2.1	Red vs. Reddened: Spectra . . . . .	57
4.2.2	Individual Lines . . . . .	57
4.3	Conclusions . . . . .	62
5.	TRENDS WITH BLACK HOLE PROPERTIES . . . . .	64
5.1	Dust Corrected Mean SEDs . . . . .	64
5.1.1	Applying Dust Corrections . . . . .	66
5.1.2	A Uniform Sample . . . . .	67
5.1.3	Extinction Corrected SEDs . . . . .	68
5.2	SEDs Based on $M_{\text{BH}}$ and $L/L_{\text{Edd}}$ . . . . .	71

5.3	Conclusions . . . . .	73
6.	CONCLUSIONS . . . . .	75
	BIBLIOGRAPHY . . . . .	77
	APPENDIX A: BAYESIAN MODEL . . . . .	83
A.1	Gibbs Sampling . . . . .	83
A.2	The Model . . . . .	84
A.3	Conditional Likelihoods . . . . .	85
	VITA . . . . .	88

## List of Tables

2.1	Quasar Catalog Format . . . . .	11
3.1	Mean Quasar SEDs . . . . .	25
3.2	Bolometric Luminosities and Bolometric Corrections . . . . .	33
4.1	Hyperparameter Fit Values . . . . .	50
4.2	Individual Fit Values . . . . .	52
4.3	Reddening Law Comparison . . . . .	56

## List of Figures

2.1	Matched survey footprints . . . . .	9
2.2	Luminosity vs. redshift . . . . .	10
2.3	2MASS vs. UKIDSS . . . . .	12
2.4	<i>WISE</i> matching radius . . . . .	13
2.5	Filter position vs. redshift . . . . .	14
2.6	$M_{\text{BH}}$ vs. Redshift . . . . .	15
3.1	Lyman series extinction . . . . .	18
3.2	Model quasar spectrum . . . . .	19
3.3	Mock photometry . . . . .	20
3.4	Uncorrected mean SED . . . . .	23
3.5	Gap filling SED . . . . .	24
3.6	Corrected mean SED . . . . .	26
3.7	Luminosity distribution of non-reddened quasars . . . . .	27
3.8	Luminosity dependent SEDs . . . . .	28
3.9	Expanded normalized SEDs . . . . .	30
3.10	C IV-dependent SEDs . . . . .	31
3.11	Bolometric correction vs. luminosity . . . . .	35
3.12	Bolometric correction dependent SEDs . . . . .	36
3.13	EUV models . . . . .	38
3.14	Mean EUV SEDs and bolometric corrections for each model . . . . .	39
4.1	Colors vs. redshift . . . . .	43
4.2	Relative colors . . . . .	44
4.3	Dust extinction curves . . . . .	45
4.4	$c_1$ vs. $c_2$ . . . . .	46

4.5	Best fit population parameters for non-BAL quasars . . . . .	48
4.6	Best fit population parameters for BAL quasars . . . . .	49
4.7	$c_1$ vs. $c_2$ for MC sample of non-BAL quasars . . . . .	51
4.8	Joint probability distribution of $2.5\Delta(\alpha_\lambda)$ and $E(B - V)$ . . . . .	53
4.9	Joint probability distribution of $2.5\Delta(\alpha_\lambda)$ and $E(B - V)$ . . . . .	54
4.10	BAL fraction . . . . .	55
4.11	Composite spectra for non-BAL quasars . . . . .	58
4.12	Composite spectra for BAL quasars . . . . .	59
4.13	Expanded emission-line regions for non-BAL quasars . . . . .	60
4.14	Expanded emission-line regions for BAL quasars . . . . .	62
5.1	Mean SEDs grouped by color . . . . .	65
5.2	Mean SEDs grouped by dust . . . . .	66
5.3	Typical reddening correction . . . . .	67
5.4	Luminosity vs. redshift . . . . .	68
5.5	Mean corrected SEDs grouped by dust and color . . . . .	69
5.6	$L_{2500 \text{ \AA}}$ and $BC_{2500 \text{ \AA}}$ distributions grouped by dust and color . . . . .	70
5.7	Mean SEDs grouped by $M_{\text{BH}}$ . . . . .	71
5.8	Mean SEDs grouped by $L/L_{\text{Edd}}$ . . . . .	72
5.9	$L_{2500 \text{ \AA}}$ and $BC_{2500 \text{ \AA}}$ distributions grouped by $M_{\text{BH}}$ and $L/L_{\text{Edd}}$ . . . . .	73

## Abstract

Spectral Energy Distributions, Dust, and Black Hole Properties: A Statistical, Multi-Wavelength  
Quasar Analysis  
Coleman M. Krawczyk  
Advisor: Dr. Gordon Richards

We explore the mid-infrared (mid-IR) through ultraviolet (UV) spectral energy distributions (SEDs) of 119,652 luminous type 1 quasars with  $0.064 < z < 5.46$  using mid-IR data from *Spitzer* and *WISE*, near-infrared data from 2MASS and UKIDSS, optical data from SDSS and UV data from *GALEX*. The mean SED requires a bolometric correction of  $BC_{2500\text{ \AA}} = 2.75 \pm 0.40$  using the integrated light from  $1\text{ }\mu\text{m}$ – $2\text{ keV}$ . We investigate the mean SED dependence on various parameters, particularly the UV luminosity for quasars with  $0.5 \lesssim z \lesssim 3$ . Low-luminosity SEDs exhibit a bluer far-UV spectral slope, a redder optical continuum, and less hot dust. Our work suggests that lower-luminosity quasars may require an extra continuum component in the unseen extreme-UV that is weak in high-luminosity quasars. As such, we consider four possible models and explore the resulting BCs.

Taking a subset of  $\sim 35,000$  uniformly selected quasars we explore their extinction/reddening in order to better understand their *intrinsic* SEDs. Using optical–UV photometry, we isolate outliers in the color distribution and find them well described by an SMC-like reddening law. A hierarchical Bayesian model was used to find distributions of powerlaw indices and  $E(B - V)$  consistent with both the broad absorption line (BAL) and non-BAL samples. 2.5% (13%) of the non-BAL (BAL) sample are shown to be consistent with  $E(B - V) > 0.1$  and 0.1% (1.3%) with  $E(B - V) > 0.2$ . Simulations show both populations of quasars are intrinsically bluer than the mean composite, with a mean spectral index ( $\alpha_\lambda$ ) of -1.79 (-1.83). The emission and absorption-line properties of both samples showed that quasars with intrinsically red continua have weaker Balmer lines and stronger ionizing spectral lines, the latter indicating a harder continuum in the extreme-UV.

Applying corrections for associated dust, we better determine the *intrinsic* SEDs and true BCs for our uniformly selected subsample. The SEDs with the most dust extinction are intrinsically brighter and showed more dust emission near  $\sim 10\text{ }\mu\text{m}$  than the SEDs with less extinction. The bluer SEDs have more hot dust emission and higher BCs, consistent with having hotter accretions disks and/or being viewed closer to edge-on. Mean SEDs were also made based on the black hole mass ( $M_{\text{BH}}$ ) and the Eddington fraction ( $L/L_{\text{Edd}}$ ). Quasars with large  $L/L_{\text{Edd}}$  and/or large  $M_{\text{BH}}$  have more hot dust and a bluer optical continua, both consistent with a hotter accretion disk.





## Chapter 1: Introduction

Most massive (bulge-dominated) galaxies are believed to harbor a supermassive black hole at their centers (Kormendy & Richstone, 1995). For the most part, these black holes are passive, but when the host galaxy's gas loses angular momentum it accretes onto the black hole, creating a luminous quasar (Lynden-Bell, 1969). This gas can be disrupted in a number of ways, including galaxy mergers (e.g. Kauffmann & Haehnelt, 2000; Hopkins et al., 2006) and secular fueling (e.g. Hopkins & Hernquist, 2009, and references therein). Most of the energy output is due to an accretion disk that forms about the black hole which either directly or indirectly produces radiation across nearly the entire electromagnetic spectrum (EM) (Elvis et al., 1994). As a result of the quasar process, some of the energy is “fed back” into the galaxy, possibly disrupting the galaxy’s gas supply (Silk & Rees, 1998; Fabian, 1999) and quenching accretion of matter onto the black hole itself (e.g., Di Matteo et al., 2005; Djorgovski et al., 2008).

The basic structure of a quasar is as follows (e.g. Antonucci, 1993; Urry & Padovani, 1995; Krolik, 1999; Heckman & Best, 2014). Directly surrounding the central supermassive black hole is a geometrically-thin, optically-thick accretion disk. A radial temperature gradient within this disk results in thermal continuum emission in the optical through ultraviolet. Surrounding this accretion disk is a hot corona which can Compton-up-scatter the continuum light into the X-ray regime. On scales of light-days to light-years a population of dense gas clouds are photo-ionized by this radiation. These gas clouds have large velocity dispersions (several thousand km s<sup>-1</sup>) leading broad emission lines.

Moving out further from the central black hole there is a region with large amount of obscuring material usually referred to as the dusty torus (Krolik & Begelman, 1988; Pier & Krolik, 1992; Krolik, 1999; Beckmann & Shrader, 2012). The inner edge of this region is set by the sublimation temperature of the dust. As the light from the accretion disk passes through this dust it is absorbed and reemitted as thermal radiation in the near- and mid-infrared. On the scales of a few hundred to a few thousand pc there is a population of lower density and lower velocity gas clouds. As the ionizing radiation from the inner regions of the quasar passes, it photo-ionizes this gas, producing narrow emission lines. In some quasars, powerful jets are produced along the polar direction of the accretion disk, leading to synchrotron emission visible at radio wavelengths.

### 1.1 Accretion Disk

Once the gas around the black hole has a mechanism for losing angular momentum, the gas will form an accretion disk as it falls into the black hole. Due to differential rotation within this accretion disk, there is friction within the gas, causing it to heat up and radiate strongly in the optical and ultraviolet. One of the most basic models for the accretion disk is the  $\alpha$ -disk model originally developed by Shakura & Sunyaev (1973).

### 1.1.1 $\alpha$ -Disk Model

The  $\alpha$ -disk model is a model for an optically-thick, geometrically-thin accretion disk. This model assumes that the angular momentum of the in-falling material is removed from the disk through a viscosity term  $\alpha$ <sup>1</sup>. For this model, Shakura & Sunyaev (1973) found the radius dependent temperature profile for the accretion disk is:

$$kT \propto \left( \frac{M_{\text{BH}}}{M_{\odot}} \right)^{-1/4} \left( \frac{\dot{M}}{\dot{M}_{\text{Edd}}} \right)^{1/4} R^{-3/4} \quad (1.1)$$

where  $M_{\text{BH}}$  is the mass of the central black hole,  $M_{\odot}$  is the mass of the Sun,  $\dot{M}$  is the accretion rate,  $\dot{M}_{\text{Edd}}$  is the Eddington accretion rate (see Equation 1.10), and  $R$  is the distance to the central black hole. Assuming each portion of the accretion disk radiates locally like a blackbody, the monochromatic luminosity can be written as:

$$L_{\nu} = \frac{8\pi h\nu^3}{c^2} \int_{R_0}^{R_1} \frac{R dR}{e^x - 1} \quad (1.2)$$

where  $x = h\nu/kT$ ,  $R_0$  is the inner edge of the accretion disk, and  $R_1$  is the outer edge. Taking the limit where  $h\nu \ll kT$ :

$$L_{\nu} \propto \nu^{1/3}. \quad (1.3)$$

This would correspond to a  $g - i$  color of -0.17, whereas the typical quasar has a  $g - i$  color of 0.23, redder than this prediction. When  $h\nu \gg kT$  the luminosity falls off exponentially. In §4.1.5 we will explore both the observed and intrinsic colors in comparison with this model.

### 1.1.2 Eddington Luminosity

The Eddington luminosity ( $L_{\text{Edd}}$ ) is the point where the radiation pressure produced by the quasar balances the inward gravitational force caused by the central black hole (Rybicki & Lightman, 1986). At this point, the in-falling material is in hydrostatic equilibrium and the acceleration is zero:

$$\frac{du}{dt} = -\frac{\nabla p}{\rho} - \nabla \Phi = 0 \quad (1.4)$$

where  $u$  is the velocity,  $p$  is the pressure,  $\rho$  is the density, and  $\Phi$  is the gravitational potential. For a quasar, the pressure is dominated by radiation pressure associated with a radiation flux  $F_{\text{rad}}$  (e.g. Stern et al., 2014):

$$-\frac{\nabla p}{\rho} = \frac{\kappa}{c} F_{\text{rad}} \quad (1.5)$$

where  $\kappa$  is the opacity of the accreting material, and  $c$  is the speed of light. The luminosity of a source bounded by the surface  $S$  is

$$L_{\text{Edd}} = \int_S F_{\text{rad}} \cdot dS = \int_S \frac{c}{\kappa} \nabla \Phi \cdot dS, \quad (1.6)$$

---

<sup>1</sup>All the derived quantities in this model are only weakly dependent on  $\alpha$  and its exact value is unimportant.

where the second equality comes from Equation 1.4. Assuming the opacity is constant over the surface and using the divergence theorem and Poisson's equation:

$$L_{\text{Edd}} = \frac{c}{\kappa} \int_V \nabla^2 \Phi dV = \frac{4\pi Gc}{\kappa} \int_V \rho dV = \frac{4\pi GM_{\text{BH}}c}{\kappa}. \quad (1.7)$$

Assuming the accreting material is made up of pure ionized hydrogen, this luminosity becomes (Rybicki & Lightman, 1986):

$$L_{\text{Edd}} = \frac{4\pi GM_{\text{BH}}m_p c}{\sigma_T} \simeq 1.23 \times 10^{38} \frac{\text{erg}}{\text{s}} \left( \frac{M_{\text{BH}}}{M_\odot} \right) \quad (1.8)$$

where  $m_p$  is the mass of the proton and  $\sigma_T$  is the Thomson scattering cross-section.

Assuming the matter in the accretion disk has a constant accretion rate at all radii, the luminosity is given by:

$$L = \eta \dot{M} c^2. \quad (1.9)$$

where  $\eta$  is the efficiency for the accretion process converting mass into energy<sup>2</sup>. Combining this equation with Equation 1.8 we can define  $\dot{M}_{\text{Edd}}$  as

$$\dot{M}_{\text{Edd}} = \frac{L_{\text{Edd}}}{\eta c^2} \simeq \frac{2.17 \times 10^{-9}}{\eta} \frac{M_\odot}{\text{year}} \left( \frac{M_{\text{BH}}}{M_\odot} \right) \quad (1.10)$$

Combining Equations 1.10 and 1.9 we get the relation:

$$\frac{L}{L_{\text{Edd}}} = \frac{\dot{M}}{\dot{M}_{\text{Edd}}} \quad (1.11)$$

This final relation allows the for the accretion rate to be estimated using the observable quantities  $L$  and  $M_{\text{BH}}$ , a property we will take advantage of in Chapter 5.

## 1.2 Spectral Energy Distributions

As seen in §1.1, accretion disk models make predictions based on  $\dot{M}$  or, using Equation 1.11, based on the observable (bolometric) luminosity,  $L_{\text{bol}}$ , while what can be measured is usually the monochromatic luminosity,  $L_\lambda$ <sup>3</sup>. The bolometric luminosity is given by the integrated area under the full spectral energy distribution (SED). The ratio between  $L_{\text{bol}}$  and  $L_\lambda$  defines a “bolometric correction,” which can be applied generically if there is reason to believe that the quasar SED is well-known (if not well-measured for an individual object). Currently the best quasar SEDs are based on only tens or hundreds of bright quasars (Elvis et al., 1994; Richards et al., 2006a). However, over 100,000 luminous broad-line quasars have been spectroscopically confirmed (Schneider et al., 2010). As it is dangerous to assume that we can extrapolate the results from a few hundred of the brightest quasars to the whole population, it is important to expand our knowledge to cover the full quasar sample.

While Elvis et al. (1994) and Richards et al. (2006a) provide the most complete SEDs in terms of number of objects and overall wavelength coverage, further understanding of the SED comes from

---

<sup>2</sup> $\eta$  is dependent on the spin ( $a$ ) of the black hole and can take on values from 0.06 up to 0.4.

<sup>3</sup> $\nu L_\nu = \lambda L_\lambda$

a variety of other investigations from both spectroscopy and multi-wavelength imaging across the EM spectrum. For example, composite SEDs, from the radio to the X-ray, for 85 optically and radio selected bright quasars ( $\log(\nu L_\nu) |_{\lambda=3000\text{\AA}} \geq 44$ ) with  $z < 1.5$  were made by Shang et al. (2011), and the bolometric corrections for this sample were tabulated by Runnoe et al. (2012). Stern & Laor (2012) construct SEDs for over 3500 low-z ( $z < 0.2$ ) type 1 active galactic nucleus (AGN) with broad H $\alpha$  lines ranging from the near-infrared (near-IR) up to the X-ray with  $\log(\nu L_\nu) |_{\lambda=2500\text{\AA}} \geq 42$ , while Assef et al. (2010) present SEDs using over 5300 AGNs spanning the mid-infrared (mid-IR) up to the X-ray, with redshift going up to  $\sim 5.6$ , from the AGN and Galaxy Evolution Survey (AGES; Kochanek et al., 2012). In the mid-IR, Deo et al. (2011) produced a composite spectrum using 25 luminous type 1 quasars at  $z \sim 2$ .

Vanden Berk et al. (2001) used 2200 Sloan Digital Sky Survey (SDSS) spectra in the redshift range of  $0.04 < z < 4.79$  to construct a mean quasar spectrum covering wavelengths from 800 $\text{\AA}$  to 8555 $\text{\AA}$  in the rest frame. From this they found that the mean UV continuum is roughly a powerlaw with  $\alpha_\nu = -0.44$  ( $f_\nu \propto \nu^\alpha$ ). To explore the far-UV (FUV) region of the quasar spectrum, Telfer et al. (2002) used  $\sim 330$  *Hubble Space Telescope* spectra of 184 quasars, with  $z > 0.33$ , covering rest frame wavelengths from 500 $\text{\AA}$  to 1200 $\text{\AA}$ , and found an anti-correlation between the spectral index of the FUV ( $\alpha_{\text{FUV}}$ ) and the luminosity at 2500 $\text{\AA}$ . This work was later supplemented at lower redshift and lower luminosity by Scott et al. (2004), who used 100 *FUSE* spectra covering the FUV. By combining their data with that from Telfer et al. (2002), they found an anti-correlation that can be characterized by

$$\alpha_{\text{FUV}} = 21.02 - 0.49 \log \left( \frac{\lambda_{1100\text{\AA}} \circ L_{1100\text{\AA}}}{\text{erg s}^{-1}} \right). \quad (1.12)$$

At shorter wavelengths, using 73 quasars, Avni & Tananbaum (1982) found a dependency of the spectral index between the optical and the X-ray and a quasar's luminosity. This relation was further studied by a number of authors, including Steffen et al. (2006), who used 333 quasars with  $z < 6$  and  $\log(\nu L_\nu) |_{\lambda=2500\text{\AA}} \geq 42$ , to find the relationship between the UV and X-ray luminosities to be:

$$\log(L_{\text{2keV}}) = (0.721 \pm 0.011) \log(L_{2500\text{\AA}}) + (4.531 \pm 0.688), \quad (1.13)$$

while Just et al. (2007) have extended this result to higher luminosities. Recently, Lusso et al. (2010) completed a similar study using 545 X-ray selected quasars and found a similar relationship. In the X-ray regime, the mean SED appears to have  $\alpha_\nu \sim -1$  (e.g., George et al., 2000) before cutting off at  $\sim 500$  keV (Zdziarski et al., 1995). These relations allow us to extend our SEDs into the X-ray when our data lacks coverage at those wavelengths.

### 1.3 Dust Reddening

In the unification model for quasars (Antonucci, 1993; Urry & Padovani, 1995) there is a large amount of obscuring material (usually referred to as the dust torus) around the accretion disk that can block the light emitted from the accretion disk along certain lines of sight. As its name suggests, this area is filled with dust, small particles that condense out of the interstellar gas in galaxies. When light passes through this dust it not only dims the intensity but also reddens it (Trumpler, 1930;

Pei, 1992; Goobar, 2008). These processes happen for two reasons: first, dust scatters some photons out of the line of sight, and second, the dust absorbs some photons, converting their energy into heat. This second process preferentially absorbs photons of shorter wavelengths since dust grains are effective absorbers of photons with wavelengths smaller than the characteristic size of the dust grains. As the dust heats up it reradiates these photons in the infrared (IR), causing the observed light to be redder after passing through the dust (Binney & Merrifield, 1998).

Extinction is the combination of both scattering and absorption. The standard notation for the extinction of an object in the  $X$ -band magnitude is:

$$A_X = (m - m_0)_X \quad (1.14)$$

where  $m$  is the observed magnitude and  $m_0$  is the magnitude that would be observed in the absence of extinction. The color excess or reddening in the  $X - Y$  color is defined to be:

$$E(X - Y) = A_X - A_Y. \quad (1.15)$$

The normalized extinction is given by:

$$R_X = \frac{A_X}{E(B - V)} \quad (1.16)$$

In the literature the most commonly cited extinction is  $A_V$ , the most cited color excess is  $E(B - V)$ , and the most cited normalized extinction is  $R_V$ . The value of  $R_V$  is related to the size of the dust grains such that large dust grains have higher values of  $R_V$  (Draine, 2003).

For distant quasars, several mechanisms contribute to extinction: the Milky Way, galaxies along the line of sight, the quasar host galaxy, and the nuclear region itself. While it is relatively straightforward to correct for and/or mitigate against the first two sources of reddening, it can be quite difficult to disentangle the last two sources and to properly isolate the effects of reddening from intrinsic differences in the spectral energy distribution (SED). Indeed, quasars can appear “red” (or rather, redder than average) both because they are intrinsically red or because of dust reddening (Richards et al., 2003).

Quasar SEDs between the UV and near-IR are generally described by a modified black body (Shakura & Sunyaev, 1973) which is produced by an accretion disk with a range of temperatures. At wavelengths which start to sample the high-temperature limit of the accretion disk, the SED begins to “turn over,” following the Wien part of the distribution. The location of this turnover is likely a function of luminosity (e.g., Brotherton & Francis, 1999; Scott et al., 2004). At longer wavelengths, contamination from the host galaxy itself can make the intrinsic contribution of the central engine difficult to measure. Once the host galaxy contribution is accounted for, it is generally found that, between the rest-frame wavelengths of  $1\,\mu\text{m}$  and  $1216\,\text{\AA}$ , a quasar’s continuum can be roughly approximated as a powerlaw (e.g., Vanden Berk et al., 2001; Richards et al., 2006a; Krawczyk et al., 2013). However, if there are significant amounts of dust associated with the quasar, then the continuum will take on the form:

$$L_{\lambda, \text{rest}} \propto \lambda^{\alpha_\lambda} e^{-\tau_\lambda} \propto \lambda^{\alpha_\lambda} 10^{-E(B-V)R_\lambda/2.5} \quad (1.17)$$

where  $L_{\lambda,\text{rest}}$  is the rest frame luminosity,  $\alpha_\lambda$  is the intrinsic spectral index,  $\tau_\lambda$  is the optical depth of the dust, and  $R_\lambda$  is a function that is dependent on the physical properties of the dust. For small amounts of dust reddening, the SED will simply appear to have a “steeper” (redder) powerlaw. For larger amounts of reddening, noticeable curvature can be seen. In §4.1.2 we use this curvature as an indicator for the type of dust present in quasars.

Deviations from the mean quasar SED have been used previously to define red quasar samples, including Gregg et al. (2002) who used an optical-infrared spectral index of  $\alpha < -1$  as their defining property. Very dust reddened quasars can be difficult to identify in optical surveys, both because of their redder than average color (often similar to stellar colors) and the corresponding extinction. Radio and infrared selection (e.g., Gregg et al., 2002; Glikman et al., 2007) help to overcome this. These studies suggest that a significant portion ( $> 25\%$ ) of the underlying quasar population is dust reddened (yet still classified as Type 1 by virtue of having broad emission lines).

The ability to identify the nature of any dust reddening, determine the magnitude of the effect, and correct for it is important for a number of reasons, for example, determining the true spectral index and optical luminosity of the quasars and, more importantly, to determine the *bolometric* luminosity of the quasar (as done in Chapter 5). This value is crucial for making comparisons between quasars photometered at different rest-frame wavelengths, the extreme example being comparisons of unobscured (type 1) and obscured (type 2) quasars (e.g., Zakamska et al., 2003; Merloni et al., 2014), where the luminosity of the latter must be measured not in the optical/UV continuum, but instead from narrow emission lines, the IR or X-ray. Accurate bolometric luminosities are also needed for accurate estimates of the accretion rate and the Eddington ratio,  $L_{\text{Bol}}/L_{\text{Edd}}$  (see Equation 1.11). Thus proper determination of the SED provides a powerful link from observed properties to the parameters of accretion disk physics: mass, accretion rate, and spin (Shakura & Sunyaev, 1973; Hubeny & Hubeny, 1997).

## 1.4 Black Hole Masses

Quasars are known to be highly variable in luminosity. Due to the large distance between the accretion disk and the broad line region (BLR) there is an observable time lag between the variability in the continuum and the variability in the broad emission lines. Combining this time lag with the speed of light gives a measure of the distance ( $R_{\text{BLR}}$ ) between the central black hole and the BLR. Assuming the BLR is in virial equilibrium and the velocity dispersion of the BLR can be estimated from the width of the broad spectral lines ( $\Delta V$ ), the black hole mass can be estimated:

$$M_{\text{BH}} = f \left( \frac{R_{\text{BLR}} \Delta V^2}{G} \right) \quad (1.18)$$

where  $f$  is a dimensionless number that is dependent on the geometry of the system, and  $G$  is the gravitational constant. This process for estimating  $M_{\text{BH}}$  is called reverberation mapping (RM). Although  $f$  can't be measured directly, an ensemble average,  $\langle f \rangle$ , can be found empirically under the assumption that active galaxies have the same  $M_{\text{BH}}-\sigma_*$  relation as local inactive galaxies (e.g. Onken et al., 2004; Woo et al., 2010, 2013; Graham et al., 2011; Park et al., 2012).

Unfortunately, there are only a small number ( $\sim 50$ ) of quasars with RM data. In order to

measure black hole masses for a larger number of quasars, various scaling relations have been found for other observables that are correlated with  $M_{\text{BH}}$  in the RM sample. In particular,  $R_{\text{BLR}}$  correlates well with luminosity (e.g. Kaspi et al., 2000, 2005; Bentz et al., 2006, 2009, 2013):

$$R_{\text{BLR}} \propto (\lambda L_{\lambda})^{\alpha} \quad (1.19)$$

where  $\alpha$  has been found to be  $0.533^{+0.035}_{-0.033}$  when using the H $\beta$  line for calibration (Bentz et al., 2013).

By replacing  $R_{\text{BLR}}$  in Equation 1.18 with luminosity via Equation 1.19 and using a spectral line's FWHM for  $\Delta V$ , several studies (e.g. McLure & Dunlop, 2004; Vestergaard & Peterson, 2006; Vestergaard & Osmer, 2009) have found scaling relations for  $M_{\text{BH}}$  of the form:

$$\log \left( \frac{M_{\text{BH}}}{M_{\odot}} \right) = a + b \log \left( \frac{\lambda L_{\lambda}}{10^{44} \text{ erg s}^{-1}} \right) + 2 \log \left( \frac{\text{FWHM}}{\text{km s}^{-1}} \right) \quad (1.20)$$

where FWHM is the full width at half maximum for either H $\beta$ , Mg II, or C IV. The relation for H $\beta$  is directly calibrated off of the RM data via Equation 1.19, but due to a lack of RM data for either Mg II or C IV, these relations are calibrated using H $\beta$  masses under the assumption that every line estimator should produce the same result.

Although the FWHM is the most commonly used value for  $\Delta V$  (since it is more robust against noise in the spectra) it has been shown to produce biased masses (Wang et al., 2009; Rafiee & Hall, 2011; Peterson, 2011; Denney, 2012; Denney et al., 2013; Park et al., 2013). Masses calculated using the line dispersion ( $\sigma_{\text{line}}$ ) tend to be more accurate and produce less scatter when compared to the RM masses. To address this concern, Wang et al. (2009) parameterized  $\Delta V^2 \propto \text{FWHM}^{\gamma}$ , essentially changing the 2 on the last term of Equation 1.20 into a free parameter  $\gamma$ :

$$\log \left( \frac{M_{\text{BH}}}{M_{\odot}} \right) = a + b \log \left( \frac{\lambda L_{\lambda}}{10^{44} \text{ erg s}^{-1}} \right) + \gamma \log \left( \frac{\text{FWHM}}{1000 \text{ km s}^{-1}} \right) \quad (1.21)$$

This parameterization has recently been used by Rafiee & Hall (2011) and Park et al. (2013) to update the scaling relations for the Mg II and C IV mass estimates respectively.

## 1.5 Outline

This thesis is structured as follows. The data used for this analysis are presented in Chapter 2. After introducing the corrections and data analysis methods, Chapter 3 presents our findings for individual and mean bolometric corrections. Chapter 4 presents our methods and findings for estimating dust reddening associated with a subset of our quasars. The statistical methods used in this chapter are outlined in more detail in Appendix A. In Chapter 5, we apply the corrections from Chapter 4 to our SEDs and use estimated black hole masses to study changes in the SEDs with the properties of the central black hole. Finally, we present our conclusions in Chapter 6. Throughout this work we use a  $\Lambda$ CDM cosmology with  $H_0 = 71 \text{ km s}^{-1} \text{ Mpc}^{-1}$ ,  $\Omega_{\Lambda} = 0.734$ , and  $\Omega_m = 0.266$ , consistent with the *Wilkinson Microwave Anisotropy Probe 7* cosmology (Jarosik et al., 2011).

## Chapter 2: Data

Our sample starts with the SDSS-DR7 quasar catalog by Schneider et al. (2010), containing 105,783 spectroscopically confirmed broad-lined quasars. Each quasar has photometric data in the five SDSS optical bandpasses  $ugriz$  (Fukugita et al., 1996). Only quasars that have nonzero flux in all five SDSS bandpasses after correcting for Galactic extinction have been kept in our catalog, bringing the sample size to 103,895. While the SDSS survey covers a large area of sky, it is limited to relatively bright quasars ( $i < 19.1$  for  $z < 3$  and  $i < 20.2$  for  $z > 3$ ). As such, in addition to these quasars, we included 15,757 lower luminosity, optically-selected quasars taken from the Two Degree Field QSO Redshift survey (2QZ;  $b_J < 20.85$  for  $z < 3$ ; Croom et al., 2004), the Two Degree Field-SDSS LRG and QSO survey (2SLAQ;  $g < 21.85$  for  $z < 3$ ; Croom et al., 2009), and the AAT-UKIDSS-SDSS survey (AUS;  $i < 21.6$  for  $0 < z < 5$ ; Croom et al., in preparation). In the rest frame, we have over 70,000 QSOs with  $\log(\nu[\text{Hz}])$  ranging from  $\sim 13.7$ – $15.4$  ( $\lambda \sim 1200 \text{ \AA}$ – $6 \mu\text{m}$ ) and at least 10,000 QSOs covering the range from  $\sim 13.3$ – $15.6$  ( $\lambda \sim 750 \text{ \AA}$ – $15 \mu\text{m}$ ). All SDSS magnitudes have been corrected for Galactic extinction according to Schlegel et al. (1998) with corrections to the extinction coefficients as given by Schlafly & Finkbeiner (2011). Table 2.1 presents the IR–UV photometry for the 119,652 quasars in our sample. Signs of dust reddening are seen in 11,468 of these, specifically with a color excess  $\Delta(g - i) > 0.3$  (Richards et al., 2003). In Chapter 3, these have been excluded from our analysis, bringing our final sample size to 108,184. However, in Chapter 4, we explicitly study the dust reddening properties of quasars, so these objects are added back into the sample. Figure 2.1 shows the sky coverage of our multi-wavelength data and Figure 2.2 shows the  $2500 \text{ \AA}$  luminosity versus redshift distributions for each survey. Note that, in the so-called SDSS “Stripe 82” region (Annis et al., 2011) along the Northern Equatorial Stripe, the SDSS imaging data reaches roughly 2 mag deeper than the main survey as a result of co-adding many epochs of data.

### 2.1 Near-Infrared

Near-IR data in the  $JHK$  bandpasses are taken from the Two Micron All Sky Survey (2MASS; Skrutskie et al., 2006). These include values that were matched to the 2MASS All-Sky and “ $6\times$ ” point source catalogs using a matching radius of  $2''$  with the  $6\times$  deeper catalog taking priority. In addition to these data, we include  $2\sigma$  extractions (i.e., “forced photometry”) at the positions of known SDSS quasars. These objects have sufficiently accurate optical positions that it is possible to perform aperture photometry at their expected locations in the near-IR imaging, despite being non-detections in 2MASS. These  $2\sigma$  “detections” were cataloged by Schneider et al. (2010); we include those objects with a signal-to-noise ratio (S/N) greater than 2.

To supplement the 2MASS data, we have matched our catalog to the UKIRT (United Kingdom Infrared Telescope) Infrared Deep Sky Survey (UKIDSS; Lawrence et al., 2007). UKIDSS uses the  $YJHK$  filter system (Hewett et al., 2006); see also Peth et al. (2011). In order to generate our combined optical and near-IR data sets, we begin by source matching samples of SDSS data with the UKIDSS LAS catalog using the Cross-ID form located on the Web site of the WFCAM Science

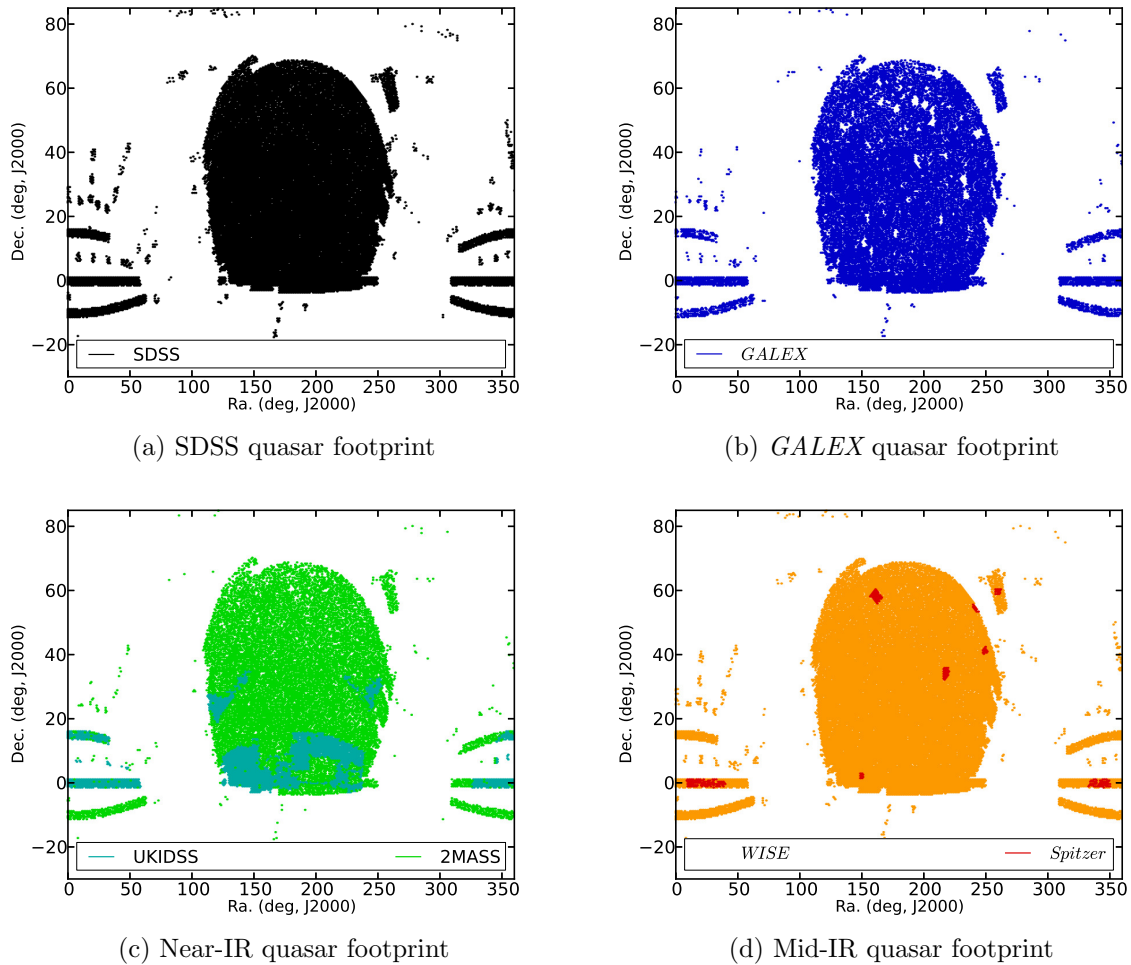


Figure 2.1 Footprints of the optically selected quasars in the matched surveys. Coverage of *GALEX* (blue), UKIDSS (teal), 2MASS (green), *WISE* (orange), and *Spitzer* (red) data are limited to the SDSS footprint (black) shown in the top-left panel.

Archive (WSA)<sup>1</sup>. In particular, we match against the UKIDSS DR5 LAS source table which contains the individual detections for a given object from each bandpass merged into a single entry. We use a matching radius of  $0.^{\circ}7$  and the nearest neighbor pairing option, accepting only the nearest object with a detection in at least one band as an acceptable match.

Since UKIDSS is deeper than 2MASS, when a quasar has data in both surveys, we only use the UKIDSS data. Between UKIDSS and 2MASS, 77,864 of our sample quasars have data in the near-IR: 35,749 from UKIDSS data and 41,434 from 2MASS, including both  $5\sigma$  detections and forced photometry. Figure 2.3 shows the difference between the UKIDSS and 2MASS magnitudes versus the UKIDSS magnitudes for the 12,130 quasars the two surveys have in common. We have split each figure into three distinct groups: quasars taken from the 2MASS  $5\sigma$  catalog, quasars with  $2\sigma$  2MASS extraction values in more than one filter, and quasars with  $2\sigma$  2MASS extractions in only

<sup>1</sup>[http://surveys.roe.ac.uk:8080/wsa/crossID\\_form.jsp](http://surveys.roe.ac.uk:8080/wsa/crossID_form.jsp)

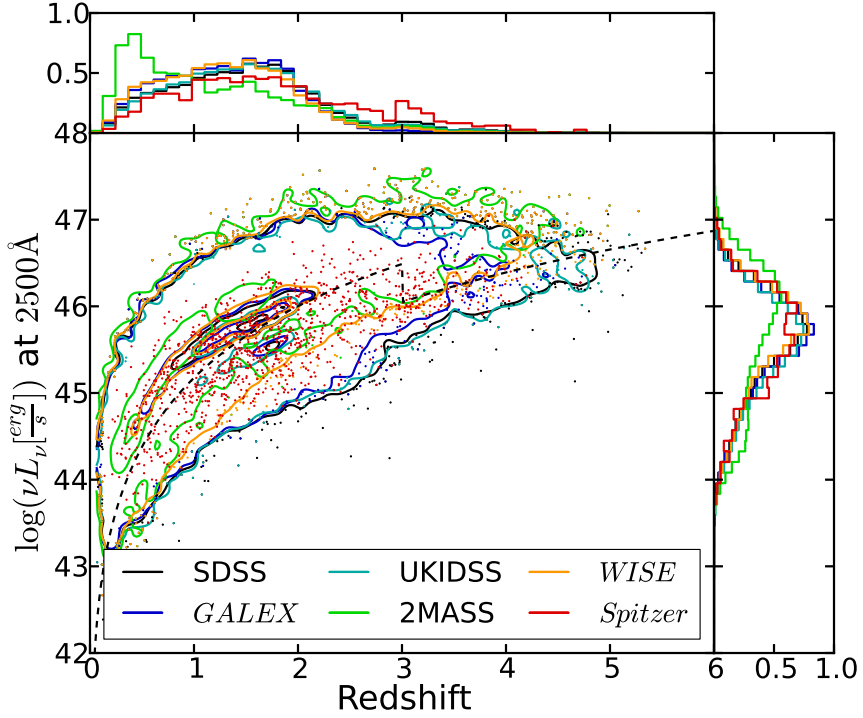


Figure 2.2 Contour-scatter plot showing the  $2500\text{ \AA}$  luminosity vs. redshift for each quasar color coded by survey. The contours indicate the linear density of scatter points on the plot with level drawn at 0.005, 0.5, and 0.95 of the normalized distributions. The histograms are normalized by the total number of quasars in each survey: 119,652 in SDSS, 42,043 in *GALEX*, 35,749 in UKIDSS, 23,088 in 2MASS, 85,358 in *WISE*, and 1196 in *Spitzer*. The black dashed line represents the flux limit of the main SDSS survey before extending the sample to lower luminosities.

one filter. As the quasars in the third group have much larger scatter (up to 2.5 mag) that can result in a misestimation of the quasar's luminosity by up to one order of magnitude, we have removed all quasars that fall into this group. This process leaves 23,088 objects in our 2MASS sample and brings our total number of QSOs with near-IR data to 58,837. In Table 2.1 all 2MASS and UKIDSS fluxes have been converted to the AB magnitudes using Hewett et al. (2006) conversions between AB and Vega magnitudes for the UKIDSS system.

## 2.2 Mid-Infrared

To extend our SEDs into the mid-IR, we included matches to the *WISE* final data release (Wright et al., 2010). The *WISE* bandpasses are generally referred to as  $W1$  through  $W4$  and have effective observed frame wavelengths of 3.36, 4.61, 11.82, and  $22.13\mu\text{m}$ , respectively, for a typical quasar SED. The matching was performed by taking all non-contaminated *WISE* point sources within  $2''$  of an SDSS quasar as a match. This matching radius maximizes the number of true objects matched while also minimizing the number of false matches. Figure 2.4 shows the number of *WISE* matches found as a function of separation distance from SDSS quasars. To ensure only the best matches

Table 2.1. Quasar Catalog Format

Column	Description
1	Previously published name
2	Right ascension in decimal degrees (J2000)
3	Declination in decimal degrees (J2000)
4	Redshift
5	BEST SDSS <i>u</i> band PSF magnitude
6	Error in <i>u</i> magnitude
7	BEST SDSS <i>g</i> band PSF magnitude
8	Error in <i>g</i> magnitude
9	BEST SDSS <i>r</i> band PSF magnitude
10	Error in <i>r</i> magnitude

Note. — This table is available in its entirety in a machine-readable form in the journal publication Krawczyk et al. (2013). A portion is shown here for guidance regarding its form and content.

were included, we also required that all matched quasars have  $S/N \geq 10$  in both *W1* and *W2*. In total, we have 85,358 matches to *WISE*; we estimate the false matching rate to be 1% based on the number of matches obtained after shifting all *WISE* data by 200'' in declination (red line in Figure 2.4). Since the *WISE* photometry was calibrated against blue stars it tends to overestimate the flux of red sources by about 10% in the *W4* band (Wright et al., 2010), this correction has been applied to all quasars in our sample.

When available, *Spitzer* IRAC data were also included. We specifically included data from the Extragalactic First Look Survey (XFLS; Lacy et al., 2005); Spitzer Deep-Wide Field Survey (SDWFS; Ashby et al., 2009); SWIRE DR2 (Lonsdale et al., 2003), including the ELAIS-N1, -N2, and Lockman Hole fields; S-COSMOS (Sanders et al., 2007), and our own extraction of high redshift QSOs in stripe 82 (S82HIZ, program number 60139). The fluxes for known SDSS quasars from the Stripe 82 program are reported here for the first time in Table 2.1 (*Spitzer* source labeled as S82HIZ). The IRAC bandpasses (ch1–ch4) have effective wavelengths of 3.52, 4.46, 5.67, and 7.7  $\mu\text{m}$  for a typical quasar SED. There are a total of 1196 matches to *Spitzer*. For a small number of quasars ( $\sim 200$ ) both *Spitzer* and *WISE* data are available; in these cases, we use both data sets. In Table 2.1 all *Spitzer* and *WISE* fluxes are reported in AB magnitudes.

### 2.3 Ultraviolet

To extend the SEDs into the UV, we use *Galaxy Evolution Explorer* (*GALEX*; Martin et al., 2005) data when available. The effective wavelengths for the near-UV (NUV) and the FUV bandpasses are 2267Å and 1516Å, respectively. Most of our matches are taken from Budavári et al. (2009) who matched *GALEX*-GR6 to SDSS-DR7. For this study, we have taken only the most secure matches; that is, only one SDSS quasar matched to only one *GALEX* point source. This algorithm gives 14,302 matches and leaves out 53,782 quasars that have multiple SDSS sources matching to the same *GALEX* source. In addition to these data, we include forced point-spread function (PSF) photometry (Bovy et al., 2011, 2012) on the *GALEX* images in the positions of the SDSS point

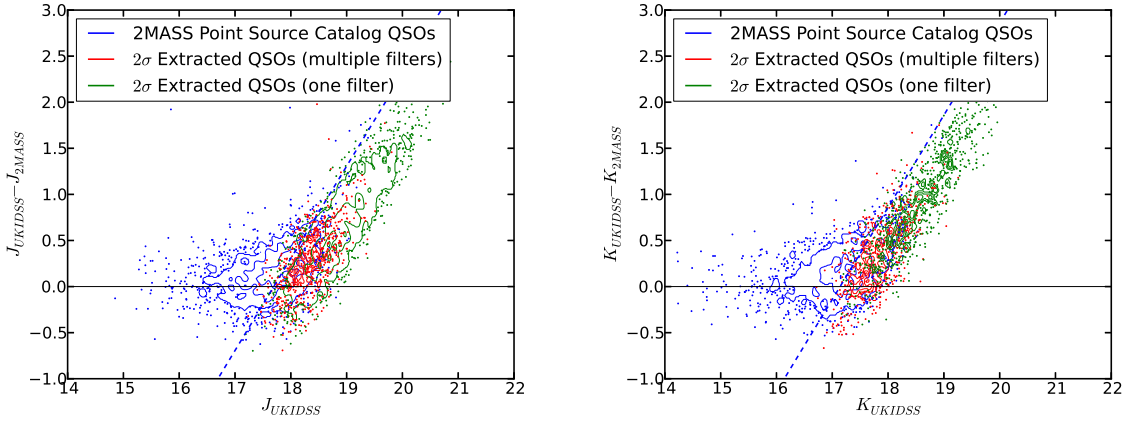


Figure 2.3 Contour-scatter plot showing the difference between the 2MASS and UKIDSS magnitudes vs. the UKIDSS magnitudes for the  $J$  and  $K$  filters. The blue contours/dots show the catalog 2MASS values, green shows the 2MASS  $2\sigma$  extraction values with a detection in only one band, and red shows the rest of the extracted values. The blue dashed line shows the 2MASS point source catalog's limiting magnitude. The two surveys contain 12,130 quasars in common. Green points were excluded as the errors are quite large (see text). Similar results were found for the  $H$  filter.

sources, which adds 61,490 detections. As with 2MASS, we only kept the extracted data with  $S/N \geq 2$ , and as with the Budavári et al. (2009) matches, we limit the sample to those with no source confusion; this reduces the number of extracted quasars to 27,744. Combining both sets, the total number of matches is 42,046. All *GALEX* photometry has been corrected for Galactic extinction, assuming  $A_{\text{NUV}} = 8.741 \times E(B-V)$  and  $A_{\text{FUV}} = 8.24 \times E(B-V) - 0.67 \times E(B-V)^2$  (Wyder et al., 2007). The  $E(B-V)$  values are taken from the Schneider et al. (2010) catalog. All the matched data are given in Table 2.1.

## 2.4 X-Ray

To construct full SEDs, we must extend our data into the X-ray regime. Due to comparatively limited sky coverage of sensitive X-ray observations, the number of our quasars with X-ray data is quite small compared to the size of the samples in the optical and IR. For example, there are only 277 matches in the ChaMP data set (Green et al., 2009). So instead we take advantage of the careful work on mean X-ray properties as a function of UV luminosity as compiled by Steffen et al. (2006). Specifically, we determine the X-ray flux of each quasar using the  $L_{\text{UV}}-L_{\text{X}}$  relation that parameterizes the correlation between the 2500Å and 2keV luminosity of quasars. We find the 2500Å luminosity by extrapolation from the closest filter using an  $\alpha_{\text{opt}} = -0.44$  (Vanden Berk et al., 2001). The 2 keV luminosity is estimated using Equation 1.13 and our 2500Å luminosities. An X-ray energy spectral index  $\alpha_x = -1$  (photon index  $\Gamma = -2$ ) was assumed between 0.2 keV and 10 keV (e.g. George et al., 2000). In this way, we can estimate the X-ray part of the SED for all of our sources rather than using just the small fraction of objects with robust X-ray detections. This process ignores the correlations between  $\alpha_{\text{ox}}$  (and  $\alpha_{\text{uv}}$ ) and  $\alpha_x$  as discussed in Kruczek et al. (2011); however, these trends are small as compared to the overall trend with luminosity.

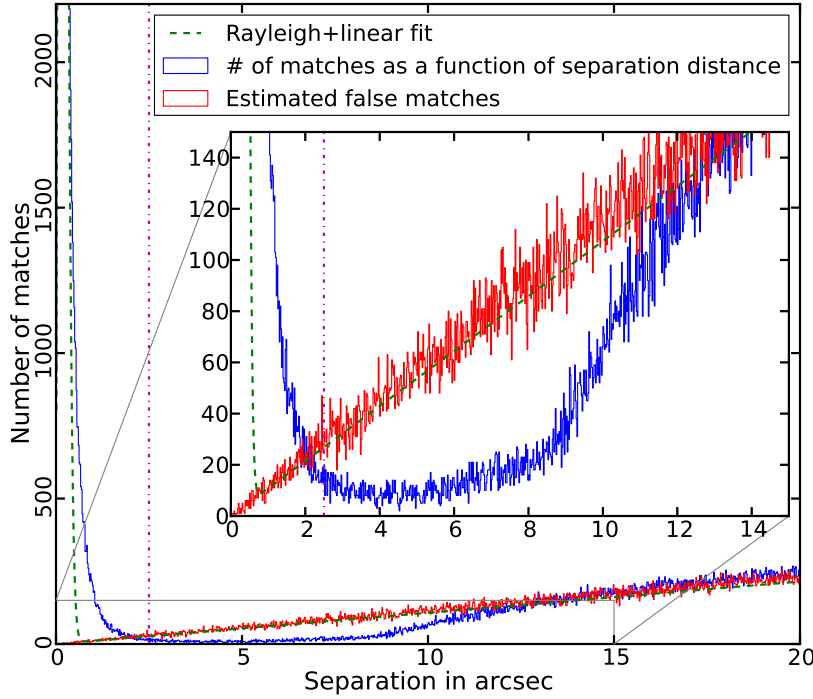


Figure 2.4 Angular separation between known quasars and nearby *WISE* sources (blue) and the known quasars with declinations shifted by  $200''$  (red). The green curve shows the best fit expected distribution (Rayleigh distribution for small separations and linear growth for larger separations). The vertical magenta dot-dash line indicates the matching radius used. As seen in the inset, the blue histogram does not follow the expected distribution; this is due, in part, to the large beam size of *WISE* ( $\text{FWHM}=6''$ ).

As a check we have compared our X-ray extrapolations to ChaMP data from Green et al. (2009, see Section 3.2). In all cases we found the X-ray data to fall within the  $1.5\sigma$  limits of the  $\alpha_{\text{ox}}$  extrapolation.

## 2.5 The Dust Reddening Sample

For the analysis in Chapters 4 and 5 we limit our sample to the uniformly selected point source quasars (Richards et al., 2006b), leaving an initial sample of 55,772 quasars. This cut mitigates against any biases due to selection effects.

In order to better understand the dust present at a quasar's redshift, we further desire to minimize the effects of reddening caused by intervening galaxies. We achieve this by removing 16,450 quasars that show signs of strong absorption line systems along the line of sight. The presence of strong absorption lines in the spectrum of a quasar generally indicates that the light is passing through an intervening galaxy. As dust in those galaxies can redden the quasar spectrum (York et al., 2006; Ménard et al., 2008; Khare et al., 2012), it is important to remove such quasars from our sample. We specifically removed all quasars with at least two identified absorption lines (grade C or higher in

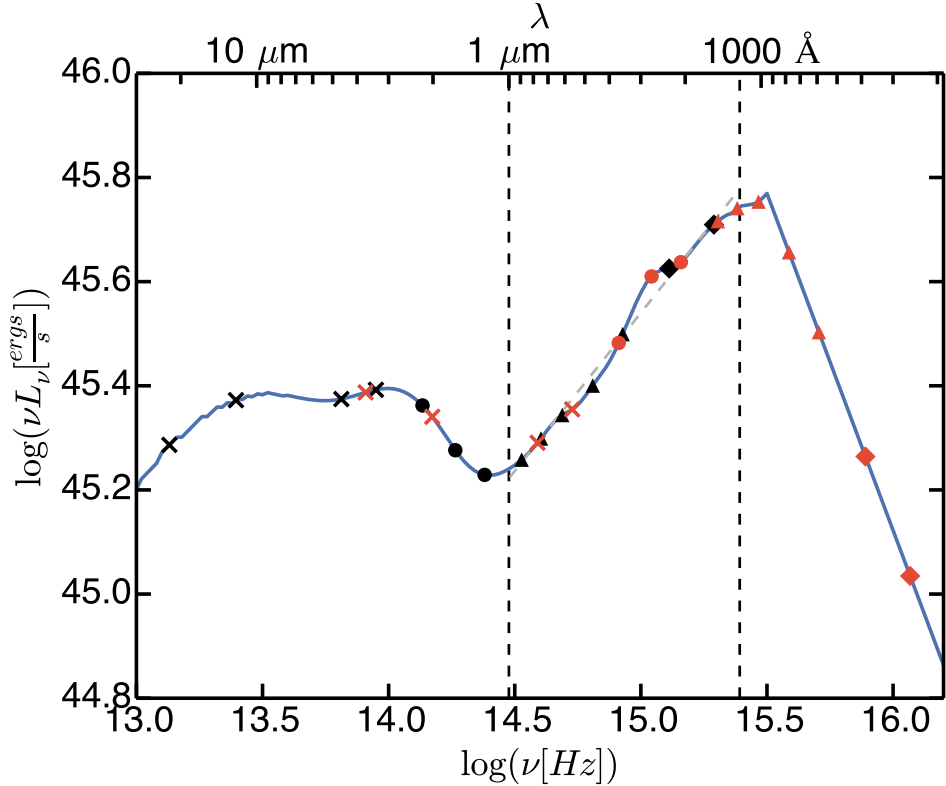


Figure 2.5 Position of various filters on the mean quasar SED (with the major spectral lines removed) for  $z = 0$  (black) and  $z = 5$  (orange). The filters are from *WISE* (x's), 2MASS/UKIDSS (circles), SDSS (triangles), and *GALEX* (diamonds). The vertical dashed lines show the range where the SED is well approximated as a powerlaw (dashed grey line  $\alpha_\nu = -0.39$ ); all but the two reddest filters pass through this range for the redshift distribution of our sample.

the parlance of York et al. (2005)) with a Mg II line having an equivalent width (EW)  $\geq 0.3 \text{ \AA}$  (York et al. 2014, in preparation). These systems are thought to be associated with absorbing columns of  $N_{\text{HI}} \sim 10^{18-20} \text{ cm}^{-2}$  (Churchill et al., 2005; Prochaska et al., 2010).

This process yields a sample of quasars that is not selected preferentially because of radio properties and whose observed SED should be dominated by the physics of the accretion disk and dust reddening/extinction that is local to the quasar and/or the host galaxy. As broad absorption line (BAL) quasars are seen to have different reddening properties (Sprayberry & Foltz, 1992) and perhaps intrinsically different SEDs (Weymann et al., 1991; Reichard et al., 2003b), we split the sample into two groups: broad absorption line (BAL) quasars, as identified by Shen et al. (2011) and York et al. (2014, in preparation), and non-BAL quasars, containing 1,744 and 34,233 quasars respectively.

For our dust analysis we only use the filters that fall between  $1 \mu\text{m}$  and  $1216 \text{ \AA}$  in a quasar's rest frame (the portion consistent with a powerlaw). Because of these limits, only the following filters are used: *NUV* and *FUV* from *GALEX*, *ugriz* form SDSS, *JHK* from either 2MASS or UKIDSS, and *W1-2* from *WISE*. Figure 2.5 shows the positions of these filters on the mean quasars SED (see Chapter 3) for  $z = 0$  (black) and  $z = 5$  (orange). This mean SED has a powerlaw index of

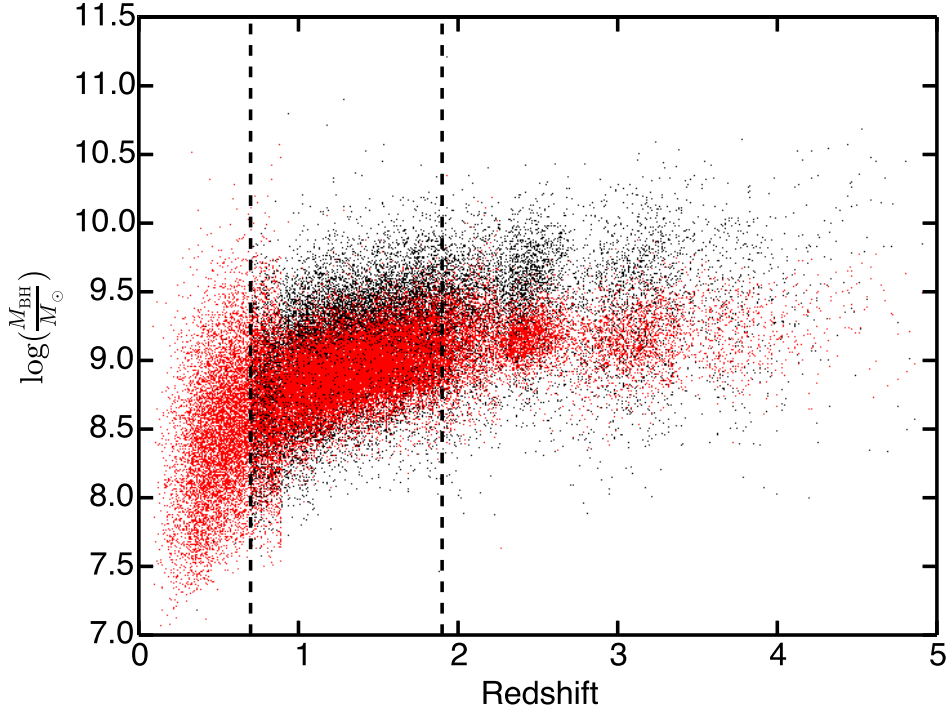


Figure 2.6  $M_{\text{BH}}$  vs. redshift for the Shen et al. (2011) masses (black) and the re-calibrated masses used in this work (red). The vertical dashed lines indicate the redshift for transitioning between the different spectral line relations (H $\beta$ , Mg II, and C IV from left to right).

$\alpha_{\nu} = -1.39$  (grey dashed line) and the small blue bump is visible at  $\sim 3500 \text{ \AA}$ .

## 2.6 Black Hole Masses

To build a catalog of  $M_{\text{BH}}$  for our sample we began with the masses presented in Shen et al. (2011) and matched them to the non-BAL quasar sample from §2.5. These masses are estimated using the width of H $\beta$  ( $z < 0.7$ ), Mg II ( $0.7 \leq z < 1.9$ ), or C IV ( $z \geq 1.9$ ) using the  $R_{\text{BLR}}$ -luminosity relations from McLure & Dunlop (2004, H $\beta$  and Mg II<sup>2</sup>), Vestergaard & Peterson (2006, H $\beta$  and C IV), and Vestergaard & Osmer (2009, Mg II). In the language of Equation 1.20 these relations are:

$$\begin{aligned}(a, b) &= (0.910, 0.50), \quad \text{VP06; H}\beta \\(a, b) &= (0.740, 0.62), \quad \text{S11; Mg II} \\(a, b) &= (0.660, 0.53), \quad \text{VP06; C IV}\end{aligned}$$

All of the masses in the Shen et al. (2011) catalog assume  $\Delta V^2 \propto \text{FWHM}^2$ , an assumption that has been shown to introduce significant scatter when compared to RM masses (Wang et al., 2009; Rafiee & Hall, 2011; Peterson, 2011; Denney, 2012; Denney et al., 2013; Park et al., 2013). As a result, we use the updated scaling relations (using Equation 1.21) for Mg II and C IV as presented in Rafiee & Hall (2011) and Park et al. (2013):

<sup>2</sup>The Mg II relation was updated in Shen et al. (2011)

$$(a, b, \gamma) = (7.25, 0.51, 1.27), \text{ RH11; Mg II}$$

$$(a, b, \gamma) = (7.48, 0.52, 0.56), \text{ P13; C IV}$$

Additionally, we included the intrinsic scatter for each of these relations into the uncertainty estimates for each mass. Figure 2.6 shows  $M_{\text{BH}}$  as a function of redshift for the Shen et al. (2011) masses (black) and the re-calibrated masses used in this work (red). The re-calibrated masses are systematically smaller than the original catalog masses.

For these updated black hole masses we have not taken into account the effects of extinction within the quasar itself (see Chapter 4 for more details). This correction turns out to be small and on average increases  $M_{\text{BH}}$  by 0.02 dex, and in most cases (99% of the sample) the “de-reddened” masses are within  $1\sigma$  of the “reddened” masses. Given how small this correction is we do not apply it to our sample.

Recent work (Denney, 2012; Denney et al., 2013; Kratzer & Richards, 2014) has cast doubt over estimating  $M_{\text{BH}}$  based on the C IV line using the survey quality spectra from SDSS. In particular Denney et al. (2013) argue that the low  $S/N$  of the SDSS spectra do not allow for the proper characterization of the C IV line (e.g. line dispersion) leading to higher scatter (and higher uncertainties) when compared to the more reliable H $\beta$  masses. Although these issues are present within our data, we still include the C IV masses in the data analysis of Chapter 5. However, our analysis weights each mass by its uncertainty, so even when we removed the C IV masses from our sample the results of our analysis do not change.

## Chapter 3: Multi-wavelength SEDs

To improve our understanding of the mean SED (and its range), we have constructed quasar SEDs, spanning from the mid-IR ( $\sim 30\mu\text{m}$  in the rest frame) to the FUV ( $\sim 300\text{\AA}$  in the rest frame), for quasars cataloged by the SDSS (York et al., 2000). The data used for this analysis are presented in Chapter 2. §3.1 describes all the corrections applied to the data. §3.2 gives an overview of our data analysis and construction of mean SEDs. §3.3 presents our findings for individual and mean bolometric corrections, and our discussion and conclusions are presented in §3.4 and §6 respectively.

### 3.1 Corrections

When studying quasar SEDs, we are interested in the *true* continuum level of the radiated light. The continuum may be contaminated by, for example, spectral emission lines, absorption by intergalactic hydrogen clouds, host galaxy contamination, and beaming effects. Here we address each of these features. For the hydrogen absorption and broad emission lines, we determine a magnitude correction by folding a model through the filter curves as discussed below. For the host galaxy correction, we subtract a model template. We do not consider beaming specifically, but refer the reader to Runnoe et al. (2012) for a discussion of how our results would change under the assumption of non-isotropic emission; see also Nemmen & Brotherton (2010).

#### 3.1.1 Lyman Forest and Limit

A particular challenge is to determine the SED in the extreme-UV (EUV) ( $\lambda_{\text{rest}} < 1216\text{\AA}$ ) part of the spectrum where intergalactic hydrogen causes significant attenuation of the quasar signal (Ly $\alpha$  forest; Lynds, 1971). To account for this attenuation, the redshift-dependent effective optical depth,  $\tau_{\text{eff}}(z, \lambda)$ , of Meiksin (2006) was used. This optical depth models the average attenuation of a source assuming Poisson-distributed intergalactic hydrogen along the line of sight, out to a given redshift. This optical depth is split into three parts: the contribution due to resonant scattering by Lyman transitions, systems with optically thin Lyman edges, and Lyman Limit Systems (LLS). Figure 3.1 shows this model for redshifts of 1, 2, and 3 for both LLS and non-LLS.

Because our investigation uses photometry and not spectra, we do not know whether a LLS is present. Furthermore, we only have spectral coverage of the LLS region for a fraction of our sources. Thus, to be as conservative as possible, we assume that there is *no* LLS present; that way we only make the *minimum* correction needed for each SED. However, it is important to note that the SDSS quasar selection algorithm has been shown to preferentially select quasars possessing a LLS in the range  $3 \lesssim z \lesssim 3.5$  (Worseck & Prochaska, 2011).

For the continuum ( $F_\nu$ ) we have assumed a powerlaw of the form  $\nu^{-0.44}$  (Vanden Berk et al., 2001), consistent with the results of Scott et al. (2004). Continuum weighting is necessary since we are dealing with broadband photometry and not spectroscopy. With high resolution spectroscopic data the correction is exact as the Meiksin (2006) corrections themselves are independent of the SED.

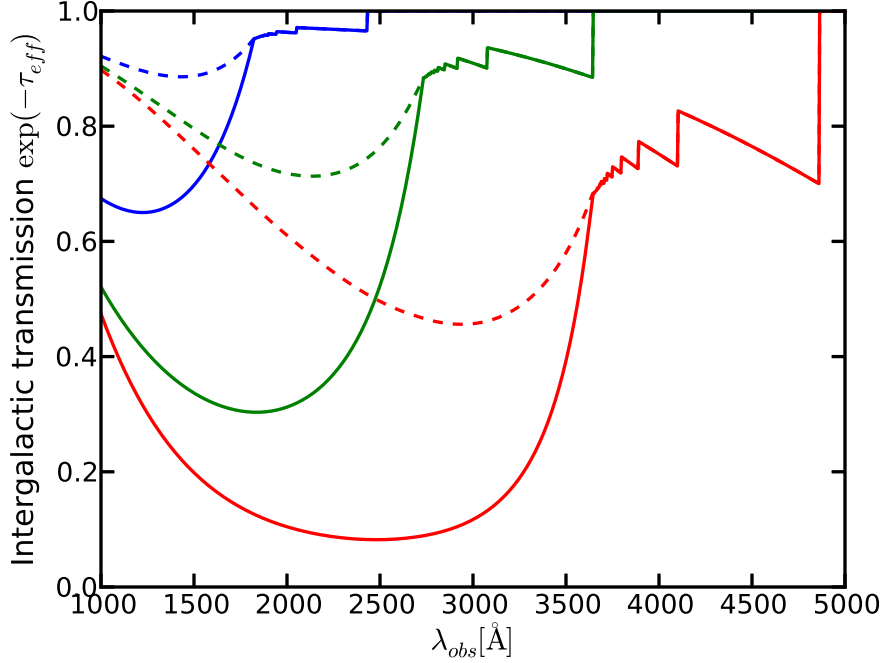


Figure 3.1 Meiksin (2006) model for Lyman series extinction as a function of observed wavelength for  $z = 1$  (blue),  $z = 2$  (green), and  $z = 3$  (red). The solid lines show the extinction assuming a LLS (at the corresponding redshifts) along the line of sight, and the dashed lines show the extinction without a LLS. The jagged edges are a result of absorption from the Lyman series and the drop-off is due to absorption from the IGM and any hydrogen clouds along the line of sight. The transmission rises with decreasing wavelength for each feature because the shorter wavelengths sample lower redshifts and the universe is more ionized at lower redshifts.

However, for broadband photometry, where the bandpass can overlap features in the  $\tau$  distribution, the convolution of the SED with the filter response changes the effective wavelength of the bandpass.

To apply the Lyman forest correction, we convolve a continuum with the Meiksin (2006) optical depth and each filter over  $0 < z < 6$  in  $\Delta z$  steps of 0.01 and use linear interpolation to precisely match redshifts. Following Meiksin (2006), the correction is given in magnitudes as a transmission weighted average of  $\tau$ :

$$K_{\text{IGM}} = -2.5 \times \log \left( \frac{\int \lambda S_\lambda F_\lambda e^{-\tau_{\text{eff}}} d\lambda}{\int \lambda S_\lambda F_\lambda d\lambda} \right), \quad (3.1)$$

where  $S_\lambda$  is a transmission filter curve,  $F_\lambda$  is the continuum, and  $\tau_{\text{eff}}$  is the redshift-dependent effective optical depth. This value is calculated independently for each filter and makes  $m(\tau = 0) = m(\tau) - K_{\text{IGM}}$  such that all quasars are made brighter in the Lyman absorption regions as a result of the correction.

### 3.1.2 Emission Lines

The presence of emission lines in a photometric bandpass affects quasar magnitudes as illustrated by Richards et al. (2006b, e.g., see their Figures 8 and 17). Thus, to make a fair comparison between

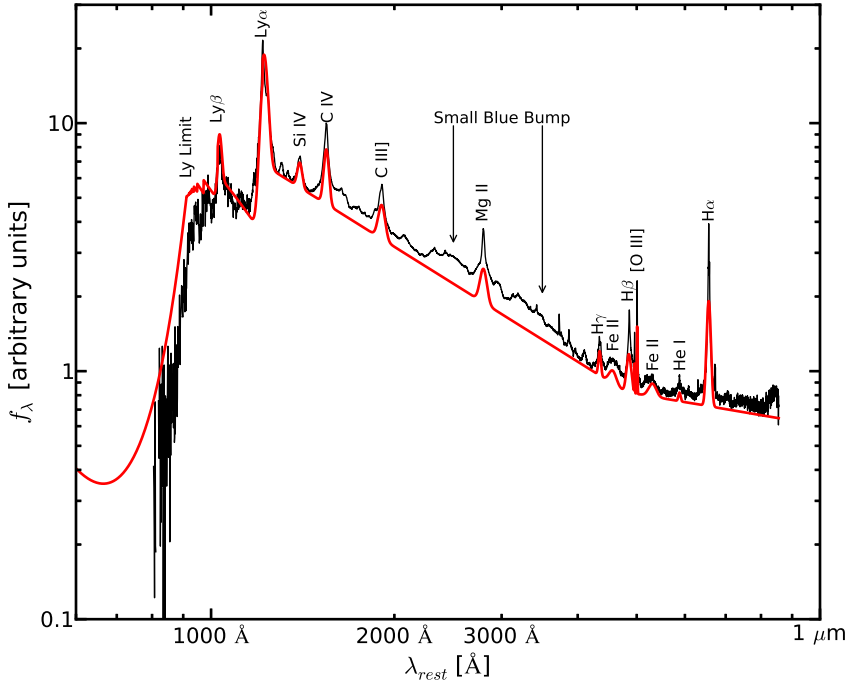


Figure 3.2 Vanden Berk et al. (2001) composite spectra (black) with our model spectrum with a LLS (red) at a redshift of 3.75. Since the SDSS spectra cover 3800–9200 Å, the contributors to the points at  $\lambda_{\text{rest}} < 1216$  Å are high- $z$  quasars and are consistent with the model used. Since we model the main emission line features, on average, they should not appear in the SEDs. However, unmodeled residuals in Fe II and the Balmer continuum (small blue bump) can clearly be seen in the SEDs on either side of the Mg II emission line at 2800 Å. We use a double powerlaw continuum in this figure since the composite spectra do not correct for host galaxy contributions on the red end. Model spectra used to correct our SEDs are placed on a single powerlaw as shown in Figure 3.3.

sources at all redshifts, we endeavor to remove first-order effects of the emission line contributions to the measured magnitudes. Our emission-line template takes the position, width, and equivalent width (EW) of the 13 strongest spectral lines (as labeled in Figure 3.2) from Vanden Berk et al. (2001). We make no attempt to correct for the small blue bump (i.e. Balmer continuum or Fe II emission), but recognize that those features can have a significant impact; indeed, their residuals can be seen in our mean SEDs. Figure 3.2 shows the mock spectrum used in our emission-line corrections; it includes a double powerlaw continuum ( $\alpha_\nu = -0.46$  for  $\lambda_{\text{rest}} \leq 4600$  Å and  $\alpha_\nu = -1.58$  for  $\lambda_{\text{rest}} > 4600$  Å) and 13 emission lines.

The correction is computed as

$$K_{\text{em}} = -2.5 \times \log \left( \frac{\int \lambda S_\lambda F_\lambda(c\&l) d\lambda}{\int \lambda S_\lambda F_\lambda(c) d\lambda} \right), \quad (3.2)$$

where  $S_\lambda$  is a transmission filter curve,  $F_\lambda(c)$  is the continuum, and  $F_\lambda(c\&l)$  is the continuum with spectral lines. This value is calculated independently for each filter and makes  $m(c) = m(c\&l) - K_{\text{em}}$ ,

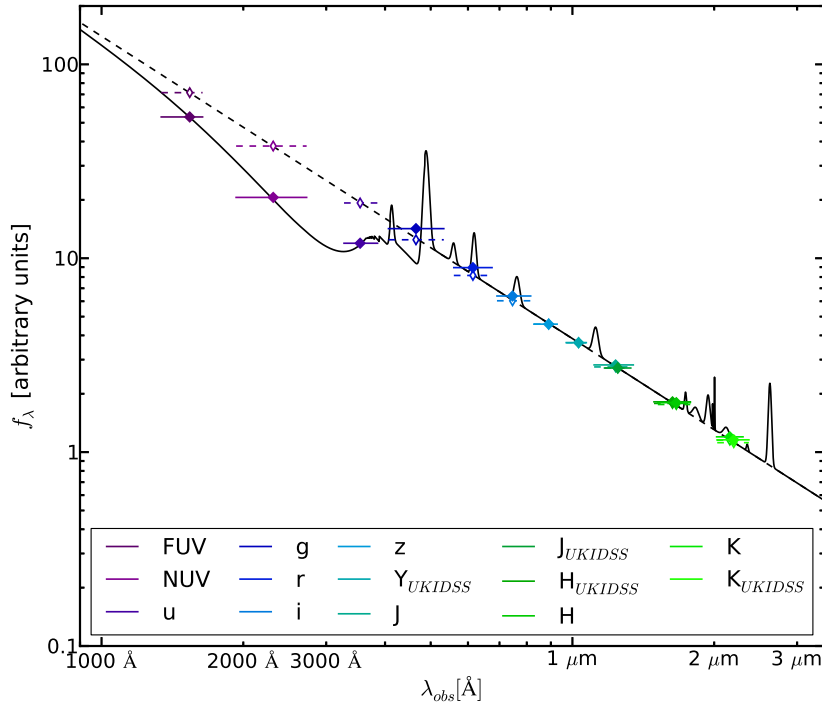


Figure 3.3 Observed frame mock spectrum (solid line) and  $\alpha_\nu = -0.44$  continuum (dotted line) for a  $z = 3$  quasar. The closed diamonds bifurcated by solid lines indicate the “measured” instrumental magnitudes, while open diamonds bifurcated by dashed lines indicated the corrected values (assuming an underlying powerlaw SED). The width of the lines indicate the width of the bandpasses. Here we have corrected for IGM attenuation (Section 3.1.1) and emission line flux (Section 3.1.2).

such that all quasars are made fainter by the removal of the emission line contribution.

We further use this template to illustrate the correction for hydrogen absorption (assuming the quasar is at  $z = 3.75$  and there is a LLS). Overall, we find reasonable agreement (by eye) with the mean composite spectrum from Vanden Berk et al. (2001) in terms of the continuum, broad emission lines, and intergalactic medium (IGM) attenuation.

In Figure 3.3, we illustrate the effect of these emission-line and IGM corrections using a mock spectrum of a  $z = 3$  quasar (without a LLS). Colored points indicate the observed instrumental magnitudes and the intrinsic continuum magnitudes after applying the emission line and IGM  $K$ -corrections.

### 3.1.3 Host Galaxy

It is also necessary to correct the data for host galaxy contamination. Since we lack the data to measure this directly, we must estimate the host galaxy contribution. To do this, we combine two different models: the relation outlined in Shen et al. (2011) for the higher luminosity quasars, and the relationship from Richards et al. (2006a) for the lower luminosity quasars. The Shen et al. (2011)

relationship is

$$\frac{L_{\text{5100}\text{\AA},\text{host}}}{L_{\text{5100}\text{\AA},\text{QSO}}} = 0.8052 - 1.5502x + 0.9121x^2 - 0.1577x^3 \quad (3.3)$$

where

$$x \equiv \log \left( \frac{\lambda_{\text{5100}\text{\AA}} L_{\text{5100}\text{\AA},\text{total}}}{\text{erg s}^{-1}} \right) - 44$$

and

$$0 \leq x < 1.053,$$

which sets the relative scaling at 5100Å. To extend this expression to all wavelengths, we use the elliptical galaxy template of Fioc & Rocca-Volmerange (1997) scaled to 5100Å. When  $x \geq 1.053$ , the quasar completely outshines the host galaxy and no correction needs to be applied. We note that this relationship was found using quasars that have  $\log(\lambda_{\text{5100}\text{\AA}} L_{\text{5100}\text{\AA},\text{total}}) \geq 44$ , and cannot, in general, be extrapolated to lower luminosities.

We found that, for lower luminosity quasars, the Shen et al. (2011) equation overestimates the host galaxy; we instead use the relationship from Richards et al. (2006a) which, was adapted from the relationship used by Vanden Berk et al. (2006):

$$\begin{aligned} \log(L_{\text{6156}\text{\AA},\text{host}}) &= 0.87 \log(L_{\text{6156}\text{\AA},\text{AGN}}) \\ &\quad + 2.887 - \log(L_{\text{Bol}}/L_{\text{Edd}}) \quad (3.4) \\ \text{where } \log(L_{\text{6156}\text{\AA},\text{AGN}}) &= \log \left( \frac{L_{\text{6156}\text{\AA},\text{total}}}{\text{erg s}^{-1}\text{Hz}^{-1}} - \frac{L_{\text{6156}\text{\AA},\text{host}}}{\text{erg s}^{-1}\text{Hz}^{-1}} \right). \end{aligned}$$

This system of equations is then solved numerically for the host galaxy luminosity. As in Richards et al. (2006a) we take  $L_{\text{Bol}}/L_{\text{Edd}}$  to be unity, since this provides the minimum correction needed. This sets the relative scaling at 6156Å and, as before, we use the elliptical galaxy template of Fioc & Rocca-Volmerange (1997) to extend this to all wavelengths. To ensure a smooth transition between these two methods, we have chosen the crossover luminosity to be the point at which both methods agree,  $\log(\lambda_{\text{5100}\text{\AA}} L_{\text{5100}\text{\AA},\text{total}}) = 44.75$ . As host galaxy subtraction can have a large impact on the SED near 1 μm and it is not a well-established procedure, we note that other methods include Croom et al. (2002), and Maddox & Hewett (2006).

It was brought to our attention that the host galaxy model used in Richards et al. (2006a) was incorrect (K. Leighly, private communication 2012). The model was converted from  $F_\lambda$  to  $F_\nu$ , but was not converted to  $\nu F_\nu$  before subtracting it from the SEDs. This does not effect the SED at 5100Å, where the SEDs are normalized, but it is systematically wrong on either side of this wavelength. Herein we correct that error.

### 3.1.4 Gap Repair

Since all the quasars in our sample have been selected from SDSS photometric data, they all have *ugriz* measurements, but are not guaranteed to have measurements in the other bandpasses that we utilize. To address this issue we will “gap repair” all missing data in a way similar to Richards et al. (2006a). Specifically, we replace missing values with those determined by normalizing an interpolation/extrapolation of the continuum in the next nearest bandpass for which we have data. Sometimes this will be a previously constructed mean SED; other times it will be a functional form. To estimate errors for the gap filled points, we have fit up to third-order polynomials to plots of the

magnitude errors,  $\log(\sigma_m)$ , versus magnitudes,  $m$ , for each of the filters. These functions were then used to estimate  $\sigma_m$  for the gap filled value for  $m$ .

This procedure works well where we can interpolate between filters (e.g., at wavelengths longward of the Lyman limit). Beyond the Lyman limit, we are no longer interpolating, but extrapolating, which is a trickier process. Using limiting magnitudes does not solve the problem as redshift effects mean that even if all quasars had coverage from all of the filters, the same rest-frame wavelengths are not observed for both high- and low-redshift quasars.

On the long wavelength end, we always extrapolate to longer wavelengths using the mean SED from Richards et al. (2006a), normalized to the nearest measured bandpass. On the short wavelength end, the gap repair process depends on whether we are making a mean SED or attempting to reconstruct the SED for an individual quasar (e.g., to determine its bolometric luminosity). See below for details for specific cases.

Unless otherwise stated, the X-ray part of the SED is determined using Equation 1.13, the  $L_{\text{uv}} - \alpha_{\text{ox}}$  relation from Steffen et al. (2006), and linearly interpolating between the X-ray and the bluest data point after gap repair. The errors in this region are determined from the uncertainties of the Steffen et al. (2006) relation.

## 3.2 Mean SEDs

### 3.2.1 Overall Mean SED

To determine the mean quasar SED, we converted all the flux densities for each quasar to luminosity densities and shifted each broadband observation to the rest frame. The data were then placed onto a grid with points separated by 0.02 in  $\log(\nu)$ ; kriging was then used to align the broadband luminosities to our grid points. Kriging is a nonparametric interpolation method that predicts values and errors for regions between observed data points. Rybicki & Press (1992) were among the first to present this technique in the astronomical literature (under the name Wiener filtering). Since then it has been mainly used to estimate light curves (e.g., Kozłowski et al., 2010).

Kriging estimates the correlation between data points as a function of separation, then uses this correlation to interpolate between the data points. We used the R package `gstat` to perform variance-weighted kriging using an exponential variogram model. Once the data are rebinned in the rest-frame, the arithmetic mean and standard deviation are taken at each grid point. Because kriging estimates variance values at each of the new grid points, we are able to estimate errors on our bolometric luminosities and the derived bolometric corrections.

Figure 3.4 shows the “raw” data points (without the corrections described in Section 3.1) and mean for all the quasars in our sample. On the red end, the SED drops due to a lack of data and on the blue end, shortward of the  $\text{Ly}\alpha$  line, there is a clear drop due to intergalactic extinction. The flattening in the mean shortward of the Lyman limit is due to redshift effects; low-redshift sources have no rest-frame measurements at this frequency, biasing the data toward higher luminosity.

To find the corrected mean SED, we first construct a “gap filling” SED by looking at the mean SED of  $\sim 2100$  quasars with full wavelength coverage; i.e., they have at least four data points in mid-IR, at least three data points in the near-IR, and full coverage with *GALEX* in the UV. Redshift effects cause the SED coverage in the rest frame to drop off sharply around the Lyman series. To

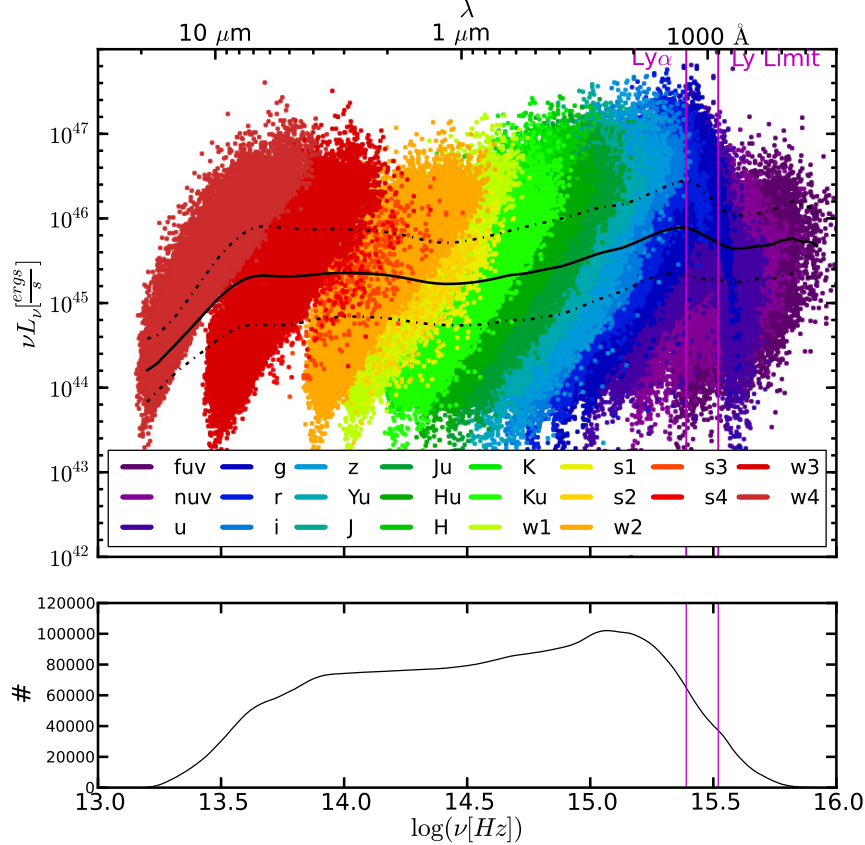


Figure 3.4 Top: mean uncorrected SED (solid line), data points for all quasars, and  $1\sigma$  level (dash-dotted line) for the raw sample (no corrections applied, see Section 3.1). The steep drop-off on the red end is caused by the lack of high luminosity, low redshift quasars in our sample; this is caused by both quasar evolution and the fact that at lower redshifts we sample a smaller volume of the universe. The white wedges between the filters are caused by the limiting magnitudes for each filter. The drop-off just shortward the Ly $\alpha$  line is due to IGM attenuation, but the flattening shortward of the Lyman limit is due to the lack of low-luminosity, high-redshift quasars, caused by the detection limits of the surveys. Bottom: the number of SEDs averaged at each frequency. The two vertical magenta lines show the positions of the Ly $\alpha$  line at  $1216\ \text{\AA}$  and the Lyman limit at  $912\ \text{\AA}$ .

avoid the mean being biased towards the higher luminosity SEDs in this region we have truncated this gap filling mean SED where the total number of quasars drops (around  $1216\ \text{\AA}$ ) and use the mean UV luminosity,  $\langle L_{2500\text{\AA}} \rangle$ , to find the X-ray luminosity using Equation 1.13. Figure 3.5 shows the resulting mean SED that we will use for gap filling individual quasar SEDs that lack full coverage in all of the bandpasses considered herein.

To find the mean SED for the *entire* sample, we apply the corrections described in Section 3.1, but only gap repairing filters with wavelengths  $\lambda > 912\text{\AA}$ , so that way we avoid gap filling in a region that is not well sampled with our gap-filling SED. We then truncate the mean at  $912\ \text{\AA}$  and use the mean UV luminosity,  $\langle L_{2500\text{\AA}} \rangle$ , to find the X-ray luminosity using Equation 1.13. We do this instead of using actual X-ray data since there are too few X-ray detections and Steffen et al. (2006) have already done the careful work of extracting the relationship between the UV and the X-ray parts of

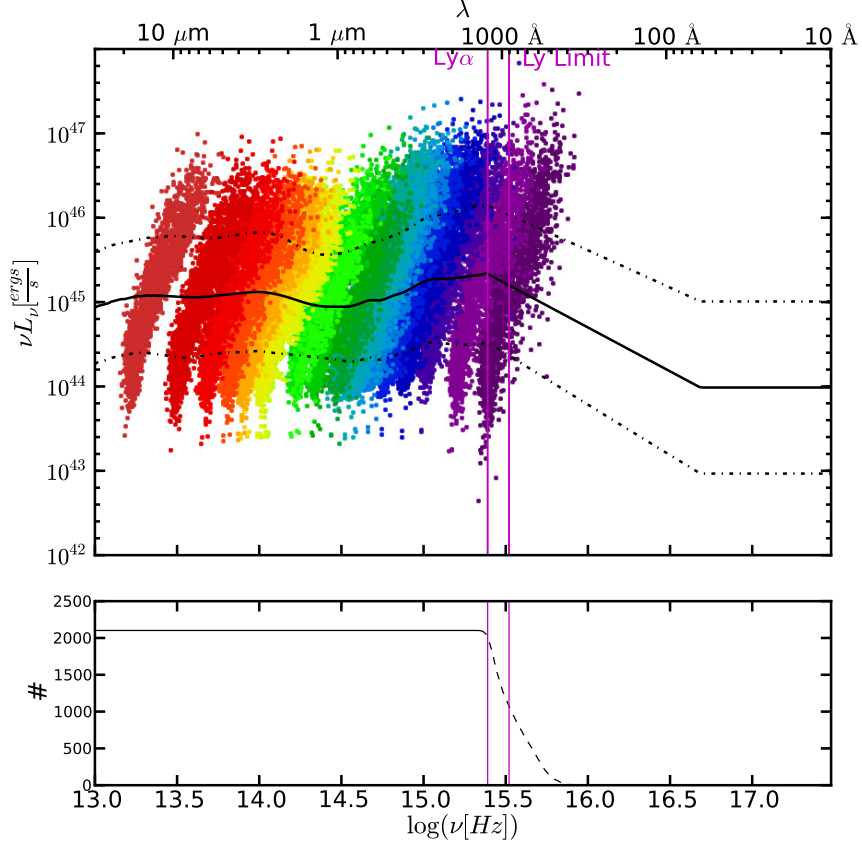


Figure 3.5 Top: mean “gap filling” SED (solid line), based on  $\sim 2100$  quasars with full broadband wavelength coverage. To avoid a bias towards high luminosity at the blue end where the number of quasars drops off, the mean is truncated at  $1216\text{ \AA}$ , and connected with the X-ray (see text). Bottom: the number of SEDs averaged at each frequency. The dotted line indicates the data that is not used due to truncation (see text). The two vertical magenta lines show the positions of the Ly $\alpha$  line at  $1216\text{ \AA}$  and the Lyman limit at  $912\text{ \AA}$ .

the SED.

Both radio-loud and radio-quiet quasars are included. The mean SED of 108,184 quasars is given in tabular form in Table 3.1. Figure 3.6 shows the resulting mean with the Richards et al. (2006a) mean, the Vanden Berk et al. (2001) powerlaw, a typical host galaxy, and the ChAMP X-ray data included for comparison. The difference between our mean SED and that of Richards et al. (2006a) in the  $912\text{--}1216\text{\AA}$  region is due to our more careful corrections of systematic effects in this region as described in Section 3.1. The abrupt change in the slope of the SED at  $\sim 1100\text{ \AA}$  is not expected to be real, but rather represents our lack of knowledge of this region of the SED. We are largely limited to simply connecting the two better known regions of the NUV and soft X-ray with a powerlaw. We will further discuss the range of possible FUV continua in Section 3.4.

Table 3.1. Mean Quasar SEDs

$\log(\nu)$	All	$\sigma_{\text{All}}$	Low Lum.			Mid Lum.			High Lum.			C IV Line Zone 1		C IV Line Zone 2		UV Bump	Scott UV	Casebeer UV	
			Low	Lum.	Mid	Lum.	High	Lum.	45.4	0.3	45.8	0.3	45.2	0.5	45.2	0.5			
13.00	45.2	0.5	44.8	0.2	45.2	0.2	45.6	0.2	45.4	0.3	45.8	0.3	45.2	0.5	45.2	0.5	45.2	0.5	0.5
13.02	45.2	0.5	44.8	0.2	45.2	0.2	45.6	0.2	45.4	0.3	45.8	0.3	45.2	0.5	45.2	0.5	45.2	0.5	0.5
13.04	45.2	0.5	44.8	0.2	45.3	0.2	45.6	0.2	45.4	0.3	45.8	0.3	45.2	0.5	45.2	0.5	45.2	0.5	0.5
13.06	45.2	0.5	44.8	0.2	45.3	0.2	45.6	0.2	45.4	0.3	45.8	0.3	45.2	0.5	45.2	0.5	45.2	0.5	0.5
13.08	45.2	0.5	44.8	0.2	45.3	0.2	45.6	0.2	45.4	0.3	45.8	0.3	45.2	0.5	45.2	0.5	45.2	0.5	0.5
13.10	45.2	0.5	44.9	0.2	45.3	0.2	45.7	0.2	45.5	0.3	45.9	0.3	45.2	0.5	45.3	0.5	45.3	0.5	0.5
13.12	45.2	0.5	44.9	0.2	45.3	0.2	45.7	0.2	45.5	0.3	45.9	0.3	45.2	0.5	45.3	0.5	45.3	0.5	0.5
13.14	45.2	0.5	44.9	0.2	45.3	0.2	45.7	0.2	45.5	0.3	45.9	0.3	45.3	0.5	45.3	0.5	45.3	0.5	0.5
13.16	45.3	0.5	44.9	0.2	45.3	0.2	45.7	0.2	45.5	0.3	45.9	0.3	45.3	0.5	45.3	0.5	45.3	0.5	0.5
13.18	45.3	0.5	44.9	0.2	45.3	0.2	45.7	0.2	45.5	0.3	45.9	0.3	45.3	0.5	45.3	0.5	45.3	0.5	0.5

Note. — All of the SEDs are taken to have  $\alpha_x = -1$  above 0.2 keV. Units are  $\log(\text{erg s}^{-1})$ . This table is available in its entirety in a machine-readable form in the journal publication Krawczyk et al. (2013). A portion is shown here for guidance regarding its form and content.

### 3.2.2 Sub-sampled Mean SEDs

While the overall mean quasar SED is a useful tool, examining how the SED changes as a function of various quasar parameters may shed light on the physical processes of the central engine. For example, Richards et al. (2006a) found that bolometric corrections (see Section 3.3) differed by as much as a factor of two in the extremes of quasar types, but with only 259 objects Richards et al. (2006a) did not have the data necessary to comment on what physics is behind the range of bolometric corrections. Marconi et al. (2004) provide a luminosity-dependent bolometric correction, but this is largely dependent on the  $L_{\text{uv}}-\alpha_{\text{ox}}$  relationship and is built into the Richards et al. (2006a) bolometric corrections. What we seek (with the aid of a substantially larger sample) is a more physical understanding of the SED differences and the resulting changes in bolometric correction.

In an attempt to better understand the physics that lead to differences in SEDs (and bolometric corrections), we consider two parameters herein, specifically the UV luminosity and C IV emission line properties. While it is also important to consider SEDs as a function of mass and accretion rate, those quantities are not directly measurable; we will leave that analysis to Chapter 5. Luminosity-dependent SEDs (Section 3.2.2) are of interest because of the known  $L_{\text{uv}}-\alpha_{\text{ox}}$  relationship and strong dependence of accretion disk wind physics on the UV to X-ray flux ratio (e.g. Proga et al., 2000). Examining the mean SED as a function of C IV emission line properties (Section 3.2.2) is interesting because that line may be an indicator of the true SED as it serves as a diagnostic of which two components dominate the broad emission line region (BELR; Richards et al., 2011; Wang et al., 2011). In fact, UV emission lines like C IV, with ionization potentials in the EUV part of the spectrum, may even be an indicator of the unseen EUV part of the SED (see Section 3.4).

#### Luminosity-dependent Mean

The well-known nonlinear relationship between the UV and X-ray luminosities means that the SED (and thus the bolometric correction) *must* be a function of luminosity. As a first test, we have split the sample into three equally populated luminosity bins, each containing 36,061 quasars. Figure 3.7 shows the cumulative histogram of  $\log(\nu L_{\nu}) |_{\lambda=2500\text{\AA}}$  for all quasars, with the vertical lines showing the luminosity cuts. In order to separate the changes that potentially arise from evolution from

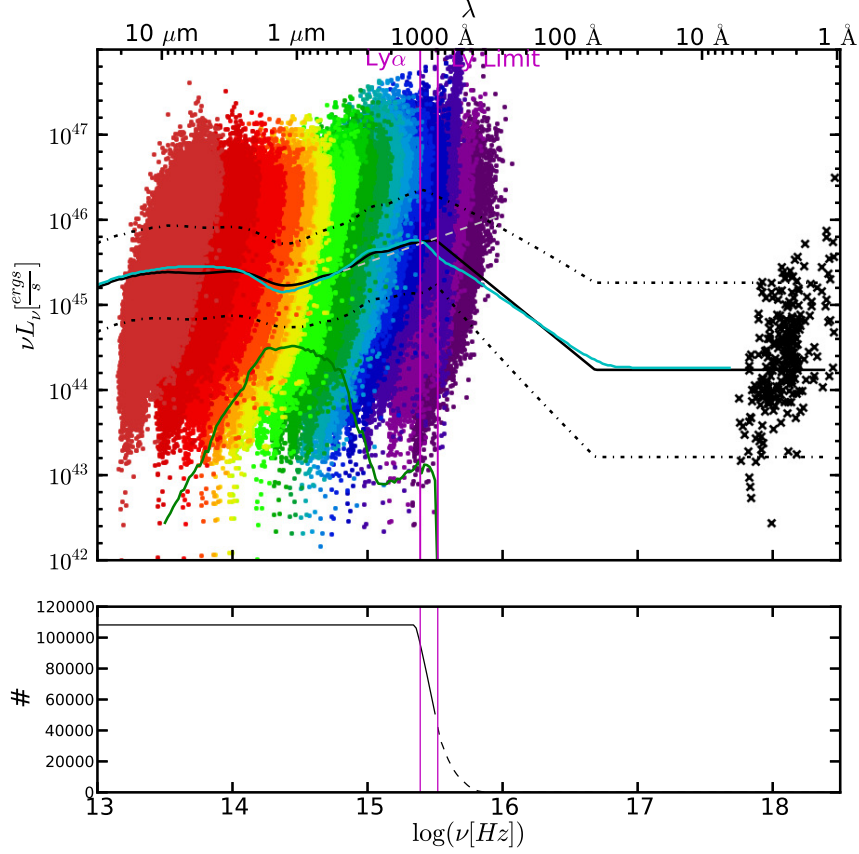


Figure 3.6 Top: mean corrected SED (black) and data points for 108,184 quasars with gap filling, edge filling, host galaxy removal, and spectral corrections (see text). The mean SED from Richards et al. (2006a, cyan), an  $\alpha_\nu = -0.44$  powerlaw (Vanden Berk et al., 2001, dashed grey), a typical elliptical host galaxy (green), and ChaMP X-ray data (Green et al., 2009, black crosses) are included for comparison. The mean has been truncated at the Lyman limit to avoid being biased to high-luminosities when the number of quasars drops off (see text). See legend of Figure 3.4 for color coding of scatter points. Bottom: the number of SEDs averaged at each frequency. The dotted line indicates where the mean SED is truncated and connected with the X-ray. The two vertical magenta lines show the positions of the Ly $\alpha$  line at 1216 Å and the Lyman limit at 912 Å.

those that are luminosity-dependent, we marginalize over redshift by selecting sub-samples from each bin that each have the same redshift distribution. The inset of Figure 3.7 shows the redshift distribution for each of the bins; the shaded region shows the redshift distribution of the sub-samples. This process leaves  $\sim 10,000$  quasars in each luminosity bin as compared to the 259 *total* objects in Richards et al. (2006a) across all luminosity bins.

We calculated the luminosity-dependent mean SEDs in an iterative way. As a first step we follow the same steps as the overall mean SED: we used our gap-filling SED to interpolate/extrapolate over gaps in the photometry with  $\lambda > 912 \text{ \AA}$  and truncated the mean SEDs at 912\AA. These mean SEDs were then connected to the X-ray points determined using the mean UV luminosity for each sample. The resulting mean SEDs were then used as the new gap-filling SEDs for each luminosity bin. For all remaining iterations all missing photometry was gap filled, and the resulting mean SEDs

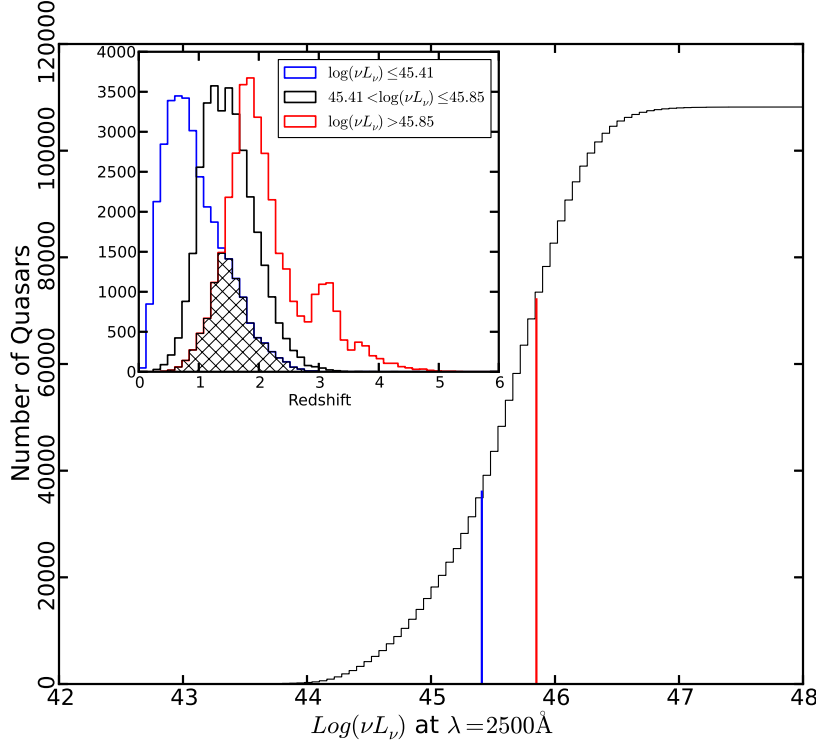


Figure 3.7 Cumulative histogram of  $\log(\nu L_\nu) |_{\lambda=2500\text{\AA}}$  for all non-reddened quasars. Vertical lines show luminosity cuts that result in three equally populated bins. The inset shows the redshift distribution for these three bins, with the overlap shaded in.

were truncated at  $800\text{\AA}$  (where the sampled number starts to fall) before connection to the X-ray. Figure 3.8 shows the mean SEDs and data for each of the luminosity bins after 10 iterations. The iteration process described above ensures that our mean SED follows the quasars with data in each luminosity bin instead of the initial gap filling model. The redshift marginalization process means that the mean redshift of all three luminosity samples is  $z \sim 1.5$ . The mean SEDs are given in tabular form in Table 3.1.

Figure 3.9(a) shows the mid-IR region of the three SEDs when they are normalized at  $1.3\mu\text{m}$  and Figure 3.9(b) shows the optical ( $\lambda < 3000\text{\AA}$ ) and UV region ( $\lambda > 3000\text{\AA}$ ) when normalized at  $1450\text{\AA}$ . The thick lines indicate where a Welch's  $t$  test shows the mean SEDs have less than a 1% chance of being the same ( $p < 0.01$ ). The high-luminosity SED has more hot dust emission (at  $2\text{--}4\mu\text{m}$ ), a small Balmer continuum ( $\lambda < 3000\text{\AA}$ ), a harder (bluer) optical spectrum, and a softer (redder) UV spectrum. The low-luminosity quasars would have to have host galaxies  $\sim 8$  times more luminous than assumed in order for the optical slopes at  $\lambda < 3000\text{\AA}$  to agree between the low-luminosity and high-luminosity SEDs (thus the redder continuum is likely to be intrinsic and not due to host-galaxy contamination). The UV region is sensitive to the Lyman series corrections (Section 3.1.2), but these corrections are not luminosity dependent. The Welch's  $t$  test shows the prominent  $10\mu\text{m}$  silicate bumps in the high-luminosity objects are statistically significant. The IR bumps are discussed in

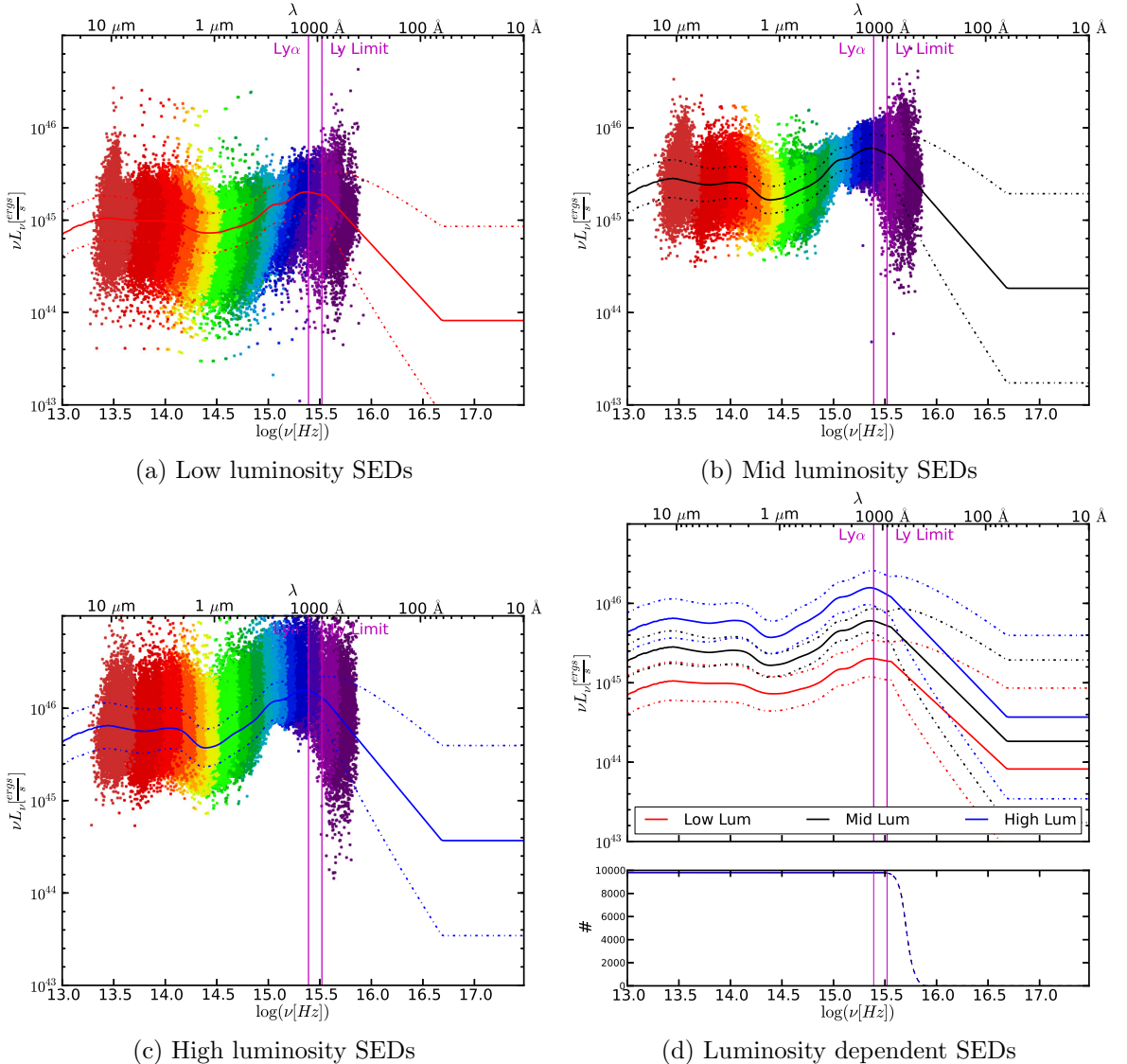


Figure 3.8 Mean SEDs for low ( $\log(\nu L_\nu) |_{\lambda=2500\text{\AA}} \leq 45.41$ ) luminosity quasars (a), mid ( $45.41 < \log(\nu L_\nu) |_{\lambda=2500\text{\AA}} \leq 45.85$ ) (b), and high ( $45.85 < \log(\nu L_\nu) |_{\lambda=2500\text{\AA}}$ ) (c). Panel (d) shows the three curves overplotted. See Figure 3.4 for an explanation of the scatter points in panels (a)-(c) and the bottom histogram of panel (d). The high luminosity SED has more hot dust emission (at 2–4 μm), a smaller Balmer continuum ( $\lambda < 3000\text{\AA}$ ), a harder (bluer) optical spectrum ( $\lambda < 3000\text{\AA}$ ), and a softer (redder) UV spectrum ( $\lambda > 3000\text{\AA}$ ); see Figure 3.9(a) and (b).

more detail in Gallagher et al. (2007).

One of our goals in considering the luminosity-dependent mean is to investigate the shape of the SEDs over  $500 < \lambda_{\text{rest}} (\text{\AA}) < 1200$ . Given the corrections necessary in this region (Section 3.1.2), the shape here is necessarily uncertain; however, the data support a harder slope with lower luminosity (see Figure 3.9(b)). This is consistent with the results of Scott et al. (2004) and suggests that the X-ray flux may not be the only part of the SED that has a nonlinear relationship to  $L_{2500 \text{\AA}}$ . This behavior is also seen in the spectral Principal Component Analysis (PCA) of Yip et al. (2004) who found that their third eigenvector shows an anti-correlation of the continua on either side of Ly $\alpha$ . In short, quasars that are bluer longward of Ly $\alpha$  have softer (redder) continua in the Ly $\alpha$  forest region. This can have important consequences for bolometric corrections; see Section 3.3.

### C IV-dependent Mean

While the Baldwin Effect (Baldwin, 1977) reveals that there is a relationship between the strength of UV emission lines and the continuum luminosity, Richards et al. (2011) have argued that the C IV (and other UV emission lines) properties are better diagnostics of the *shape* of the SED than its absolute scaling. If that is the case, SEDs made as a function of emission line properties such as C IV blueshift and EW (Richards et al., 2011) or PCA (e.g., “Eigenvector 1”; Boruson & Green, 1992; Brotherton & Francis, 1999) may reveal interesting differences. Any such differences would have important implications for bolometric corrections of individual objects.

Thus, in addition to luminosity sub-samples, we have also divided the data as a function of C IV blueshift and rest-frame EW (Richards et al., 2011). To see if the SED shape depends on these properties, we have taken two zones that are representative of extrema in disk-wind structures according to Richards et al. (2011, see also Wang et al. (2011)) : Zone 1, blueshifts  $< 600 \text{ km s}^{-1}$  and EW  $> 50 \text{ \AA}$  (i.e., with “disk-dominated” BELRs) and Zone 2, blueshifts  $> 1200 \text{ km s}^{-1}$  and EW  $< 32 \text{ \AA}$  (i.e., with “wind-dominated” BELRs). These cuts are chosen to have roughly the same number of objects in each sample. In Zone 1 there are 5736 quasars with a mean  $\log(\nu L_\nu) |_{\lambda=2500 \text{\AA}} = 45.9$ , and Zone 2 contains 5713 quasars with a mean  $\log(\nu L_\nu) |_{\lambda=2500 \text{\AA}} = 46.2$ . Figure 3.10 shows the data and mean SEDs for the quasars in each zone. For these mean SEDs, we used the mean mid-luminosity SED for the initial gap repair to *all* the filters and truncated the mean at 800 $\text{\AA}$  before connecting it with the X-ray. We then took the resulting mean SED and used that to gap repair in the same way; this was repeated 10 times. We note that there is a difference in mean luminosity between Zones 1 and 2; however, we have not gap-filled with the luminosity-dependent SEDs in order to isolate any residual differences. The mean SEDs are given in tabular form in Table 3.1.

Our primary interest in these SEDs lies in the UV part of the spectrum; however, it seems that there is relatively little that can be learned about that region from this sample. Seeing C IV requires that the sample is restricted to  $z \gtrsim 1.6$ , which has a number of consequences. In particular, it limits the sample to the highest luminosities and the redshift limit introduces a bias toward LLS (Worseck & Prochaska, 2011), which may be the cause of the steep fall-off beyond Ly $\alpha$ . However we are able to see differences in the optical/UV continuum consistent with eigenvector 1 analyses (Brotherton & Francis, 1999). In particular, Figure 3.9(c) shows that the Zone 1 mean SED has a larger Balmer continuum ( $\lambda < 3000 \text{\AA}$ ) and stronger Ly $\alpha$  emission (the difference in slopes is consistent with being due to stronger C IV and Ly $\alpha$  in Zone 1 mean SED relative to Zone 2 since we have only corrected

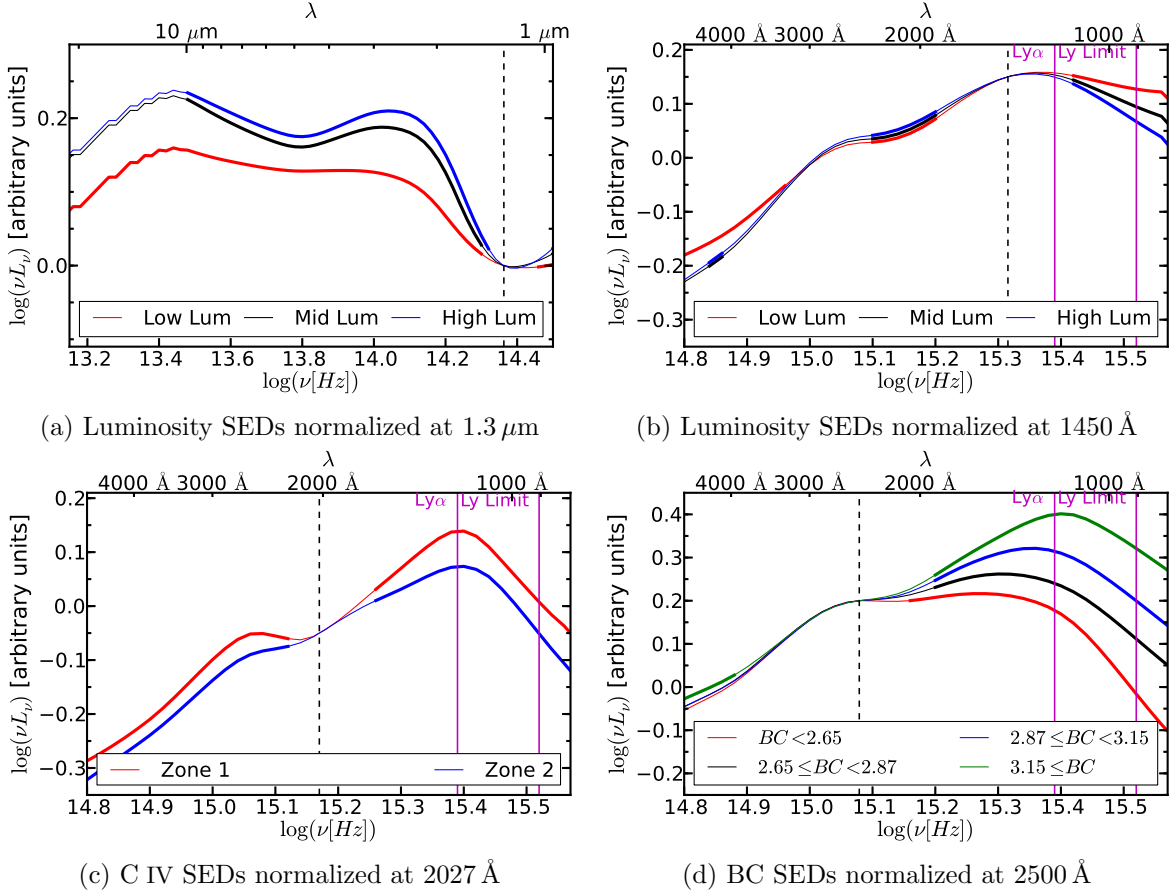


Figure 3.9 Normalized SEDs with the  $y$ -axis showing relative luminosity. The thick lines indicate where the probability of the mean SEDs being the same is less than 1% and the vertical dashed lines indicate the normalization frequency. (a) Luminosity-dependent SEDs normalized at  $1.3\ \mu\text{m}$ ; high-luminosity quasars appear to have more hot dust emission. (b) Luminosity-dependent SEDs normalized at  $1450\ \text{\AA}$ ; high-luminosity quasars have softer EUV continua. (c) C IV-dependent SEDs normalized at  $2027\ \text{\AA}$ . Zone 1 (disk-dominated) quasars have more Balmer continuum and stronger  $\text{Ly}\alpha$  emission than Zone 2 (wind-dominated) quasars. See Figure 3.10. (d) Bolometric correction-dependent SEDs normalized at  $2500\ \text{\AA}$ , showing the effect that most of the range in BC comes from the range of UV and EUV continua (and dust).

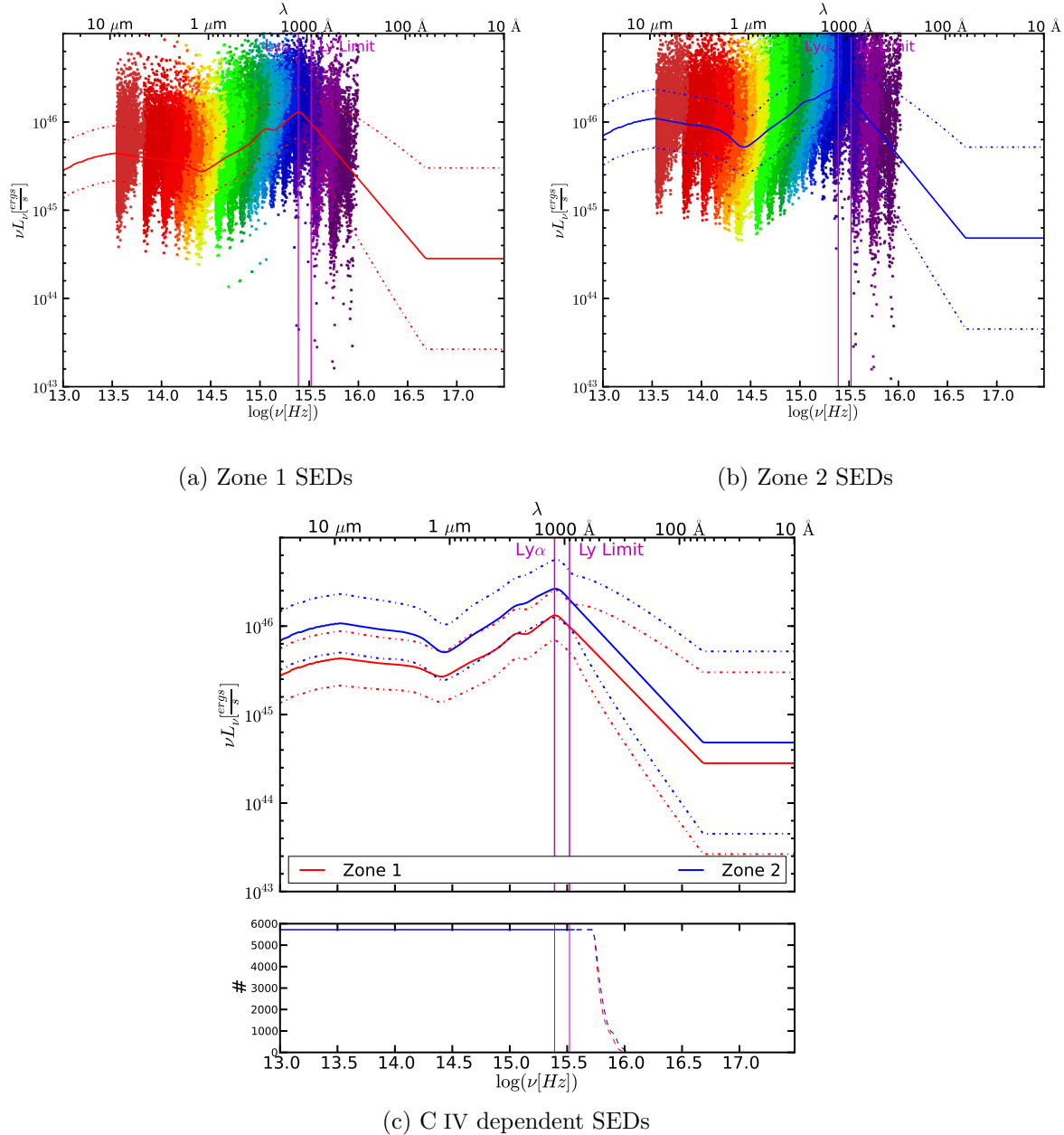


Figure 3.10 Mean SEDs for quasars in two zones of the C IV blueshift vs. C IV EW plane. Panel (a) shows Zone 1: BS < 600 km s<sup>-1</sup> and EW > 50 Å (disk-dominated objects in Richards et al., 2011). Panel (b) shows Zone 2: BS > 1200 km s<sup>-1</sup> and EW < 32 Å (wind-dominated objects in Richards et al., 2011). Panel (c) shows the two curves overplotted. See Figure 3.4 for explanation of scatter points in panels (a and b) and the bottom histogram of panel (c). The zone 1 mean SED shows a larger Balmer continuum ( $\lambda < 3000$  Å) and stronger Ly $\alpha$  emission, consistent with eigenvector 1 analyses. Figure 3.9 shows an expanded version of panel (c).

for the mean emission line contribution). We will further consider differences in the bolometric correction and what can be learned about the shape of the SED as a function of the UV emission line properties in Section 3.3, further investigations of the UV continuum of quasars as a function of C IV emission line properties are certainly warranted.

### 3.3 Bolometric Corrections

One of the main goals of this study is to characterize the bolometric luminosities of quasars. The bolometric luminosity is the integrated area under the SED curve and can be calculated as:

$$L_{\text{bol}} = \int_0^{\infty} L_{\nu} d\nu = \int_{-\infty}^{\infty} \ln(10) \nu L_{\nu} d\log(\nu) \quad (3.5)$$

where Figures 3.4 and 3.6 plot the quantity  $\nu L_{\nu}$ . Normally, we do not have an accurate measurement of the full SED for a quasar, but we can estimate the bolometric luminosity by assuming some SED template and using a known monochromatic luminosity,  $L_{\nu}$ . This “bolometric correction” (BC) is given as:

$$\text{BC}_{\nu} = \frac{L_{\text{bol}}}{\nu L_{\nu}}. \quad (3.6)$$

In the next sections we will discuss our choices for limits of integration, normalization wavelength/frequency, and SED models.

#### 3.3.1 Limits of Integration

As was discussed by Marconi et al. (2004), the full observed SED includes light that is not directed to the observer along its original line of sight. Thus, the SED determined in this manner is not the *intrinsic* one. For example, most of the IR radiation ( $\sim 30 \mu\text{m} - 1 \mu\text{m}$ ) is believed to be produced in a large toroidal dusty region beyond the accretion disk (e.g., Krolik & Begelman, 1988; Elitzur & Shlosman, 2006). The radiation from this “dusty torus” arises from the reprocessing of higher energy photons emitted by the accretion disk and re-radiated by the torus in the IR. Any optical-UV radiation that does not come directly to the observer, but is instead reprocessed by dust, is effectively double-counted when determining the true bolometric luminosity. Because of this effect, Marconi et al. (2004) do not include the IR bump when computing their bolometric corrections. Their choice of integration limits of  $1 \mu\text{m} - 500 \text{ keV}$  is well justified, although strictly speaking the optical/UV bump must also be corrected for dust reddening along the direct line of sight; otherwise, the observed luminosity will be smaller than the true intrinsic luminosity.

Here we describe a similar effect in the hard X-ray band (energies larger than  $2 \text{ keV}$ ). While it is thought that IR flux can include reprocessed disk emission, so too can the hard X-ray emission. The accretion disk itself can emit thermal soft X-ray photons from the inner part of the accretion disk, but hard X-ray photons are believed to come from Compton upscattering of accretion disk photons off hot electrons in the so-called “corona.” Depending on the geometry of the corona, it may or may not be appropriate to include the hard X-ray part of the SED in the bolometric luminosity in the same way that Marconi et al. (2004) suggest avoiding the IR emission. If the corona is a hot spherical region surrounding the black hole (Sobolewska et al., 2004a) then one should exclude the highest energy photons from the tabulation of the “intrinsic” luminosity. However, if the corona is

Table 3.2. Bolometric Luminosities and Bolometric Corrections

SDSS ID	$\nu L_{\text{2500 \AA}}$	$\nu L_{\text{5100 \AA}}$	BC <sub>disk</sub> <sup>a</sup>	$L_{\text{30 \mu m--1 \mu m}}$	$L_{\text{1 \mu m--2 keV}}$	$L_{\text{2 keV--10 keV}}$	$L_{\text{10 keV--500 keV}}$							
587745539970630036	46.06	0.03	45.77	0.07	3.08	0.25	46.27	0.03	46.54	0.01	44.75	0.17	45.11	0.11
587732772647993547	45.35	0.07	44.98	0.04	2.59	0.43	45.52	0.02	45.76	0.02	44.24	0.17	44.60	0.11
587735666930941958	45.68	0.08	45.37	0.06	2.83	0.51	46.13	0.02	46.13	0.02	44.48	0.17	44.84	0.11
58772419827780231	46.31	0.06	46.39	0.08	2.31	0.33	46.78	0.02	46.67	0.01	44.97	0.17	45.33	0.11
587729159520452814	45.85	0.05	45.62	0.06	3.14	0.36	46.22	0.02	46.35	0.02	44.62	0.17	44.98	0.11
588848900997054741	44.71	0.06	44.53	0.07	3.62	0.51	45.02	0.02	45.27	0.02	43.79	0.17	44.15	0.11
588017978340999239	46.91	0.06	46.63	0.03	2.49	0.33	47.25	0.02	47.31	0.01	45.38	0.18	45.74	0.12
587722984428798040	46.29	0.05	46.07	0.07	3.33	0.37	46.47	0.02	46.81	0.01	44.92	0.17	45.28	0.11
587732483289055296	45.50	0.06	45.37	0.04	2.20	0.30	45.94	0.01	45.84	0.01	44.31	0.17	44.67	0.11
587733081880789140	45.54	0.05	45.30	0.04	2.64	0.34	45.91	0.02	45.96	0.02	44.39	0.17	44.76	0.11

<sup>a</sup>Taken over the range of 1  $\mu\text{m}$  to 2 keV.

Note. — All luminosities are reported in  $\log(\text{erg s}^{-1})$ . This table is available in its entirety in a machine-readable form in the journal publication Krawczyk et al. (2013). A portion is shown here for guidance regarding its form and content.

more like a patchy skin to the accretion disk as in Sobolewska et al. (2004b), including the hard X-ray flux in the SED would be more appropriate. Our solution here is an agnostic one; instead of presenting the full integrated luminosity, we will give it in four pieces: 30  $\mu\text{m}$ –1  $\mu\text{m}$ , 1  $\mu\text{m}$ –2 keV, 2 keV–10 keV, and 10 keV–500 keV (see Table 3.2), allowing the user to determine which approach is best. Although, given the small amount of data and the large uncertainties in the X-ray, we do not recommend taking BCs based on monochromatic X-ray luminosities as proposed by Vasudevan & Fabian (2007).

### 3.3.2 Normalization Wavelength

Typically, bolometric corrections are computed with respect to 5100 Å and we will report those values herein for backward compatibility with previous work. However, we will generally report BCs relative to 2500 Å. There are a number of reasons for this choice. While 5100 Å makes sense for low-redshift sources, especially when using the H $\beta$  line to estimate black hole masses and then the Eddington ratio from the ratio of  $L_{\text{bol}}$  to  $M_{\text{BH}}$ , that rest-frame wavelength is inaccessible for the vast majority of SDSS quasars. The SDSS quasar sample peaks at  $z \sim 1.5$ , which corresponds to rest-frame spectral coverage of  $\sim 1500$ –3700 Å. As such, the majority of SDSS quasars have observed flux density measurements at 2500 Å. For this reason, Richards et al. (2006b) chose to  $K$ -correct to  $z = 2$  where the SDSS  $i$ -band roughly corresponds to  $\lambda_{\text{eff}} = 2500$  Å. Moreover, 2500 Å is typically used as the optical anchor point in the  $L_{\text{uv}}-\alpha_{\text{ox}}$  relationship. In addition to this, the 5100 Å luminosity always has a larger host galaxy contamination. As such, we have chosen to use 2500 Å as our fiducial wavelength.

### 3.3.3 Integrated Luminosities and Bolometric Corrections

For comparison with previous work, we compute the bolometric luminosity in a number of ways, including the tabulation of integrated optical and IR luminosities. In terms of bolometric corrections, we start by computing BCs for each individual object in our sample, and, with those, compute mean BCs for the full sample. In computing BCs we used SEDs constructed as discussed above: namely, using broadband observations where available, the  $L_{\text{uv}}-\alpha_{\text{ox}}$  relationship, and “gap-filling” (with

the mid-luminosity mean SED) as needed. The overall mean BC<sub>2500 Å</sub> and corresponding standard deviation values are  $2.75 \pm 0.40$  using limits of  $1\text{ }\mu\text{m}$  and  $2\text{ keV}$  (hereafter called  $L_{\text{disk}}$ , which avoids the issue of IR and hard X-ray double counting); at  $5100\text{ \AA}$  this corresponds to  $4.33 \pm 1.29$ . For comparison with Elvis et al. (1994) and Richards et al. (2006a) we also determine the bolometric correction to  $5100\text{ \AA}$  in the range of  $30\text{ }\mu\text{m}$  up to  $10\text{ keV}$ . We find BC<sub>5100 Å</sub> =  $7.79 \pm 1.69$ , as compared to the results of Elvis et al. (1994) and Richards et al. (2006a) who found  $11.8^{+12.9}_{-6.3}$  and  $10.3 \pm 2.1$  respectively. Using the range  $1\text{ }\mu\text{m}$  to  $500\text{ keV}$  from Marconi et al. (2004) we find that BC<sub>2500 Å</sub> =  $2.97 \pm 0.43$ .

Recent studies by Nemmen & Brotherton (2010) and Runnoe et al. (2012) suggest the relationship between a quasar's monochromatic and bolometric luminosity is nonlinear. As is expected given the nonlinear relationship used to connect the UV and the X-ray, we also find this to be the case; our best fit is a powerlaw of the form:

$$\begin{aligned} \log(L_{\text{Bol}}) = & (0.9869 \pm 0.0003) \log(\nu_{2500\text{ \AA}} L_{2500\text{ \AA}}) \\ & + (1.051 \pm 0.014) \end{aligned} \quad (3.7)$$

Note that while we allow for a nonlinear slope, the best-fit slope is very close to linear. The errors quoted on this fit are small because of our large sample size and only statistical, not systematic, errors are included.

In addition to mean BCs, we give BCs and error estimates for each of the objects in our sample; these are shown by the points and contours in Figure 3.11. As did Marconi et al. (2004), we investigate how the BCs are dependent on quasar luminosity and, in turn, on the  $L_{\text{uv}}-\alpha_{\text{ox}}$  relation that was assumed. The black dotted line in Figure 3.11 shows the luminosity-independent BC that one gets for our mean SED and assuming a linear dependence between  $L_{\text{uv}}$  and  $L_x$ (i.e. re-normalizing the mean SED without changing  $\alpha_{\text{ox}}$ ). To illustrate the importance of the observed nonlinear correlation between  $L_{\text{uv}}$  and  $L_x$  we do the following. We re-normalize our mean SED to  $L_{2500\text{ \AA}}$  values that span the range shown in Figure 3.11, stepping in small increments. We then truncate the mean SED at  $1216\text{ \AA}$  and connect it to  $0.2\text{ keV}$  using the  $L_{\text{uv}}-\alpha_{\text{ox}}$  relationship and assuming  $\alpha_x = -1$  beyond  $0.2\text{ keV}$ . We then calculate the resulting BCs over a range of luminosities; the results are given by the dashed blue line in Figure 3.11. This line tracks the outliers well, but the core of our sample shows a weaker luminosity dependence to the BCs (as expected from Equation 3.7). This weaker luminosity dependence may reflect the trend of redder optical continua in low-luminosity quasars are bluer optical continua in high-luminosity quasars, which would counteract the trends in  $\alpha_{\text{ox}}$  with  $L_{\text{uv}}$ .

We have also included the line found by Marconi et al. (2004, maroon) for comparison. This line has been adjusted to match our limits of integration and the BC normalization wavelength. We see that the form of the Marconi line and ours are similar, and the offset is due to the fact that the Marconi SEDs use a shallower  $L_{\text{uv}}-\alpha_{\text{ox}}$  relation that is extrapolated to  $2\text{ keV}$  (which would predict a soft X-ray excess in all quasars), whereas we use a steeper  $L_{\text{uv}}-\alpha_{\text{ox}}$  relation extrapolated to  $0.2\text{ keV}$ .

The general shape of the distribution of individual BCs shows that the main luminosity dependence of our BCs is indeed due to the  $L_{\text{uv}}-\alpha_{\text{ox}}$  relation. We do, however, see a large spread of  $\sim 1$  on either side of the dashed line. In particular, it is possible for a high- $L$  quasar to have a BC that

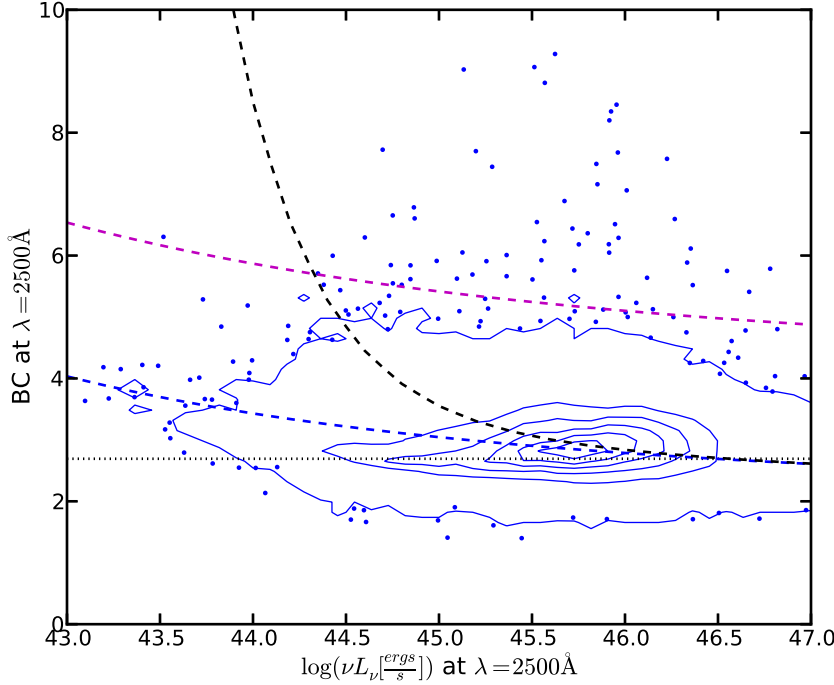


Figure 3.11 Disk bolometric correction as a function of UV luminosity,  $L_{\text{2500}\text{\AA}}$ . The blue contours and scatter points shows a density plot for our quasar sample. The contours indicate the linear density of scatter points on the plot. The black dotted line is the bolometric correction for the overall mean SED (see Figure 3.6) without taking into account the nonlinear correlation between  $L_{\text{UV}}$  and  $L_{\text{X}}$ . The blue dashed line shows the  $L$ -dependence of the BCs assuming the  $L_{\text{UV}} - L_{\text{X}}$  relation (Steffen et al., 2006); this line tracks the data points since the individual BCs are also dependent on  $L_{\text{UV}}$ . The black dashed line shows the same relation with an extra bump added in the EUV (see Section 3.4). For comparison the relationship from Marconi et al. (2004) is shown as the dotted maroon line scaled to the limits of integration and to 2500Å.

is higher than a low- $L$  quasar even though the general trend is in the other direction.

In order to facilitate the determination of bolometric corrections using different limits of integration and normalizing wavelengths, in Table 3.2 we have tabulated the integrated luminosity and errors for individual SEDs over  $30\text{ }\mu\text{m}$ – $1\text{ }\mu\text{m}$ ,  $1\text{ }\mu\text{m}$ – $2\text{ keV}$ ,  $2\text{ keV}$ – $10\text{ keV}$ , and  $10\text{ keV}$ – $500\text{ keV}$ . The second range is our recommended range as it corresponds to  $L_{\text{disk}}$ , but the sum of the first three ranges matches that used by Richards et al. (2006a) and the sum of the last three ranges is that used by Marconi et al. (2004). We further give  $L_{\text{5100}\text{\AA}}$ ,  $L_{\text{2500}\text{\AA}}$ , and the resulting  $\text{BC}_{\text{2500}\text{\AA}}$  (relative to  $L_{\text{disk}}$ ). We have not corrected for non-isotropic emission (i.e. the emitted light is not the same in all directions) in our tabulations; however, taking anisotropy into account, Runnoe et al. (2012) suggest scaling the bolometric luminosities by 0.75 when calculating the bolometric luminosity over the range of  $1\text{ }\mu\text{m}$ – $10\text{ keV}$ .

With individual BCs for each quasar, we are able to construct BC-dependent mean SEDs using  $\text{BC}_{\text{disk}}$ . For this we split our sample into four equally populated bins:  $\text{BC} < 2.65$ ,  $2.65 \leq \text{BC} < 2.87$ ,

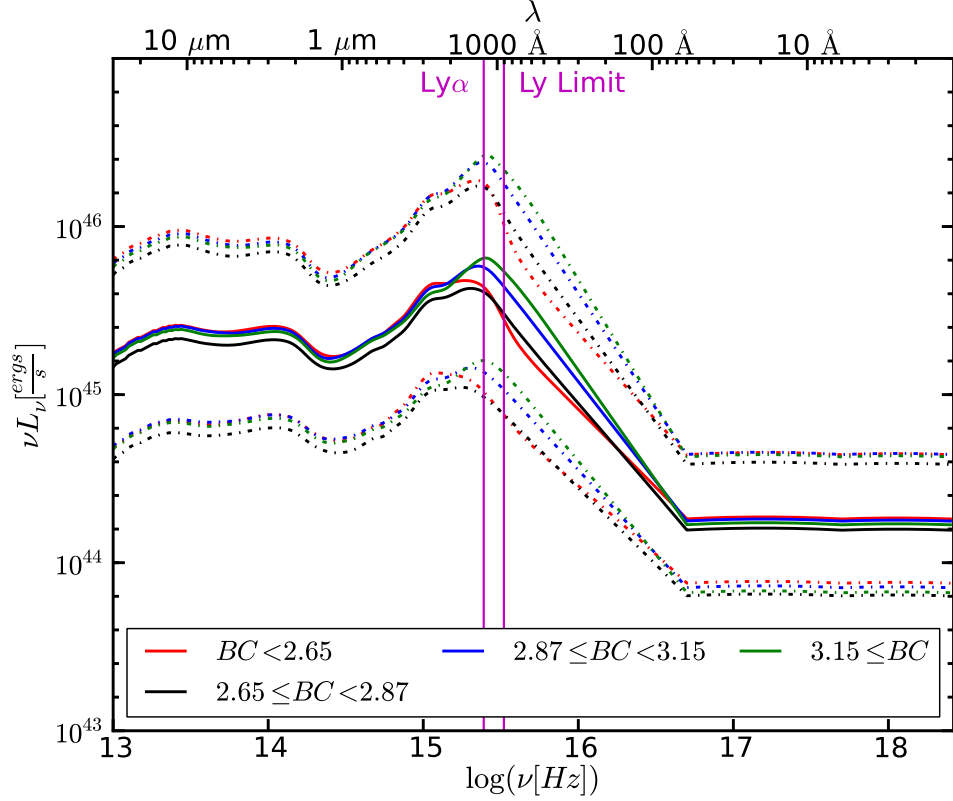


Figure 3.12 Mean SEDs for four bolometric correction bins. The higher BC SEDs show more emission in the UV–EUV part of the SED ( $\lambda \lesssim 2000 \text{ \AA}$ ) and an overall higher luminosity. The steep drop-off of the low-BC SED shortward Ly $\alpha$  could be caused by unaccounted for dust reddening (see end of Section 3.3.3 for details). Figure 3.9 shows an expanded version of the UV section of this plot.

$2.87 \leq \text{BC} < 3.15$ , and  $\text{BC} \geq 3.15$ , each containing  $\sim 29,000$  quasars. Unlike the luminosity- and C IV-dependent SEDs, these mean SEDs do not truncate the individual SEDs and connect the mean to the X-ray, but instead connects each individual SED to the X-ray and then takes the mean. This is done since each SED needs to be connected to the X-ray in order to calculate the BC. Figure 3.12 shows the resulting means and Figure 3.9(d) shows the UV region when the SEDs are normalized at  $2500 \text{ \AA}$ . From these figures we see that the mean SEDs only differ significantly in the UV ( $\lambda \lesssim 2000 \text{ \AA}$ ) and the largely unknown regions of the SED in FUV could have significant effects as compared to the differences seen over  $1000\text{--}2000 \text{ \AA}$  where the SED is well-measured. Although they were not included in the mean SEDs, the 11,468 quasars that show signs of significant dust reddening ( $\Delta(g - i) > 0.3$ ) all fall in the two lowest BC bins; this is expected since quasars with heavy dust reddening will appear to have a smaller BC. This cut only accounts for strong dust reddening; if there is only a small amount of dust reddening then a high-BC quasar could easily fall into the low-BC bin. We might expect the low-BC bin to be contaminated by quasars with mild dust reddening, which could be the cause of the steep drop-off in the low-BC SED just past Ly $\alpha$ .

### 3.4 Discussion: The Unseen EUV Continuum

One of the reasons that we explored the mean SED in subsamples as a function of various quasar parameters is that we expect that the diversity of quasar properties (especially in broad emission lines) is a direct consequence of the diversity in SEDs (e.g., Richards et al., 2011). In particular, quasars with significant UV luminosity relative to the X-ray are capable of driving strong winds through radiation pressure on resonance line transitions (Murray et al., 1995; Proga et al., 2000). Given the nonlinear relationship between  $L_{\text{uv}}$  and  $L_{\text{x}}$  (e.g., Steffen et al., 2006), one might expect to see significant differences in the SEDs of quasars as a function of luminosity. Richards et al. (2011) have argued that a potential wind diagnostic may be the properties of the C IV emission line in the context of the Boroson & Green (1992) eigenvector 1 parameter space which looked at the difference between quasars using principal component analysis. This was the main motivation for exploring the mean SED as a function of these parameters in Section 3.2. While we saw significant differences in the mean SEDs as a function of luminosity, we saw fewer differences between the C IV composites than might have been expected.

While it is possible that the SEDs of quasar extrema (in UV emission) truly are similar, it is difficult to understand how BELR properties could be so different, yet have similar SEDs. For example, there is a large range in the strength of the He II 1640 line (with an ionization potential of 54.4 eV) in Figures 11 and 12 of Richards et al. (2011). As such, we are led to a similar conclusion as Netzer & Davidson (1979), Korista et al. (1997), Done et al. (2012), and Lawrence (2012)—namely that the EUV SEDs may be quite different from the standard powerlaw parameterization between the optical and X-ray. This variation could be in a number of forms, including a second bump in the EUV or simply that the SED seen by the BELR is different from what we view (e.g., Korista et al., 1997).

Here we suggest that the solution may be more than just a different mean SED in the EUV than is normally assumed, but rather that the shape of the EUV SED must be quite different for quasars at opposite extrema in terms of their BELR properties; i.e., there is *no* universal quasar SED (even after accounting for the  $L_{\text{uv}}-\alpha_{\text{ox}}$  relationship)! While Grupe et al. (2010) find that only a factor of a few difference can be hidden in the EUV, their sample is restricted to low-redshift AGNs, whereas our suggestion is that the differences might be significant when considering the extremes of the distribution as spanned by the full SDSS quasar sample. In terms of a model where the BELR emission comes from both disk and wind components (Collin-Souffrin et al., 1988; Leighly et al., 2004), quasars with strong winds would have a weaker EUV continuum than quasars with strong disk components. What Richards et al. (2011) refer to as disk-dominated objects have emission line features that are consistent with a much harder EUV SED than the wind-dominated objects (Kruczek et al., 2011). If the SEDs over the *observable* range of the EM spectrum are similar, the *unseen* part of the EM spectrum may yield very different SEDs. This hypothesis is consistent with radiation line driving being sensitive to the UV to ionizing flux ratio (Proga et al., 2000).

If this hypothesis is correct, it would have important consequences for the determination of bolometric corrections (and thus  $L/L_{\text{Edd}} \propto L_{\text{Bol}}/M_{\text{BH}}$ ). A full investigation into the range of EUV continuum properties is beyond the scope of this paper; however, herein we have created some examples showing how different these values might be for different assumptions of the EUV SED at

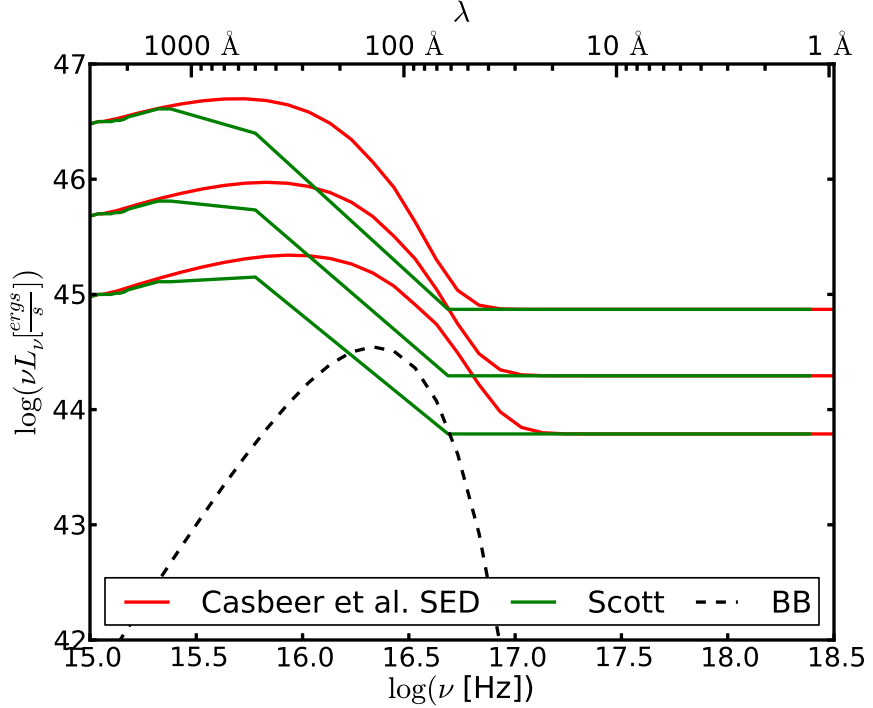


Figure 3.13 The three models we used to represent the EUV part of our SEDs at three luminosities. The Casebeer et al. model is shown in red and the Scott+ $L_{\text{uv}}-L_{\text{x}}$  model in green. The black dashed line shows a blackbody with a peak energy of 23 eV and normalized so it peaks with  $\log(\nu L_\nu) = 44.5$ . These models show the differences between the observed and theoretical models shortward of Ly $\alpha$  as a function of luminosity and illustrate the relative level of our hypothetical extra EUV component.

the extrema of BELR properties.

The most obvious deviation from our baseline prescription (using  $L_{\text{uv}}-\alpha_{\text{ox}}$  to describe the unseen part of the SED) follows from the work of Scott et al. (2004) in the FUV. The UV spectral index just shortward of Ly $\alpha$  was found to be different by Telfer et al. (2002) and Scott et al. (2004) ( $\alpha_{\text{FUV}} = -1.42$  as compared to  $\alpha_{\text{ox}} = -1.54$  for the average quasar luminosity). These differences can be explained by a luminosity-dependent spectral index given in Equation (1.12) (Scott et al., 2004) that is similar to that seen for  $\alpha_{\text{ox}}$  and by the fact that these two samples probe different ranges of  $L_{\text{uv}}$ . Thus, we create  $L$ -dependent model SEDs that do not just connect 2500 Å directly to 0.1 keV, but instead that connect 2500 Å first to 500 Å following Equation 1.12 and then connect 500 Å to 0.2 keV using the  $L_{\text{uv}}-\alpha_{\text{ox}}$  relationship to set the X-ray continuum level. Such an SED is illustrated (green lines) in Figure 3.13 for three different luminosities, where it can be seen that these SEDs have a small (luminosity-dependent) excess of EUV flux as compared to a powerlaw fit between the optical and the X-ray.

We compare this to model SEDs taken from Casebeer et al. (2006) that are adapted from the CLOUDY (Ferland, 2002) so-called “AGN” continuum. The functional form of this continuum is given in Casebeer et al. (2006, Equation (A1)). Essentially this SED consists of a powerlaw representing the optical/UV continuum with exponential cutoffs in the infrared and UV, plus a powerlaw in the X-rays, where the normalization of the two components is set by  $\alpha_{\text{ox}}$  (calibrated to

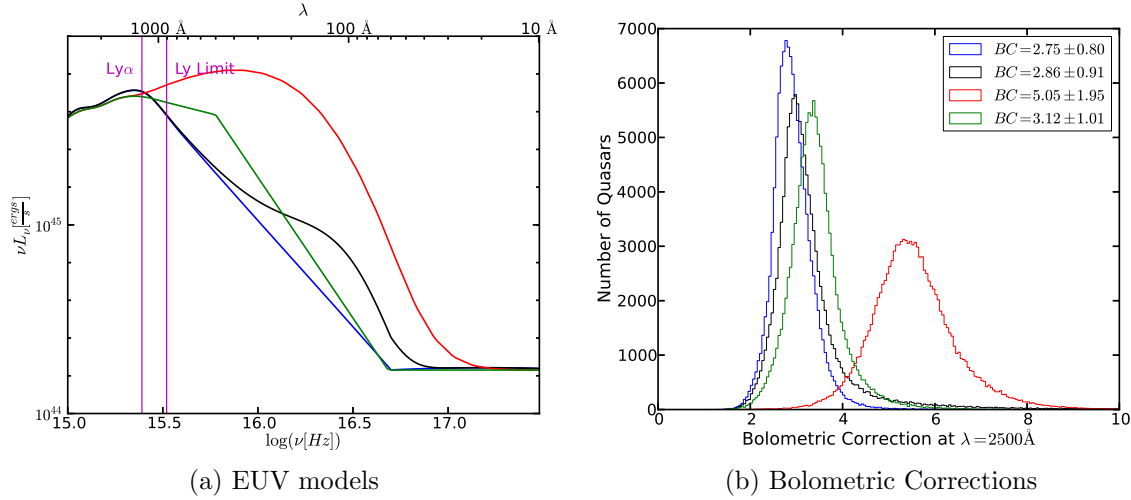


Figure 3.14 (a) Mean SEDs for four different models:  $L_{\text{uv}} - L_x$  from Steffen et al. (2006, blue), the  $L_{\text{uv}} - L_x$  relation with a 23 eV blackbody with a peak value of  $\log(\nu L_\nu) = 45$  (black), using the EUV extension from Scott et al. (2004, green), and the Casebeer et al. model (Casebeer et al., 2006, red). (b) Bolometric corrections for the four models in (a) where the bolometric luminosity is taken from  $1 \mu\text{m}$  to  $2 \text{ keV}$  ( $L_{\text{disk}}$ ). The errors in the legend give the  $2\sigma$  levels of the BC distributions. Models similar to all of those shown here are arguably well-justified and used in the literature. Their differences emphasize the need to better understand the distribution of EUV continua in quasars.

Wilkes et al., 1994). Casebeer et al. (2006) used a range of  $\alpha_{\text{ox}}$  and UV cutoffs to test the influence of the SED on emission line ratios (and not to determine BCs); we show in Figure 3.13 the ones with  $kT_{\text{cut}} = 50, 37, 27 \text{ eV}$  and  $\alpha_{\text{ox}} = -1.5, -1.57, -1.66$ , from lowest to highest luminosity respectively (chosen to have the same optical luminosities as the Scott lines).

While we cannot directly measure the EUV part of the spectrum, it is interesting to compare the Scott and Casebeer et al. SEDs in the  $\sim 800 \text{ \AA}$  range. For low-luminosity quasars, the data-driven Scott-based SED and the more theoretical (but empirically calibrated) Casebeer et al. SED (chosen to have the same  $\alpha_{\text{ox}}$ ), follow the same upward trend. This leads one to wonder if low-luminosity objects may indeed have much more EUV flux shortward of  $500 \text{ \AA}$  (i.e., that the Casebeer et al. 2006 model is correct) than is typically assumed when applying the  $L_{\text{uv}} - \alpha_{\text{ox}}$  prescription, as the EUV is unconstrained for the green curves between  $500 \text{ \AA}$  and  $0.2 \text{ keV}$ . However, for the high-luminosity quasars, the Scott and Casebeer et al. SEDs do not follow the same trend even at  $\sim 800 \text{ \AA}$ , which suggests a model like the Casebeer et al. (2006) SED likely overestimates the EUV emission in the most luminous quasars. Indeed, a comparison of the UV emission lines in the extrema shown in Figure 12 of Richards et al. (2011) suggests that the SEDs of quasars with “disk”- and “wind”-dominated BELRs may be very different in the range of  $\sim 50 \text{ eV}$  where the ionization potentials of many UV lines lie (e.g., Richards et al., 2011, Figure 13).

Since the wind-dominated objects are more luminous on average than the disk-dominated objects (as can be seen in Figure 3.10(c)), we also consider a model where we add a blackbody component of fixed luminosity, such that it is significant in low-luminosity sources, but contributes little to the EUV continuum for high-luminosity sources.

To construct a toy model to illustrate such a situation, we start by extending our SEDs to the X-ray using the Steffen et al. (2006)  $L_{\text{uv}}-\alpha_{\text{ox}}$  relation and then added a blackbody peaking at 23 eV. This peak was chosen in order to add photons of the typical energy needed to produce the spectral lines we see (e.g., C IV and He II). The normalization of the blackbody was taken to have  $\log(\nu L_\nu) = 44.5$  at its peak (see the dashed black curve in Figure 3.13) so that the highest luminosity quasars remain unaffected but the lower luminosity quasars gain an extra feature which has the correct sign to explain the broad range of EWs for, e.g., C IV and He II (Richards et al., 2011). This model leads to a larger spread in their bolometric corrections than when no extra component is used (see Figure 3.14(b)). While we lack direct observational evidence for such a component, the range of emission line strengths for lines with ionization potentials of  $\sim 50$  eV, suggest that some, but not all, quasars have a need for more ionizing flux in this region of the EM spectrum in order to understand their emission line properties. We include it here as a way to illustrate how significantly such a component would change the bolometric corrections of low-luminosity quasars.

We compare these four models, which were chosen to bracket the range of reasonable EUV shapes for a given  $\alpha_{\text{ox}}$ , shown in Figure 3.14(a) for a single luminosity. Figure 3.14(b) then shows how the BC distribution would change under the assumption of each of these models. The biggest deviation from the standard model results when using the Casebeer et al. SEDs. These SEDs may have too much EUV flux for high-luminosity sources, while being more reasonable at low-luminosities (see Figure 3.13). On the other hand, the Scott-based and extra EUV component SEDs depict a more subtle shift in the mean BCs. More importantly, however, is that these deviations from our standard SED produce BC changes that are *systematic* with  $L_{\text{uv}}$ . Although there is a lack of data in the EUV, in Figure 3.11, the dashed black line shows how much we would expect the BCs to change for low-luminosity sources if there were an extra EUV continuum component. Adding the  $L$ -dependence from Scott to this model would make this contrast even stronger.

While this extra EUV component is speculative, the ramifications are such that it is important to consider the possibility. Moreover, the  $L$ -dependence of the FUV continuum based on the work of Scott et al. (2004) already suggests that a correction in this direction is needed. Achieving a better understanding of the EUV continuum is clearly of importance for understanding quasar physics, as a change of a factor of a few in BCs for low-luminosity sources translates to the same correction factor for both  $L_{\text{bol}}$  and the Eddington ratio (i.e., accretion rates). Ideally, we would also like to consider the BC distribution as a function of quantities like the accretion rate, but such analysis is difficult without first understanding any systematic effects in the unseen EUV part of the spectrum.

### 3.5 Conclusions

We have compiled a sample of 119,652 quasars detected in the SDSS. These data are supplemented with multi-wavelength data spanning from the mid-IR through the UV (Table 2.1). This data set was used to construct a new mean SED consisting of 108,184 non-reddened quasars, with rest frame coverage from  $\sim 20 \mu\text{m} - 912 \text{\AA}$  (Table 3.1). By splitting our sample into luminosity bins we constructed three luminosity-dependent mean SEDs and found  $\alpha_{\text{FUV}}$  to be dependent on luminosity in the sense that more luminous quasars have redder  $\alpha_{\text{FUV}}$  continua (Figure 3.9(b)), consistent with Scott et al. (2004). In addition, the high-luminosity quasars also show signs of having bluer optical

continua (Figure 3.9(b)) and more hot dust emission than the low-luminosity quasars (Figure 3.9(a)). When splitting our sample based on C IV properties we saw differences in the Balmer continuum, Ly $\alpha$  and C IV (by construction) line strengths (Figure 3.9(c)) that are consistent with eigenvector 1 trends (Brotherton & Francis, 1999).

We also constructed SEDs for each quasar and, from those, found bolometric corrections (Table 3.2). The overall mean is  $BC_{2500\text{ \AA}} = 2.75 \pm 0.40$  using integration limits of  $1\text{ }\mu\text{m}$ – $2\text{ keV}$ . While the range of bolometric corrections indicated by the IR through NUV data alone is reasonably small, there can be significant changes in the distribution of bolometric corrections when different models are assumed in the unseen EUV part of the SED (Figure 3.14(b)). Although more work has to be done to determine which model should be used in the EUV, it is nevertheless clear that it is important to consider potentially significant differences in the EUV part of the SED at the extrema of quasar properties (e.g., in luminosity and in eigenvector 1 parameter space). In Chapter 5, we will further explore the cause(s) of the width in the bolometric correction distribution (after correcting for known luminosity trends) and will characterize the systematic error in the accretion rate estimates.

## Chapter 4: Dusty Quasars

In this chapter we aim to identify the type of dust extinction present in the observed population of quasars and to construct de-reddened quasar SEDs for a subset of the Sloan Digital Sky Survey’s (SDSS) 7th data release (DR7) quasar catalog (Schneider et al., 2010). By distinguishing between objects that are intrinsically red and those that are dust reddened, we can also comment on the broad emission (e.g., Richards et al., 2003) and broad absorption line (e.g., Reichard et al., 2003a,b) properties of quasars as a function of their intrinsic color (and the amount of dust reddening). These emission line properties can help to reveal the SED shape outside of the range covered by our data, as a function of the masses, and/or inclinations that correlate with intrinsic color. To this end this chapter is structured as follows: §4.1 focuses on the identification and fitting of various dust reddening models including individual reddening values for each quasar in our sample. We analyze composite spectra as a function of these fitted values in §4.2 and present our conclusions in §4.3. The data used throughout this chapter are presented in §2.5.

### 4.1 Fitting Reddening Models to Quasar Photometry

#### 4.1.1 Modal Colors

To identify a quasar as “red,” we must first determine both the expected distribution of SEDs and a method for identifying which quasars can be considered as outliers from that distribution. The expected observed SED changes as a function of redshift as the different spectral lines are shifted through the filter sets. By examining quasar colors as a function of redshift we can find the typical quasar SED, and assuming this SED contains little or no dust, we can use it to characterize the effects that different reddening laws have on the SED.

Previous studies have mitigated against emission lines changing a quasar’s colors by binning the data by redshift and removing the median (e.g., Richards et al., 2003) or mode (e.g., Hopkins et al., 2004) within each bin. The results of this process are strongly dependent of the bin width chosen. To avoid this issue, we used a non-parametric 2nd degree local regression to estimate the modal color as a function of redshift. We used the `loess` regression package in R with smoothing parameters chosen so the regression followed the ridge-line (i.e. the mode) for each color-redshift plot, as in Figure 4.1. Although this method does not work well once a filter passes into the Lyman forest (vertical dashed lines in Figure 4.1), with the rest frame wavelength cuts applied in the analysis, this discrepancy does not affect our results.

With these modal colors, we define relative colors (Richards et al., 2003) as the difference between the observed color and the modal color at the quasar’s redshift (e.g.  $\Delta(u-g) = (u-g) - \langle u-g \rangle_{\text{mode},z}$ ). From these relative colors we can also build relative magnitudes ( $\Delta m$ ) up to a normalization factor; we adopt  $\Delta m_{\text{iband}} = 0$  throughout this paper. These relative colors and magnitudes allow for a color analysis that is independent of emission line effects.

To determine if we have a population of quasars affected by dust reddening, we compare the

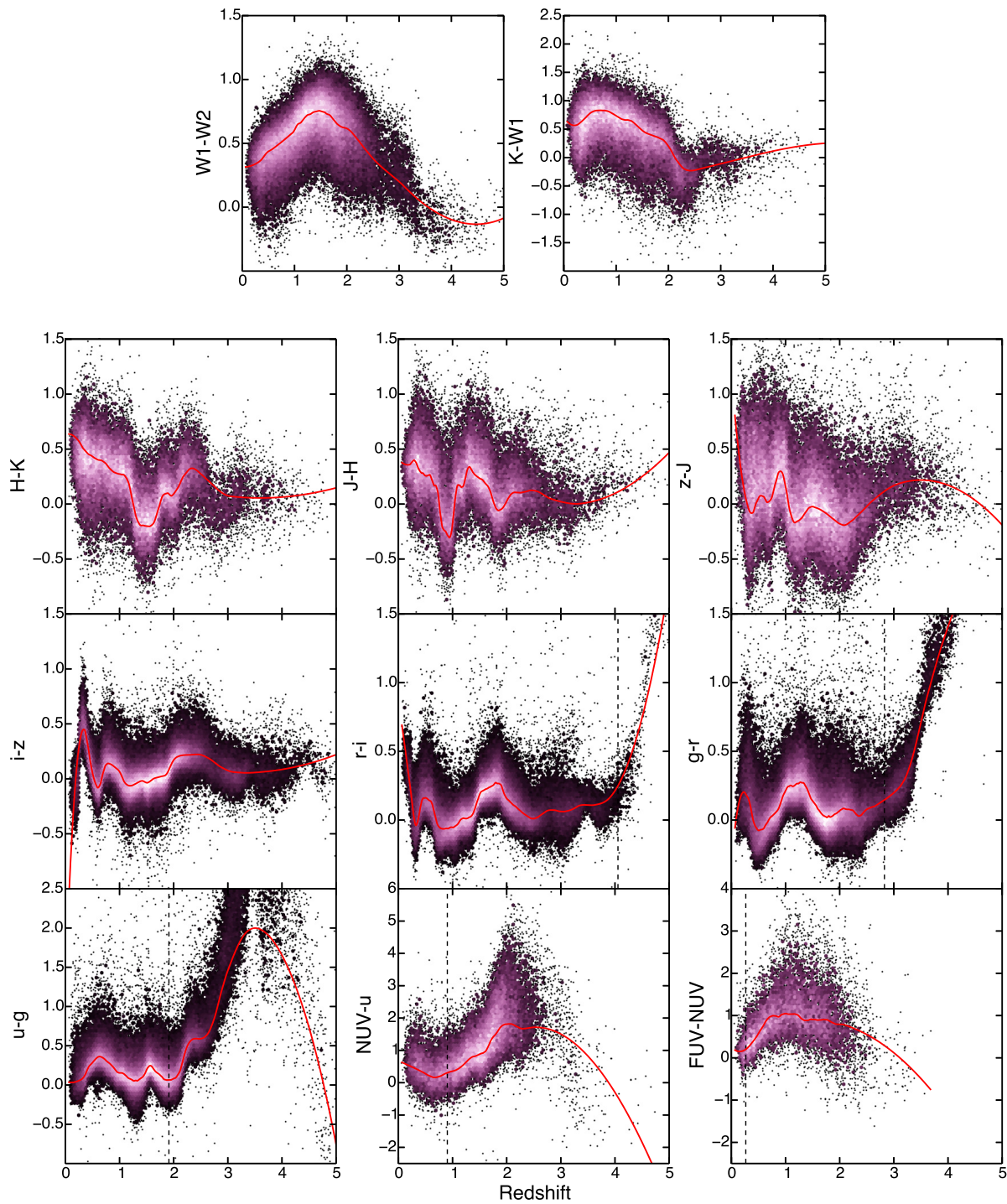


Figure 4.1 Colors as a function of redshift with the modes indicated by the red lines. The colors indicate the linear density of points with white being most dense and the outliers shown as black points. The vertical dashed lines indicate the redshift where each color passes into the Ly $\alpha$  line.

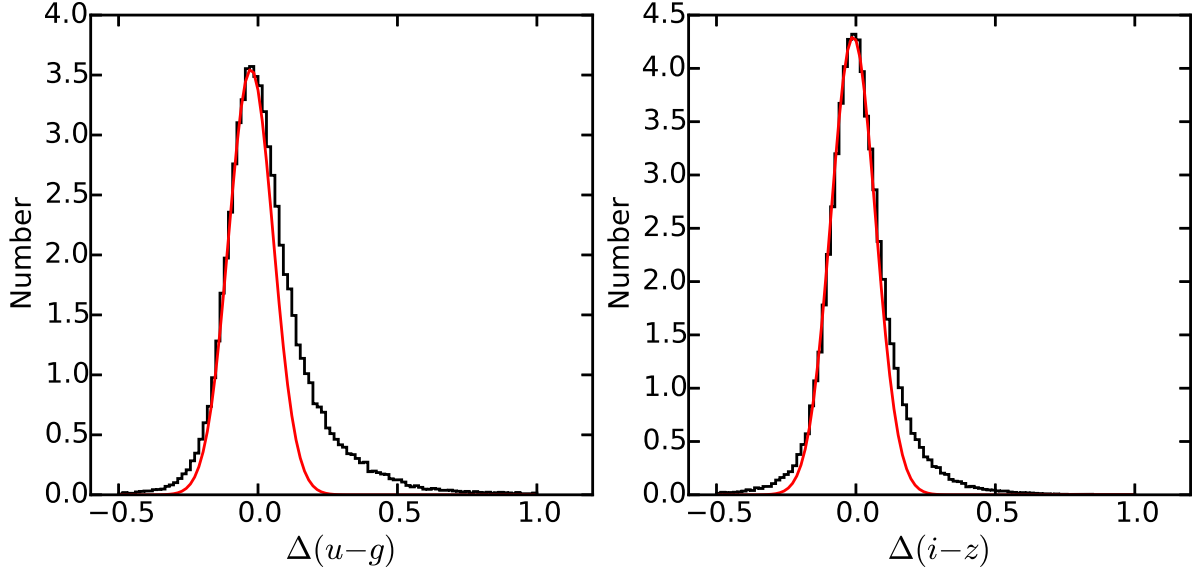


Figure 4.2 Relative colors for  $\Delta(u-g)$  (left) and  $\Delta(i-z)$  (right).  $\Delta(u-g)$  shows a heavy red tail as compared to its best fit Gaussian (red), while  $\Delta(i-z)$  shows a weaker red tail as compared to its best fit Gaussian. This asymmetry indicates that there is a population of dust reddened quasars in our sample.

distributions for a relative color on the blue end of the quasar SED ( $\Delta(u-g)$ ) and relative color on the red end of the quasar SED ( $\Delta(i-z)$ ). If there is no dust reddening in our population, we would expect the shape of these two distributions to be the same, whereas dust reddening would cause there to be (relatively) more red quasars on the blue end of the SED than the red end of the SED. Thus we can distinguish between dust reddening and synchrotron emission extending to the optical since dust preferentially absorbs the shorter-wavelength photons (e.g. adding a heavy red tail to  $\Delta(u-g)$ ), while synchrotron adds long-wavelength photons (e.g. adding a heavy red tail to  $\Delta(i-z)$ ). Figure 4.2 shows these two distributions and we can see  $\Delta(u-g)$  shows a heavier red “tail” than  $\Delta(i-z)$ , indicating that we do indeed have a population of dust reddened quasars.

#### 4.1.2 Red vs. Reddened: Photometry

As discussed in Richards et al. (2003), “red” quasars can be intrinsically red or dust reddened. In order to tell these two apart, we need to understand how dust changes the observed  $\Delta m$ . Combining Equation 1.17 with our definition of  $\Delta m$  and assuming the modal quasar contains no dust<sup>1</sup>:

$$\begin{aligned} \Delta m &= m - \langle m \rangle_{\text{mode},z} && \text{(observed)} \\ &= m_0 + 2.5\Delta(\alpha_\lambda) \log(\lambda) + E(B-V)R_\lambda && \text{(model)} \end{aligned} \quad (4.1)$$

<sup>1</sup>This technically measures dust reddening relative to the modal quasar and is in addition to any reddening of the modal quasar itself.

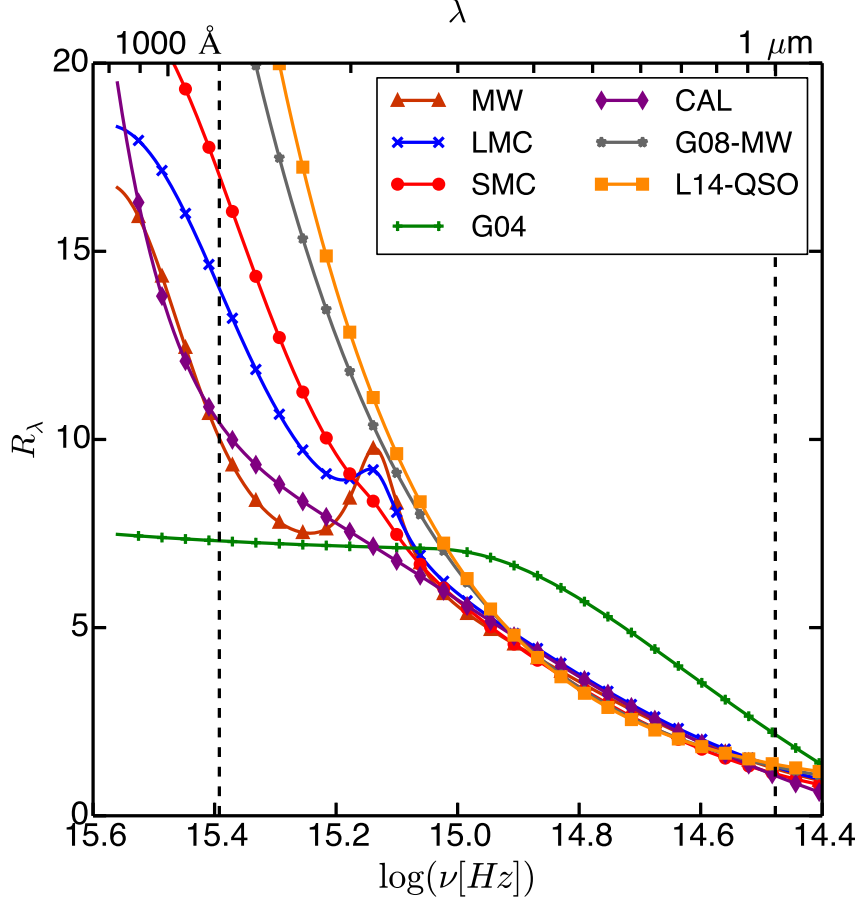


Figure 4.3 Extinction curves for seven different reddening laws with  $E(B - V) = 1$ : Milky Way type (brown triangles), LMC type (blue X's), SMC type (red dots), starburst type (purple diamonds), Goobar (2008) type (grey stars), Leighly et al. (2014) type (orange squares), and Gaskell et al. (2004) type (green +'s). The vertical dashed lines indicate the polynomial fitting range used in this chapter. In all cases we see dust reddening adds curvature to the relative magnitudes.

where  $m_0$  is a normalization term,  $\Delta(\alpha_\lambda)$  is the difference between the quasar's *intrinsic* spectral index and the *observed* modal spectral index of  $\alpha_\lambda = -1.72$  ( $\alpha_\nu = -0.28$ , as determined from the modal colors in Figure 4.1), with positive values being bluer, and  $R_\lambda$  is a function dependent on the properties of the dust. Throughout the remainder of the chapter we will be working with values of  $2.5\Delta(\alpha_\lambda)$  since that is the term that appears in the model. These values can be converted to absolute spectral indices ( $f_\lambda \propto \lambda^{\alpha_\lambda}$ ,  $f_\nu \propto \nu^{\alpha_\nu}$ ) by adding in the observed modal spectral index:

$$\alpha_\lambda = -1.72 - \Delta(\alpha_\lambda) \quad (4.2)$$

$$\begin{aligned} \alpha_\nu &= -2 - \alpha_\lambda \\ &= -0.28 + \Delta(\alpha_\lambda) \end{aligned} \quad (4.3)$$

As stated in §1.3, this model only holds between  $1\mu\text{m}$  and  $1216\text{\AA}$ , since that is where the

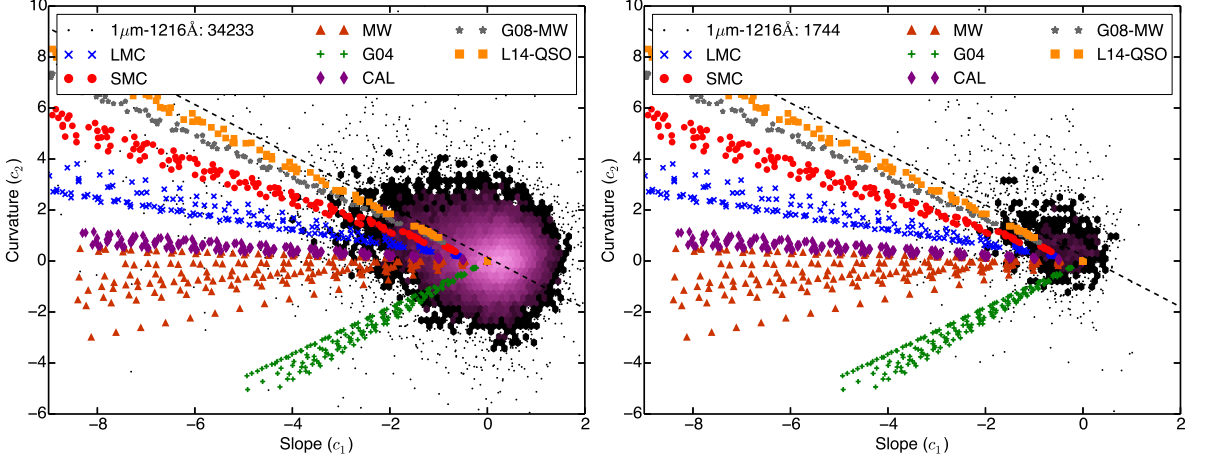


Figure 4.4  $c_1$  vs.  $c_2$  for uniformly selected SDSS quasars. The colors indicate the linear density of scatter points with white being the most dense and the outliers are shown as black scatter points. The symbols show a typical quasar placed at redshifts ranging from 0–2.2 and with  $E(B - V)$  values ranging from 0–0.8 for seven different reddening laws: SMC type (red dots), LMC type (blue X's), starburst type (purple diamonds), Milky Way type (brown triangles), multiple-scattering dust fit to the Milky Way (grey stars Goobar, 2008), multiple-scattering dust fit to a BAL quasar (orange squares Leighly et al., 2014), and Gaskell et al. (2004) type (green +'s). The black dashed line shows the orthogonal regression of the data. *Left:* Sample of 34,233 non-BAL quasars. *Right:* Sample of 1,744 BAL quasars. In both samples the trend of the data best matches the steeper reddening laws.

underlying SED is well approximated by a single powerlaw. The one thing  $R_\lambda$  has in common across all forms of dust is that it adds *curvature* to  $\Delta m$  by preferentially removing shorter wavelength photons (except for Gaskell et al. 2004 reddening which introduces curvature in the opposite sense). Figure 4.3 shows  $R_\lambda$  for seven different reddening laws with  $E(B - V) = 1$ : Milky Way (MW; Pei, 1992), Large Magellanic Cloud (LMC; Pei, 1992), Small Magellanic Cloud (SMC; Pei, 1992), starburst (CAL; Calzetti et al., 1995), multiple-scattering dust fit to the Milky Way (G08-MW; Goobar, 2008), multiple-scattering dust fit to a BAL quasar (L14-QSO; Leighly et al., 2014), and Gaskell et al. (G04; 2004) type reddening.

From Equation 4.1 we see that changes in the intrinsic spectral index ( $\Delta(\alpha_\lambda)$ ) will change the slope of  $\Delta m$  (i.e. it is only multiplied by  $\log(\lambda)$ ), while changes in the amount of dust ( $E(B - V)$ ) will change both the slope and curvature of  $\Delta m$  since  $R_\lambda$  contains higher orders of  $\log(\lambda)$ . Hopkins et al. (2004) characterized these changes by fitting  $\Delta m$  with a 1st-order Chebyshev polynomial to obtain the slope ( $c_1$ ), and fitting  $\Delta m$  with a 2nd-order Chebyshev polynomial to obtain the curvature ( $c_2$ ). Because of the orthogonality properties of the Chebyshev polynomials,  $c_1$  and  $c_2$  are linearly independent of each other. This property means that changes in a quasar's intrinsic spectral index will *only* change  $c_1$ , but given the nature of  $R_\lambda$ , changes in  $E(B - V)$  will change *both*  $c_1$  and  $c_2$ .

Figure 4.4 shows the  $c_1$  vs.  $c_2$  parameter space for both the non-BAL (*left*) and BAL (*right*) samples, where the symbols show the modal quasar ( $c_1=0$ ,  $c_2=0$  by definition) reddened by seven different reddening laws with redshifts ranging from 0–2.2 and  $E(B - V)$  values ranging from 0–0.8. If the reddening were instead applied to a quasar that was intrinsically blue (red) then the symbols

would shift to higher (lower)  $c_1$  values while the  $c_2$  values would remain unchanged. Looking at the trend of the BAL and non-BAL quasar samples in Figure 4.4, it appears that the data is most closely matched with the steeper reddening laws, e.g., the SMC dust law or the multiple-scattering dust model described by Goobar (2008) to explain anomalous dust extinction in supernovae host galaxies (see also Fynbo et al., 2013; Leighly et al., 2014).

#### 4.1.3 Monte Carlo Parameter Estimation

One of the difficulties of our analysis is the degeneracy between changes in color and dust reddening (e.g., Richards et al., 2003; Reichard et al., 2003a,b). As such, to fit for both the individual  $2.5\Delta(\alpha_\lambda)$  and  $E(B - V)$  values along with the shapes of the distributions they come from, we use a multi-level or hierarchical Bayesian model. In our model we assume the  $2.5\Delta(\alpha_\lambda)$  values come from a normal distribution with mean  $\mu_\alpha$  and width  $\sigma_\alpha$  and the  $E(B - V)$  values come from an exponentially modified Gaussian (EMG) distribution. The EMG is the result of summing a normal random variable with mean  $\mu_{\text{dust}}$  and width  $\sigma_{\text{dust}}$  and an exponential random variable with rate parameter  $\lambda_{\text{dust}}$  (smaller values indicate a heavier red tail). The EMG was chosen since it is very similar in shape to the half-normal, half-exponential distribution Hopkins et al. (2004) found to work well for the  $E(B - V)$  distribution of quasars. In addition to these parameters we also assume a noise term with zero mean and width  $S$  to model error in determining the modal colors. The technical details of this process are included in Appendix A for the interested reader; we summarize the results in §4.1.4 and continue our analysis in §4.2.

#### 4.1.4 MCMC Results: Population Parameters

Using the model described in §A.2, we fit for both individual  $2.5\Delta(\alpha_\lambda)$  and  $E(B - V)$  values ( $\phi_i = \{2.5\Delta(\alpha_\lambda)_i, E(B - V)_i\}$  from Appendix A) and the population parameters ( $\theta = \{\mu_\alpha, \sigma_\alpha, \mu_{\text{dust}}, \sigma_{\text{dust}}, \lambda_{\text{dust}}, S\}$  from Appendix A) describing the distributions of these variables. This method was used for both the SMC reddening law and the multiple-scattering reddening law from Goobar (2008) calibrated to fit Mark 231 (a BAL quasar; Leighly et al., 2014). The values of the population parameters for both reddening laws are given in Table 4.1 (see also the top and side panels of Figures 4.8 and 4.9). Figures 4.5 and 4.6 show the marginalized posterior distributions for the 1D and 2D projections for each of the six population parameters for the non-BAL and the BAL samples using the SMC reddening law<sup>2</sup>.

These projections reveal information about the overall shapes of our  $2.5\Delta(\alpha_\lambda)$  and  $E(B - V)$  distributions and correlations between the population parameters. Both samples have a positive value for  $\mu_\alpha$  indicating that the (intrinsic) mean spectral indices are bluer than the observed modal quasar. For the SMC law the BAL sample is bluer ( $\langle\alpha_\lambda\rangle = -1.83$ ) than the non-BAL sample ( $\langle\alpha_\lambda\rangle = -1.79$ ), and for the L14-QSO law the BAL sample is slightly redder ( $\langle\alpha_\lambda\rangle = -1.74$ ) than the non-BAL sample ( $\langle\alpha_\lambda\rangle = -1.76$ ). Although the values of  $\mu_\alpha$  are statistically different between the two samples, these differences are within  $1-2\sigma$  of our (systematic) ability to measure the modal spectral index (related to  $S$ ), indicating that the non-BAL and BAL quasars are consistent with having the same mean spectral index for both reddening laws.

---

<sup>2</sup>The results for the L14-QSO fit are qualitatively similar.

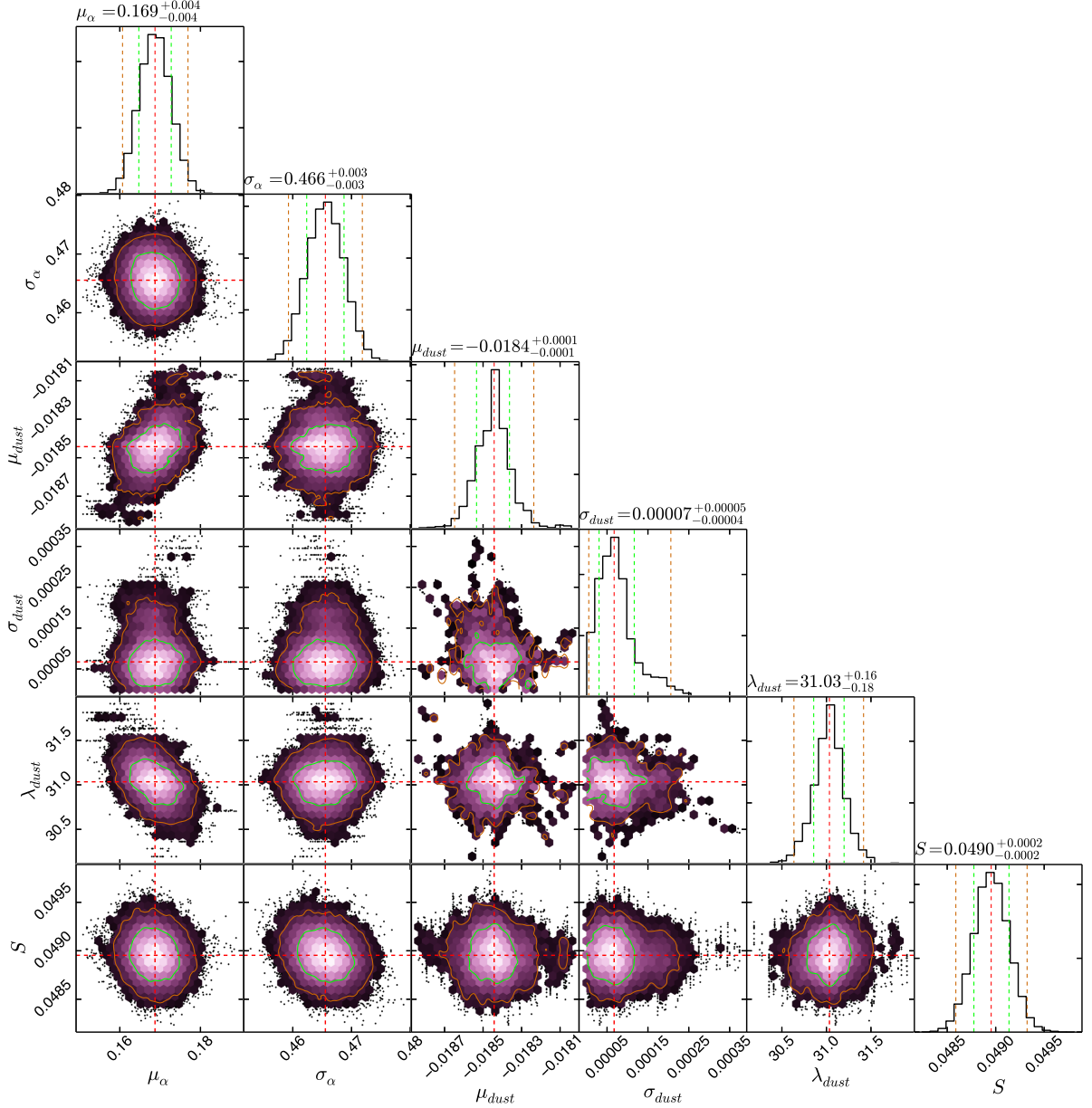


Figure 4.5 The best fit population parameters for an SMC reddening law for the non-BAL quasars. The red dashed lines show the median for each variable, the  $1\sigma$  ( $2\sigma$ ) confidence regions are shown in green (orange). The  $2.5\Delta(\alpha_\lambda)$  distribution is fit with a normal distribution with mean  $\mu_\alpha$  and width  $\sigma_\alpha$ . The  $E(B-V)$  distribution is fit with a EMG with shape parameters  $\mu_{dust}$ ,  $\sigma_{dust}$ , and  $\lambda_{dust}$  (see text).  $S$  is the uncertainty associated with determining the  $\Delta m$ . In the left column, third from the top, we see a positive correlation between the mean values of the  $2.5\Delta(\alpha_\lambda)$  and  $E(B-V)$  distributions, showing there is a degeneracy between these variables.

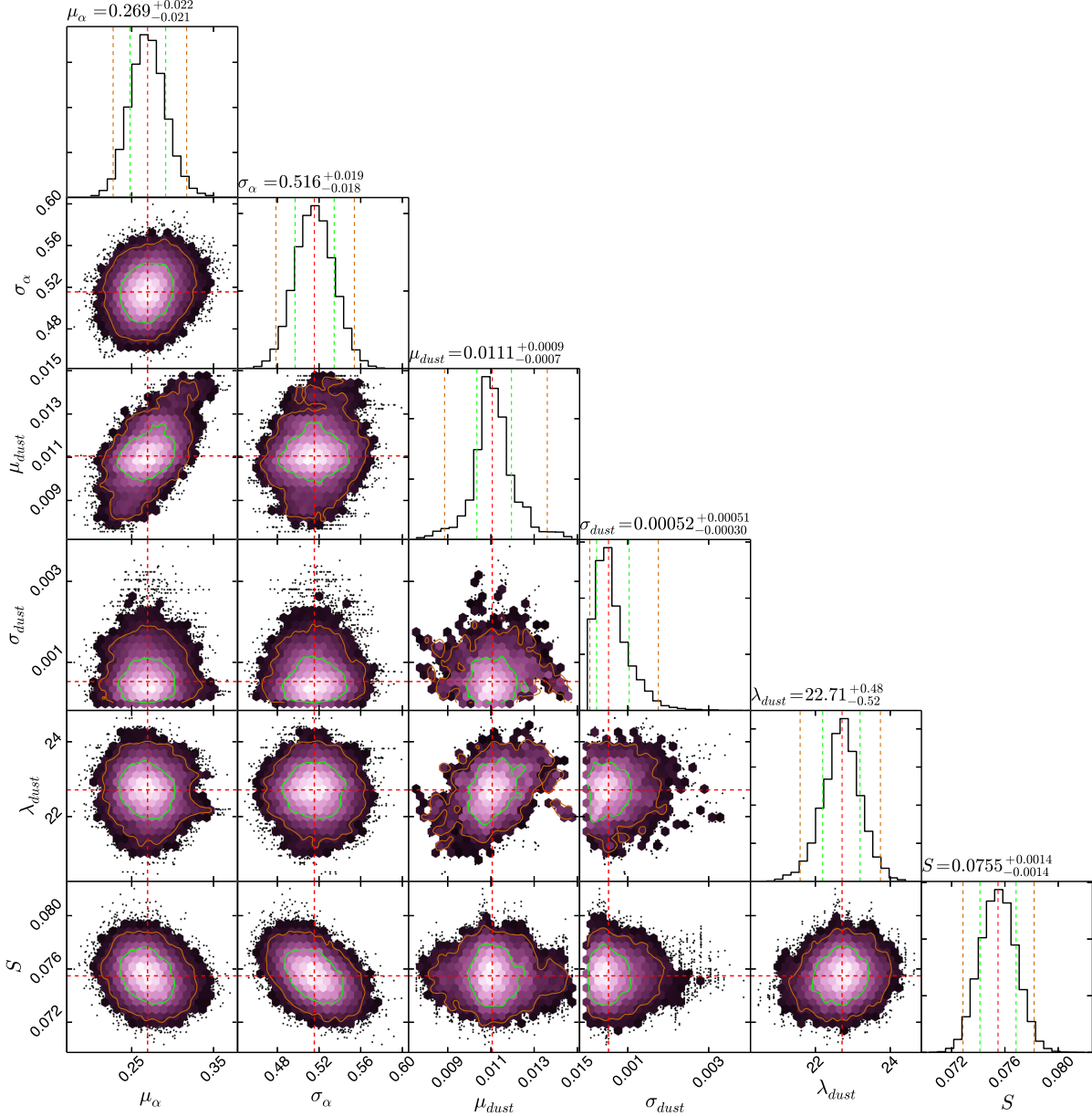


Figure 4.6 Same as Figure 4.5 but for the BAL quasars. As with the non-BAL sample we find a positive correlation between the mean values of the  $2.5\Delta(\alpha_\lambda)$  and  $E(B - V)$  distributions, showing there is a degeneracy between these variables. The BAL sample has a larger value for  $\mu_\alpha$  and a smaller value for  $\lambda_{dust}$  than the non-BAL sample, indicating that the BAL quasars, on average, are (statistically) intrinsically bluer and have more dust reddening than the non-BAL sample (see text).

Table 4.1. Hyperparameter Fit Values

Population Parameter	SMC		L14-QSO	
	non-BAL	BAL	non-BAL	BAL
$\mu_\alpha^a$	$0.169 \pm 0.004$	$0.269^{+0.022}_{-0.021}$	$0.098 \pm 0.004$	$0.052^{+0.019}_{-0.018}$
$\sigma_\alpha^a$	$0.466 \pm 0.003$	$0.516^{+0.019}_{-0.018}$	$0.505 \pm 0.003$	$0.535 \pm 0.015$
$\mu_{\text{dust}}$	$-0.0184 \pm 0.0001$	$0.0111^{+0.0009}_{-0.0007}$	$-0.0125 \pm 0.0001$	$0.0007^{+0.0004}_{-0.0003}$
$\sigma_{\text{dust}}$	$0.00007^{+0.00005}_{-0.00004}$	$0.00052^{+0.00051}_{-0.00030}$	$0.0004 \pm 0.0001$	$0.00027^{+0.00023}_{-0.0015}$
$\lambda_{\text{dust}}^b$	$31.03^{+0.16}_{-0.18}$	$22.71^{+0.48}_{-0.52}$	$53.96^{+0.31}_{-0.27}$	$41.53^{+0.89}_{-0.81}$
$S$	$0.0490 \pm 0.0002$	$0.0755 \pm 0.0014$	$0.0469 \pm 0.0002$	$0.0671 \pm 0.0012$

<sup>a</sup>These are the shape parameters for  $2.5\Delta(\alpha_\lambda)$  not  $\alpha_\lambda$ .

<sup>b</sup>Smaller values indicate a heavier tail.

Note. — The  $1\sigma$  error regions are given for each value.

In all cases  $\sigma_{\text{dust}}$  is consistent with 0; since this parameter corresponds to the width of the Gaussian half of the EMG distribution, this means the distribution for  $E(B - V)$  is consistent with coming from a pure exponential distribution that is offset from the origin by  $\mu_{\text{dust}}$ . We also find a positive correlation between  $\mu_\alpha$  and  $\mu_{\text{dust}}$  (left column, third from the top in Figures 4.5 & 4.6) showing there is a degeneracy between the mean values for  $\Delta(\alpha_\lambda)$  and  $E(B - V)$  in the model. The positive value of  $\mu_{\text{dust}}$  in the BAL sample suggests that all of the BAL quasars are consistent with having dust reddening, while the negative value on the non-BAL sample suggests that there are quasars with no dust reddening<sup>3</sup>.

Our population parameters for the SMC law are comparable to the shape parameters found in Table 2 of Hopkins et al. (2004). After converting the parameters to the same scale ( $\sigma_\alpha^{\text{Hopkins}} = \sigma_\alpha / 2.5$ ,  $\sigma_{\text{dust}}^{\text{Hopkins}} = 1/\lambda_{\text{dust}}$ , and  $\sigma_{\text{Gaussian}}^{\text{Hopkins}} = \sigma_{\text{dust}}$ ) we find  $\sigma_\alpha$  (0.33 in Hopkins) to be higher for the non-BAL (0.47) and BAL (0.52) samples and  $\lambda_{\text{dust}}$  (22.22 in Hopkins) to be about the same for the BAL sample (22.71) and higher<sup>4</sup> for the non-BAL sample (31.03). As mentioned above, our values for  $\sigma_{\text{dust}}$  are much smaller than the Hopkins et al. (2004) value of 0.02.

To see how well these population parameters represent our data we simulate an MC sample of quasars using the results of our fit to find  $c_1$  and  $c_2$  values. The resulting distributions can be seen in the left panels of Figure 4.7 while right panels show the residual with the original data. In the residual plots, green shows where the model over-estimated and purple shows where it under-estimated the number of objects. In Figure 4.7 we see that the model over-predicts the number of objects along the direction of largest deviation in  $c_1 - c_2$  space, whereas along the direction perpendicular (with the smallest deviation in  $c_1 - c_2$  space), the model under-predicts the number of objects. This difference shows that our model favors changes in the slope over changes curvature, and as a result under-estimates the amount of curvature in our data. This is not surprising given that the average object

<sup>3</sup>If the modal quasar has a small amount of dust reddening, negative  $E(B - V)$  values would indicate quasars with less dust than the mode.

<sup>4</sup>Higher values mean fewer reddened quasars

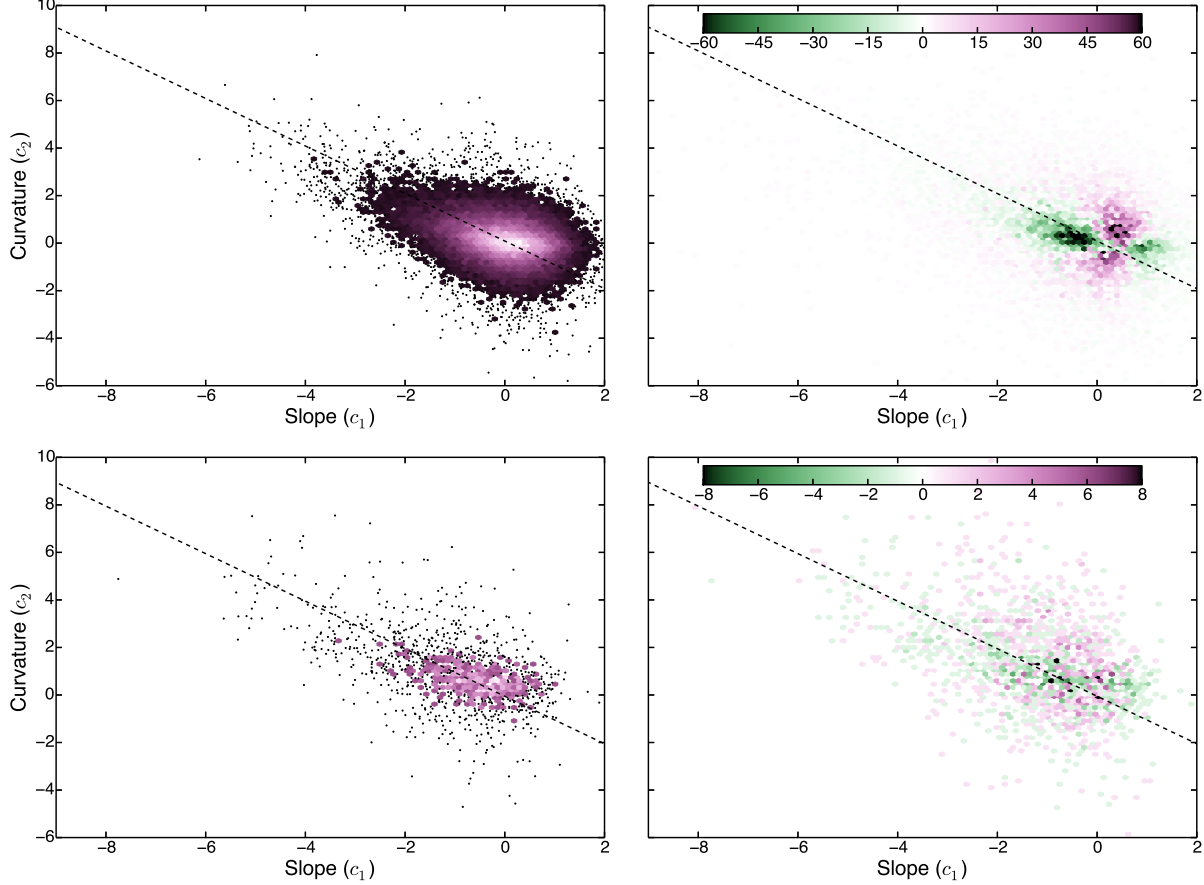


Figure 4.7 Monte Carlo simulations of  $c_1$  and  $c_2$  (*left*) and residuals with the data (*right*) for the SMC reddening law based on the population parameters shown in Figures 4.5 & 4.6 for the non-BAL (*top*) and BAL (*bottom*) samples. The orthogonal regression for the MC distributions are shown as a black dashed line in each panel. Our model over-predicts the number of quasars with low curvature, indicating it is likely under-predicting the amount of dust in the sample or the powerlaw model is not a perfect representation of the continuum.

has low curvature. This difference could also be attributed to the underlying SED not being well modeled by a powerlaw. In the bottom right panel of Figure 4.7 the agreement for the BAL sample is better, but again the amount of curvature is under-estimated by our model.

#### 4.1.5 MCMC Results: Individual Parameters

Previous studies (i.e., Reichard et al., 2003a,b) have avoided assigning physical meaning to their fit values for spectral index and amount of reddening due to the high degeneracy between these parameters (e.g., Figure 3 of Reichard et al., 2003a). The correlation between the  $\mu_\alpha$  and  $\mu_{\text{dust}}$  population parameters, and the correlations between the  $2.5\Delta(\alpha_\lambda)$  and  $E(B-V)$  values for an individual quasar, are very similar to the degeneracies seen in previous work. What makes our work different is the ability of our model to share this degeneracy across all levels of the model, from the individual fits up to the population parameters, in such a way that the degeneracy is broken in the

Table 4.2. Individual Fit Values

Name (J2000)	SMC			L14-QSO									
	2.5Δ(α <sub>λ</sub> )	E(B - V)	C <sub>α, α</sub>	C <sub>E(B-V), E(B-V)</sub>	C <sub>α, E(B-V)</sub>	DIC	2.5Δ(α <sub>λ</sub> )	E(B - V)	C <sub>α, α</sub>	C <sub>E(B-V), E(B-V)</sub>	C <sub>α, E(B-V)</sub>	DIC	BAL
104543.39+533203.0	-0.13 <sup>+0.42</sup> <sub>-0.39</sub>	0.021 <sup>+0.025</sup> <sub>-0.022</sub>	1.55 × 10 <sup>-1</sup>	5.04 × 10 <sup>-4</sup>	7.71 × 10 <sup>-3</sup>	-25.85	-0.22 <sup>+0.43</sup> <sub>-0.39</sub>	0.010 <sup>+0.013</sup> <sub>-0.012</sub>	1.55 × 10 <sup>-1</sup>	5.04 × 10 <sup>-4</sup>	7.71 × 10 <sup>-3</sup>	-21.47	0
102630.35+424632.0	0.29 <sup>+0.30</sup> <sub>-0.25</sub>	-0.007 <sup>+0.014</sup> <sub>-0.008</sub>	8.21 × 10 <sup>-2</sup>	1.32 × 10 <sup>-4</sup>	2.49 × 10 <sup>-3</sup>	-26.98	0.20 <sup>+0.32</sup> <sub>-0.27</sub>	-0.006 <sup>+0.008</sup> <sub>-0.005</sub>	8.21 × 10 <sup>-2</sup>	1.32 × 10 <sup>-4</sup>	2.49 × 10 <sup>-3</sup>	-18.34	0
105105.81+274934.4	-0.10 <sup>+0.41</sup> <sub>-0.39</sub>	0.087 <sup>+0.029</sup> <sub>-0.030</sub>	1.60 × 10 <sup>-1</sup>	8.92 × 10 <sup>-4</sup>	1.08 × 10 <sup>-2</sup>	-29.52	-0.26 <sup>+0.36</sup> <sub>-0.38</sub>	0.047 <sup>+0.017</sup> <sub>-0.017</sub>	1.60 × 10 <sup>-1</sup>	8.92 × 10 <sup>-4</sup>	1.08 × 10 <sup>-2</sup>	-12.32	0
120540.29+384636.9	0.52 <sup>+0.32</sup> <sub>-0.21</sub>	-0.007 <sup>+0.017</sup> <sub>-0.008</sub>	5.05 × 10 <sup>-2</sup>	2.00 × 10 <sup>-4</sup>	1.77 × 10 <sup>-3</sup>	-31.00	0.51 <sup>+0.31</sup> <sub>-0.21</sub>	-0.006 <sup>+0.010</sup> <sub>-0.005</sub>	5.05 × 10 <sup>-2</sup>	2.00 × 10 <sup>-4</sup>	1.77 × 10 <sup>-3</sup>	-13.69	0
154117.05+100910.9	0.62 <sup>+0.24</sup> <sub>-0.21</sub>	0.003 <sup>+0.017</sup> <sub>-0.014</sub>	4.91 × 10 <sup>-2</sup>	2.18 × 10 <sup>-4</sup>	2.85 × 10 <sup>-3</sup>	-33.60	0.65 <sup>+0.20</sup> <sub>-0.20</sub>	0.003 <sup>+0.008</sup> <sub>-0.008</sub>	4.91 × 10 <sup>-2</sup>	2.18 × 10 <sup>-4</sup>	2.85 × 10 <sup>-3</sup>	-21.24	0
205201.61+000051.5	-0.19 <sup>+0.37</sup> <sub>-0.29</sub>	0.014 <sup>+0.031</sup> <sub>-0.022</sub>	1.10 × 10 <sup>-1</sup>	6.69 × 10 <sup>-4</sup>	7.25 × 10 <sup>-3</sup>	-29.99	-0.27 <sup>+0.34</sup> <sub>-0.27</sub>	0.005 <sup>+0.018</sup> <sub>-0.012</sub>	1.10 × 10 <sup>-1</sup>	6.69 × 10 <sup>-4</sup>	7.25 × 10 <sup>-3</sup>	-4.98	0
083857.43+275701.9	0.05 <sup>+0.26</sup> <sub>-0.19</sub>	-0.004 <sup>+0.015</sup> <sub>-0.010</sub>	5.73 × 10 <sup>-2</sup>	1.65 × 10 <sup>-4</sup>	2.55 × 10 <sup>-3</sup>	-34.52	-0.01 <sup>+0.26</sup> <sub>-0.20</sub>	-0.005 <sup>+0.009</sup> <sub>-0.006</sub>	5.73 × 10 <sup>-2</sup>	1.65 × 10 <sup>-4</sup>	2.55 × 10 <sup>-3</sup>	-25.02	0

Note. — This table is available in its entirety in a machine-readable form in the electronic version of this journal. A portion is shown here for guidance regarding its form and content.

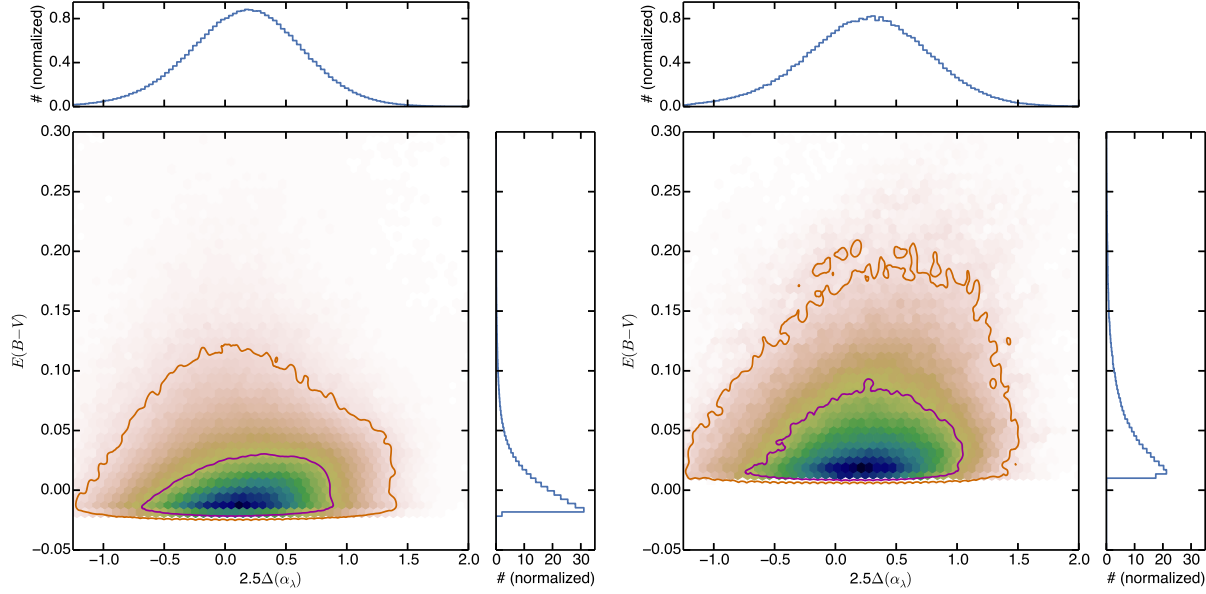


Figure 4.8 Joint probability distribution of  $2.5\Delta(\alpha_\lambda)$  and  $E(B - V)$  values for non-BAL (left) and BAL (right) quasars for the SMC reddening law. The  $1\sigma$  ( $2\sigma$ ) contours are shown in purple (orange) and the fully marginalized distributions for each variable are shown as histograms. The zero point on the x-axis represents the modal quasar that has  $\alpha_\lambda = -1.72$  ( $\alpha_\nu = -0.28$ ) and positive  $2.5\Delta(\alpha_\lambda)$  values are bluer. The negative  $E(B - V)$  values on the left argue that the mean non-BAL quasar is not dust reddened (and is slightly bluer than we have assumed). The positive  $E(B - V)$  values on the right argue that, in contrast to non-BALs, BALs all have dust and are intrinsically bluer than the non-BALs by virtue of the centroid of the blue region. Moreover, at a given  $E(B - V)$ , the most probable value for  $2.5\Delta(\alpha_\lambda)$  is larger, suggesting that more heavily reddened BAL quasars are actually intrinsically bluer.

marginalized distribution, as can be seen in Figures 4.8 and 4.9. Put another way, the individual fits are regulated by the population parameters, kept within physical ranges by priors, and uncertainty is propagated through every level such that the marginalized distributions for  $2.5\Delta(\alpha_\lambda)$  and  $E(B - V)$  follow the model we specified in §A.2. As a result the trends seen in Figures 4.8 and 4.9 are expected to be real trends in the data and are not caused by degeneracies in the model. Table 4.2 provides the  $\alpha_\lambda$ ,  $E(B - V)$ , and the covariance matrix between them for each quasar and both reddening laws.

Figures 4.8 and 4.9 show the marginalized joint probability distributions for  $2.5\Delta(\alpha_\lambda)$  and  $E(B - V)$  for each of our samples, i.e. the (2D) probability distribution for each *individual* quasar summed together and projected onto the  $2.5\Delta(\alpha_\lambda)$ - $E(B - V)$  plane. The top and side panels of each plot show the fully marginalized probability distributions for  $2.5\Delta(\alpha_\lambda)$  and  $E(B - V)$  respectively; these distributions are the ones described by the population parameters in Table 4.1. The modal quasar ( $\alpha_\lambda = -1.72$ ,  $\alpha_\nu = -0.28$ ) represents the zero point of the x-axis and positive values of  $\Delta(\alpha_\lambda)$  indicate quasars that are bluer than the mode.

In Figure 4.8 we show the results for fitting the SMC reddening law. As was learned from the population parameters, we see that both the non-BAL and BAL samples are (on average) bluer than the modal quasar and the BAL sample shows more dust reddening. The marginalized

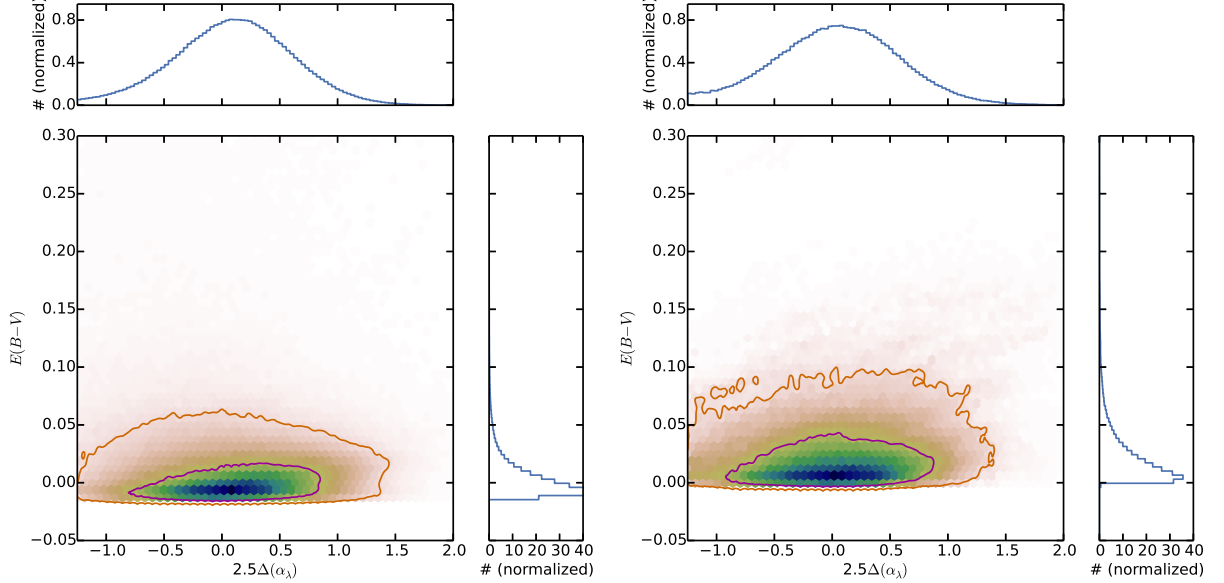


Figure 4.9 Same as Figure 4.8 but using the L14-QSO reddening law. The general shapes of these distributions are the same but the  $E(B - V)$  values are smaller, as expected for a steeper reddening law. Again, the BAL quasars show that for a given  $E(B - V)$ , the most probable value for  $2.5\Delta(\alpha_\lambda)$  is larger, suggesting that the more heavily reddened BAL quasars are actually intrinsically bluer.

distributions for  $E(B - V)$  argue that 2.5% (13%) of the non-BAL (BAL) quasars are consistent with  $E(B - V) > 0.1$  and 0.1% (1.3%) are consistent with  $E(B - V) > 0.2$ . Moreover, at a given  $E(B - V)$  value, the BAL quasars are more likely to be bluer, suggesting that more heavily reddened BAL quasars are actually intrinsically bluer. This trend is not seen in the non-BAL sample. In both plots we see a lack of quasars that are intrinsically red and heavily dust reddened. This deficit could be caused by an observational bias, i.e. quasars in this region have colors that are missed by the selection algorithm. If this is not the case, then this implies that the heaviest levels of extinction are associated with the quasar itself rather than the host galaxy, otherwise there would be no link between the intrinsic color and the reddening.

In Figure 4.9 we see qualitatively the same trends for the L14-QSO reddening law as we did for the SMC law, the biggest differences being the scaling of the y-axis and a shift in the  $\Delta(\alpha_\lambda)$  to smaller values. Here the marginalized distributions for  $E(B - V)$  argue that 0.2% (1.7%) of the non-BAL (BAL) quasars are consistent with  $E(B - V) > 0.1$  and 0.002% (0.022%) are consistent with  $E(B - V) > 0.2$ .

Using this data set, we can also look at the BAL fraction as a function of  $2.5\Delta(\alpha_\lambda)$  and  $E(B - V)$ . Figure 4.10 shows that the BAL fraction for the SMC and L14-QSO reddening laws. As with the previous plots, we see that the BAL fraction is qualitatively similar for both reddening laws: it increases from  $\sim 0.01$  for red quasars with little dust reddening, up to  $\sim 0.6$  for blue quasars with heavy dust reddening. After marginalizing over  $E(B - V)$  we see that the BAL fraction ranges between  $\sim 0.05$  and  $\sim 0.2$  and it clearly increases as quasars become bluer. This trend has only become clear due to our larger data set, and is in comparison to previous studies (e.g. Tolea

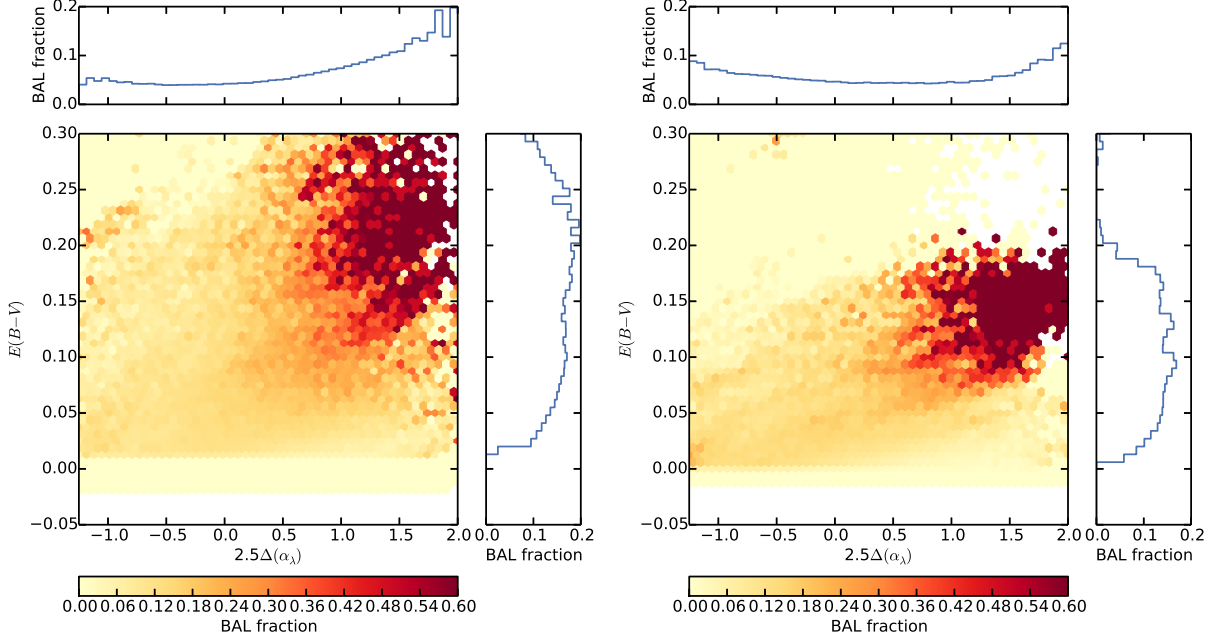


Figure 4.10 The fraction of BAL quasars as a function of  $2.5\Delta(\alpha_\lambda)$  and  $E(B - V)$  for the SMC reddening law (*left*) and the L14-QSO reddening law (*right*). The fully marginalized BAL fractions are shown in the histograms. We can see the BAL fraction goes from  $\sim 0.01$  to  $\sim 0.6$  as the intrinsic color becomes bluer and the amount of dust increases. Although the BAL fraction reaches  $\sim 0.6$  in the 2D parameters space, it does not exceed  $\sim 0.2$  after marginalizing over  $E(B - V)$ .

et al., 2002; Hewett & Foltz, 2003; Reichard et al., 2003b) that were only able to measure the mean BAL fraction of  $\sim 20\%$ . As with Figures 4.8 and 4.9 we have marginalized over the probability distributions for each individual quasar, meaning the trend seen here is expected to be real (up to any observational biases) and not an artifact of our model.

This analysis suggests that the parent populations for BALs and non-BALs are slightly different (BALs being intrinsically bluer, on average). However, we need to be careful that selection effects are not involved. For example, Reichard et al. (2003b) discussed how the probability of SDSS finding a BAL changes with redshift.

#### 4.1.6 What Reddening Law Fits Better?

Given that we used two different reddening laws to fit our data, it is natural to ask: what reddening laws fits the data better? To answer this question we use the deviance information criterion (DIC). The DIC is a generalization of the Bayesian information criterion (BIC) such that it can be directly applied to the output of an MCMC fit, and can be used to directly compare multiple models fit to the same data. The DIC is made up to two terms, one that is related to the likelihood of the model explaining the data (similar to  $\chi^2$ ), and a penalty term based on the complexity of the model (i.e. the effective degrees of freedom after taking into account the covariances between the fitted variables).

Table 4.3. Reddening Law Comparison

Evidence	non-BAL		BAL	
	Number	Fraction	Number	Fraction
SMC: strong	23443	68.5%	1131	64.9%
SMC: positive	9291	27.1%	414	23.7%
Both	1470	4.3%	192	11.0%
L14-QSO: positive	16	0.05%	5	0.3%
L14-QSO: strong	6	0.01%	2	0.1%

Models that have smaller DIC values fit the data better than models with higher DIC value, and the size of this difference gives a measure of how much better the fit is. When the difference is less than 2 both models fit the data well, when it is between 2 and 6 there is positive evidence for the lower model fitting better, and when it is greater than 6 there is strong evidence. We have calculated the DIC for each individual quasar to see what model fits better, these values are included in Table 4.2. Table 4.3 summarizes the comparison of the two models. Overall we find the SMC reddening law does a better job fitting our data, and to the end of applying the best correction in the mean sense, it will be used exclusively for the remainder of this thesis. However, we do find that up to 4% (11%) of non-BAL (BAL) quasars show signs of contributions from multiple scattering, and for future work it may be interesting to consider this subset to see how they differ from the main sample.

## 4.2 Composite Spectra

Hopkins et al. (2004) discuss composite spectra as functions of the  $(c_1, c_2)$  parameter space. Here we construct composite spectra based on the more physical parameter space of  $2.5\Delta(\alpha_\lambda)$  and  $E(B - V)$  from the previous section. Our composites are constructed in the same way as the Vanden Berk et al. (2001) quasar composite, using similar code. In brief, the quasars are sorted by redshift, shifted to their rest frames, re-sampled onto a common 1Å grid, and normalized by the overlap with the current composite. To preserve the continuum shape in the composite we chose to use a weighted geometric mean to combine the spectra (Vanden Berk et al., 2001; Reichard et al., 2003b).

The spectra were split into ten equally spaced bins in both  $2.5\Delta(\alpha_\lambda)$  and  $E(B - V)$ . The MCMC sampler from §4.1.3 produced full probability distributions for each quasar in this parameter space, allowing us to find the probability for each quasar belonging to any given bin. This probability was used as the weight when calculating the geometric mean in each bin. To prevent quasars with high variance (i.e. spread across many bins) from contaminating the sample, only quasars with a probability of being in a bin greater than 10% were used. After this cut, composites were made for any bin with more than ten quasars.

### 4.2.1 Red vs. Reddened: Spectra

Figures 4.11 and 4.12 show the resulting composites for the non-BAL and BAL samples respectively. Each panel in these figures corresponds to a single  $2.5\Delta(\alpha_\lambda)$  bin (the 10th bin for each sample had too few quasars to stack) and each color corresponds to a single  $E(B - V)$  bin. The black dashed lines show the typical intrinsic powerlaw in each bin (red to blue going from the top left to bottom right) with the red dashed lines showing the global modal powerlaw,  $\alpha_\lambda = -1.72$  ( $\alpha_\nu = -0.28$ ), for comparison. The color dashed lines show the typical powerlaw for each bin reddened by the  $E(B - V)$  values corresponding to each color. In most cases we see that the color dashed lines are in agreement with the stacked spectra in each bin, indicating that the  $2.5\Delta(\alpha_\lambda)$  and  $E(B - V)$  values found in the previous section are accurate. The notable exceptions are the most reddened bin for almost all the  $2.5\Delta(\alpha_\lambda)$  bins, these spectra tend to show more curvature than would be expected from the fits to their photometry suggesting, that, if anything, those quasars are better fit by a steeper reddening law (such as multiple-scattering).

We also see slight deviations in the bluest bin for the least reddened spectra. One potential cause for this deviation is if the underlying continuum between  $1\mu\text{m}$  and  $1216\text{\AA}$  is not well described by a powerlaw. The continuum emission from a quasar is thought to come from a modified blackbody (Shakura & Sunyaev, 1976) that has been seen to turn over at wavelengths of about  $\sim 1000\text{--}1300\text{\AA}$  (Shang et al., 2005). If this turn over happens within the fitting range of our model, these quasars will be erroneously fit with large  $E(B - V)$  values and have curvatures that are different than that caused by an SMC law.

For the BAL quasars in Figure 4.12 we see a trend in C IV absorption ( $\log(\lambda) \sim 3.2$ ) with  $2.5\Delta(\alpha_\lambda)$  and  $E(B - V)$ . At a given  $2.5\Delta(\alpha_\lambda)$  value the absorption trough for C IV deepens as  $E(B - V)$  increases. When holding  $E(B - V)$  at a fixed value, the absorption trough becomes wider (and extends to higher velocities) for bluer colors than redder colors. These trends are consistent with the findings of Baskin et al. (2013) who found C IV troughs become wider as the strength of He II decreased, a trend we find also corresponds to the non-BAL quasars being bluer (see §4.2.2). They also found the depth of the C IV trough increased as  $\alpha_{UV1}$  became redder, a quantity they associated with dust reddening.

### 4.2.2 Individual Lines

Richards et al. (2003) constructed several composite spectra based on the observed  $\Delta(g - i)$  relative colors. They were able to construct four spectra that had little dust reddening and span different spectral indices. By comparing these spectra they found several trends in individual spectral lines related to the intrinsic slopes. Our analysis provides a more robust metric for distinguish intrinsically red and dust reddened quasars, allowing us to create a cleaner sample of quasars that are thought to be relatively free of dust.

In this section we explore the trends in some individual emission lines as a function of the intrinsic spectral index for the non-BAL quasars consistent with little to no reddening (i.e. the lowest  $E(B - V)$  bin). To prevent being influenced by known trends due to quasar luminosity, we picked sub-samples from each bin such that the distribution of  $L_{2500\text{\AA}}$ , taken from Krawczyk et al. (2013), was the same for every sample. When doing this we excluded the two bluest bins from

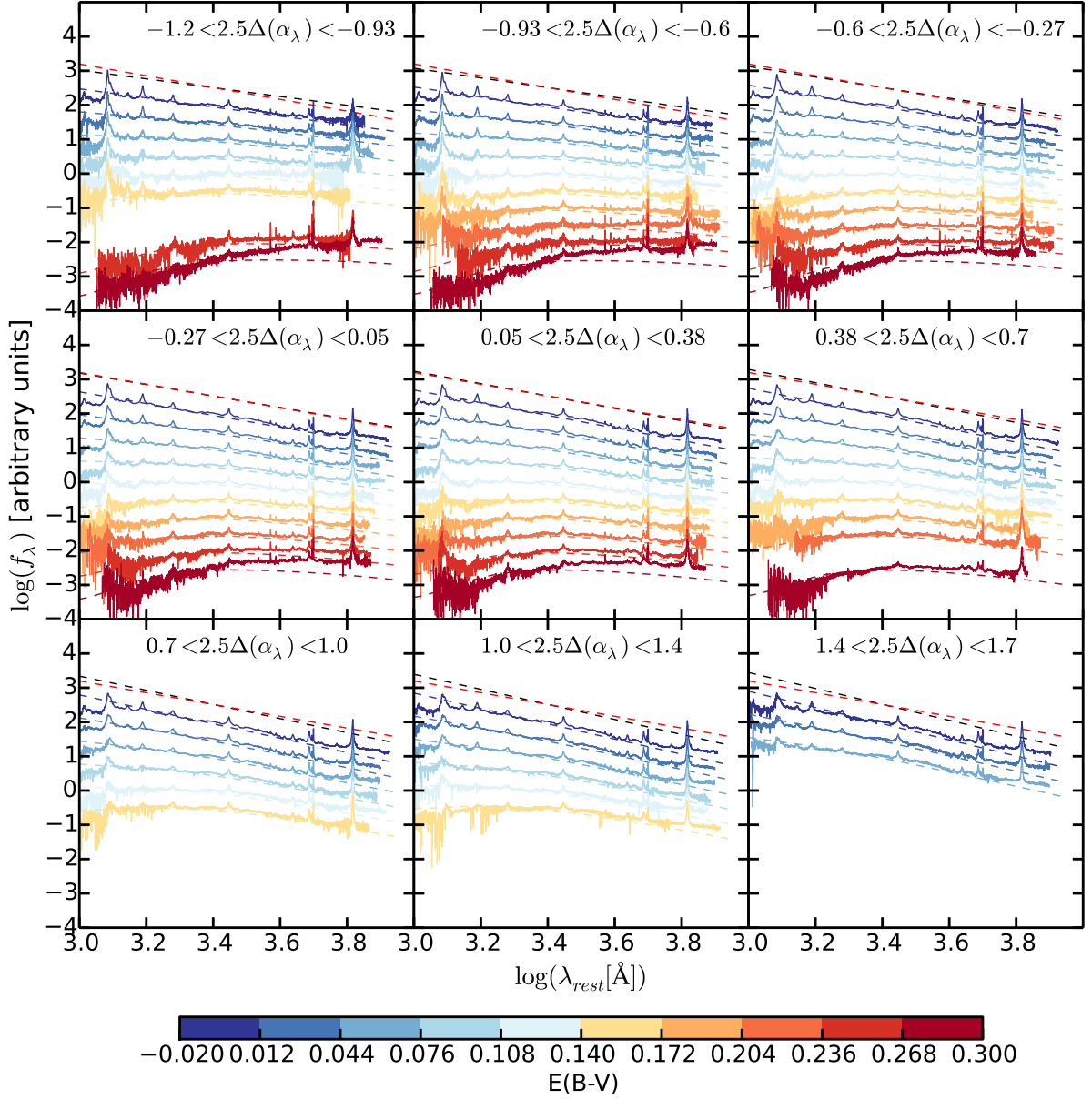


Figure 4.11 Composite spectra for non-BAL quasars (solid lines) for nine evenly spaced bins along  $2.5\Delta(\alpha_\lambda)$  (subplots going intrinsically red to blue from the top left to the bottom right) and for ten evenly spaced bins along  $E(B - V)$  (various colors) based on the fits to the SMC reddening law. The black dashed line in each panel indicates the typical powerlaw for each quasar in that  $2.5\Delta(\alpha_\lambda)$  bin and the red dashed line shows the observed modal powerlaw ( $\Delta(\alpha_\lambda) = 0$ ) for comparison. The colored dashed lines show the typical powerlaw reddened by the  $E(B - V)$  value corresponding to each color. The middle-left panel shows objects with spectral indices most similar to the modal powerlaw. The objects best fit by an intrinsically bluer spectrum demonstrate that such objects exist, but the bluest spectra that are best fit without any dust are not perfect fits. This could be a sign of mis-fitting, or may be an indication of the spectral turn-over within the fitting region (which is expected from Shang et al. (2005)). Each composite spectrum is largely in agreement with the bin values found from fitting the photometry.

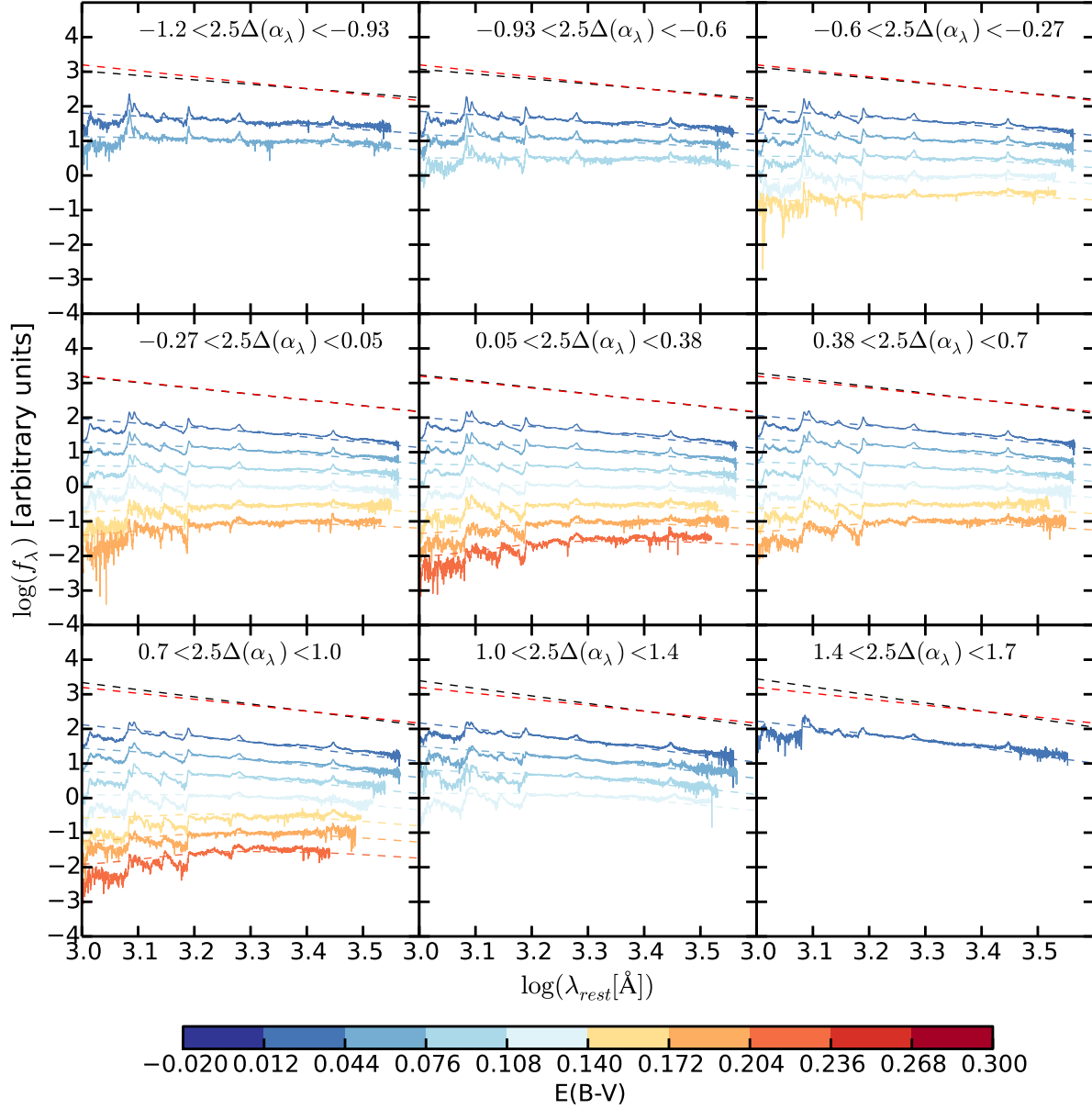


Figure 4.12 Same as Figure 4.11 but for the BAL sample. Within each panel there is an increase in the depth of the C IV absorption trough ( $\log(\lambda) \sim 3.2$ ) as the  $E(B-V)$  values increase. The C IV absorption trough also becomes wider as quasars become bluer (e.g. the trough extends out to the nearby Si IV line for the bluest quasars). Each composite spectra is largely in agreement with the bin values found from fitting the photometry.

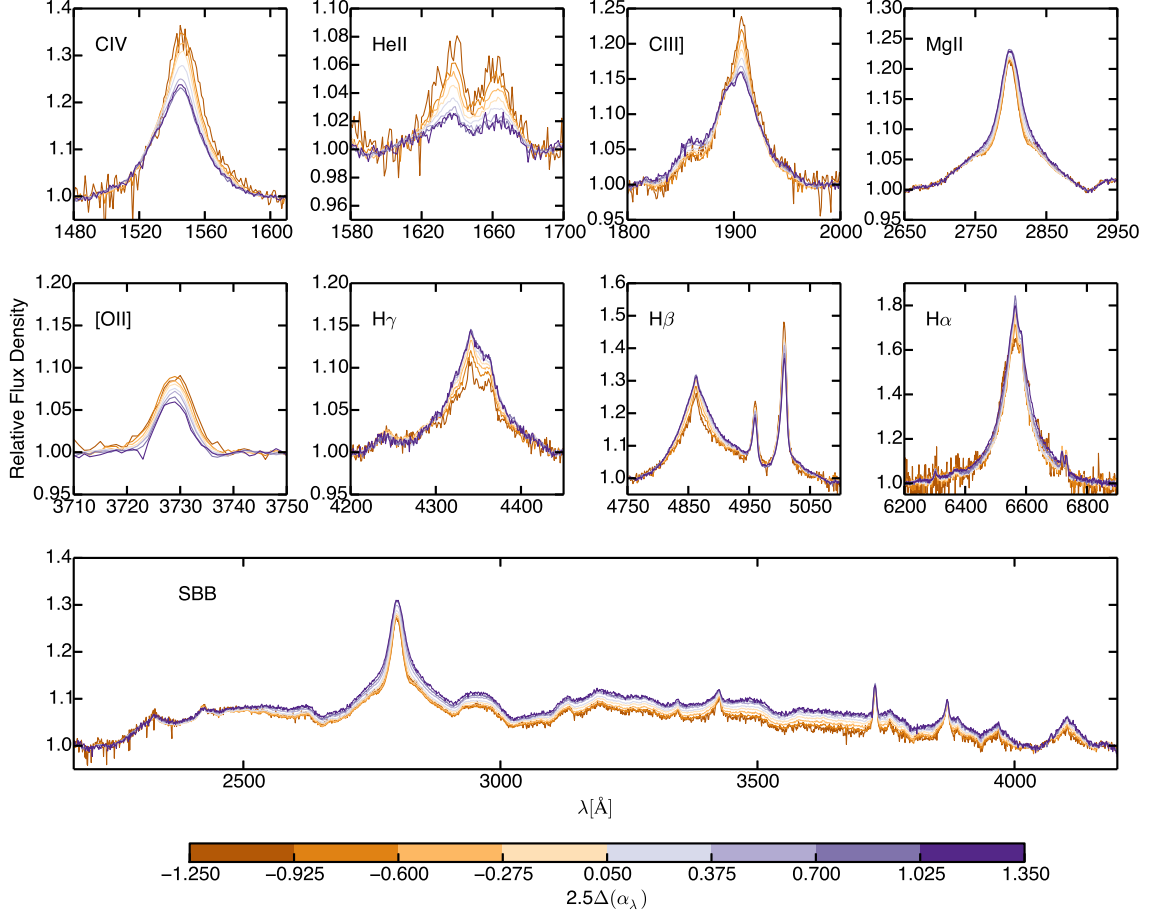


Figure 4.13 Expanded emission-line regions from the lowest  $E(B-V)$  bin from Figure 4.11 ( $E(B-V) < 0.012$ ). “SBB” refers to the 3000 Å (or small blue) bump. The colors represent the  $2.5\Delta(\alpha_\lambda)$  value for each spectrum. The spectra are normalized such that their continua agree at the edges of the panels.

the analysis seeing as their  $L_{2500\text{ \AA}}$  distributions were significantly lower than the other bins<sup>5</sup>. The resulting luminosity distribution for the non-BAL sample had  $44.4 < \log(L_{2500\text{ \AA}} [\text{ergs s}^{-1}]) < 47$  and a median of 45.7, while the BAL sample had  $46 < \log(L_{2500\text{ \AA}} [\text{ergs s}^{-1}]) < 46.7$  and a median of 46.2.

The major emission line regions are shown in Figure 4.13. These spectra have been normalized such that they are unity at the edges of each plot. Below we comment on each of the emission lines.

**C IV** – Unlike Richards et al. (2003), who found only slight trends in C IV, we see a very clear trend with C IV where redder quasars have stronger emission. We attribute this difference between our work and that of Richards et al. (2003) as being due to our better ability to separate dust from intrinsic redness (specifically dusty blue objects likely affected the reddest spectra in Richards et al. (2003)) which is consistent with bluer objects having weaker C IV. There is also a small blueward

<sup>5</sup>This lower  $L_{2500\text{ \AA}}$  distribution is caused by lower redshift distribution for the bluest quasars (see Figure 5.4).

shift of the line for objects with weaker C IV, consistent with previous findings (e.g. Sulentic et al., 2007; Richards et al., 2011; Gaskell & Goosmann, 2013), best seen here in the red wing of the line (as compared to the blue wing).

**He II** – The strength of the He II  $\lambda 1640 \text{ \AA}$  increases as the spectra become redder. The same trend can be seen in the O III]/Al II/Fe II blend just redward of He II. Leighly & Moore (2004) suggests that a stronger He II emission line is an indicator of a harder (bluer) continuum in the X-ray. These trends are consistent with Richards et al. (2003).

**C III]** – A clear trend of increasing strength with increasing redness is seen in the C III]  $\lambda 1909 \text{ \AA}$  line, consistent with Richards et al. (2003). The opposite trend is seen in the nearby Al III  $\lambda 1857 \text{ \AA}$  line (blue being stronger) and no trend is seen in the Si III]  $\lambda 1892 \text{ \AA}$  line, whereas Richards et al. (2003) showed no trend with either line. The combination of both strong Al III and Si III] with respect to C III] in the bluer quasars is an indication that they have a softer (redder) ionizing spectrum as compared to the redder quasars (Appendix A3 of Casebeer et al., 2006).

**Mg II** – There is a slight trend in Mg II where the line get weaker and narrower as redness increases.

**[O II]** – This line shows the opposite trend as Mg II, the line get stronger and wider as redness increases, broadly consistent with Richards et al. (2003). The combination of stronger [O II] and weak Balmer line emission in the red quasars may indicate an underestimation in the host galaxy subtraction for these quasars.

**H $\gamma$  and [O III]** – The strengths of both H $\gamma$  and [O III]  $\lambda 4363 \text{ \AA}$  decrease as redness increases.

**H $\beta$**  – The strength and width of the H $\beta$  decreases as redness increases. The width of this line has been shown to be an indicator of inclination, such that wider H $\beta$  corresponds to more edge-on views of the accretion disk (Wills & Browne, 1986). Additionally the FWHM of H $\beta$  is used to estimate the virial velocity of the BLR when estimating black hole masses (Vestergaard & Peterson, 2006, e.g.), where a larger FWHM corresponds to a more massive black hole. The nearby [O III] lines show a slight trend in the opposite direction, an indication that the electron temperature of the emitting gas could be changing in response to the quasars continuum.

**H $\alpha$  and [N II]** – As with the other Balmer lines, H $\alpha$  gets weaker as redness increases.

**SBB** – The small blue bump (SBB) becomes smaller as redness increases, consistent with Richards et al. (2003). This is likely caused by a weakening of the Balmer emission as quasars become redder.

We also looked at the same spectral lines while holding  $2.5\Delta(\alpha_\lambda)$  fixed and comparing spectra with different value of E(B – V). The clearest trend is seen in C IV, where the strength of the line decreases as the reddening increases. Unlike Richards et al. (2003) we do not see any increase in the strength of [O II] with reddening, but we do see a slight increase in the [O III] lines. The strong increase in [O II] seen in Richards et al. (2003) could have been caused by intrinsically red quasars being mistaken as dust reddened in their sample.

In the BAL spectra we confirm differences in the emission and (mean) absorption as a function of (intrinsic) color (see Figure 4.14), with the redder objects having more strongly peaked C IV, stronger C III (and Si III) and some excess at  $\sim 1750 \text{ \AA}$ , as was seen in Figure 9 of Reichard et al. (2003b). The absorption and emission are correlated as might be expected if both are responding to differences in the SED. If the absorption was not responding to differences in the SED, the differences in the absorption troughs would be averaged away and little variation would be seen in

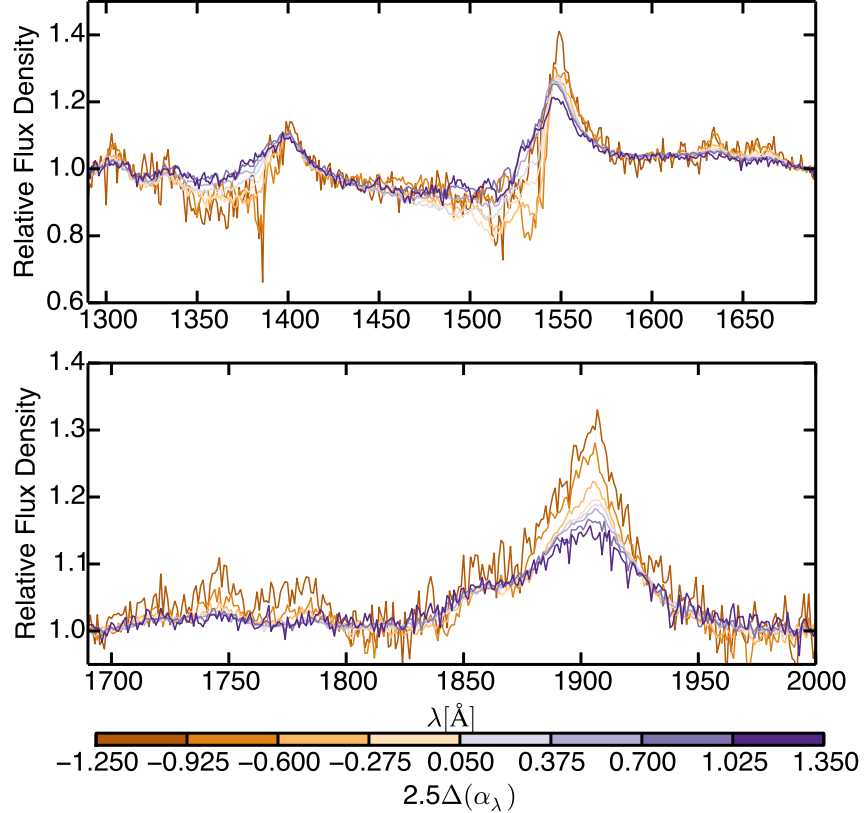


Figure 4.14 Expanded emission-line regions from the lowest  $E(B - V)$  bin from Figure 4.12 ( $0.012 < E(B - V) < 0.044$ ). The colors represent the  $2.5\Delta(\alpha_\lambda)$  value for each spectrum. The spectra are normalized such that their continua agree at the edges of the panels. Intrinsically redder BALs have stronger C IV and C III] emission lines. The correlation seen between changes in both the emission and absorption lines indicate they are both responding to changes in the underlying SED.

the composites. Therefore, the correlation we see indicates there may be some underlying trend relating both the absorption and emission (e.g., Turnshek et al., 1988). The narrow, low-velocity absorption seen in the redder BAL quasars (just blueward of the C IV and Si IV lines) could be an indication of weaker wind. These quasars also show evidence of strong, not blueshifted C IV and strong C III] two properties that Richards et al. (2011) argue are also indicators of a weaker winds.

We note that the radio-loud (RL) “BALs” Becker et al. (e.g., 2000) do not always meet the formal definition of BALs, having relatively weak absorption troughs at low velocity. As the RL quasars tend to be (on average) redder than radio-quiet (RQ) quasars, our finding of mini-BAL-like residuals in the reddest composites is not that surprising.

### 4.3 Conclusions

Using mid-IR thorough UV photometry alone we calculated intrinsic powerlaw slopes ( $2.5\Delta(\alpha_\lambda)$ ) and SMC reddening law coefficients ( $E(B - V)$ ) for  $\sim 35,000$  uniformly selected quasars from the SDSS DR7 quasar catalog. By using a hierarchical Bayesian model we were able to break the

degeneracy between these parameters and keep both of them in a physical range (Figure 4.8). From these fits we found that BAL quasars are biased (blueward) within the parent population as compared to the non-BAL quasars. The BAL quasars are slightly bluer ( $\alpha_\lambda = -1.83$ ) and have higher amounts of reddening (13% with  $E(B - V) > 0.1$ ) than the non-BAL quasars ( $\alpha_\lambda = -1.79$ , 2.5% with  $E(B - V) > 0.1$ ). We also find the BAL fraction is very dependent on the intrinsic color and amount of dust reddening of the quasars. After marginalizing over  $E(B - V)$  we find the BAL fraction increases from  $\sim 0.05$  to  $\sim 0.2$  as quasars become bluer (Figure 4.10).

We constructed composite spectra by splitting the resulting measurements of  $2.5\Delta(\alpha_\lambda)$  and  $E(B - V)$  into a 10x10 grid. With the exception of the non-BAL quasars with the most reddening and the bluest quasars with the least reddening, the fit values for each bin do a good job of reproducing the slopes and curvatures of the spectra, showing that our fit values are physically meaningful (Figures 4.11 and 4.12). Exploring the spectra further, we found within the BAL sample that the C IV absorption trough becomes deeper as  $E(B - V)$  increases and becomes wider as quasars become bluer.

Comparing the spectra in the lowest reddening bin revealed trends in the spectral lines based on a quasar's intrinsic color. We found that intrinsically red quasars have stronger C IV, He II, C III], and [O II], while the Mg II, H $\gamma$ , H $\beta$ , H $\alpha$ , and the SBB are all weaker (Figure 4.13). These stronger ionization lines in the intrinsically red quasars indicate that they have more ionizing photons (harder SED) in the energy range  $\sim 13.6$ – $64.5$  eV ( $15.5 \lesssim \log(\nu[\text{Hz}]) \lesssim 16.2$ ) than the bluer quasars. Additionally, the width of H $\beta$  and Mg II are proportional to the mass of the central black hole, indicating that the bluer quasars likely have larger  $M_{\text{BH}}$ . Or if H $\beta$  is used as an indicator of inclination, the bluer quasars might be instead viewed closer to edge-on. We will take a closer look at these trends in Chapter 5.

When holding the intrinsic color fixed and looking at spectra with different amounts of reddening, we only see trends in C IV (weaker for more reddened quasars) and [O III] (stronger for more reddened quasars). In the BAL sample similar trends were found in C III] and C IV (stronger for redder quasars), and in addition we see that the absorption troughs are responding to the changes in the underlying SED (Figure 4.14).

## Chapter 5: Trends with Black Hole Properties

In Chapter 3 we explored the multi-wavelength quasar SEDs as the functions of various properties, but we did not consider them as a function of  $M_{\text{BH}}$  or accretion rate, as those quantities are determined more indirectly than the properties in Chapter 3. The analysis of Chapter 4 was restricted to the optical–UV photometry and the SDSS spectroscopy. Here we extend the analysis of Chapter 4 to the full mid-IR–X-ray SEDs and the analysis of Chapter 3 to the  $M_{\text{BH}}$  and  $\dot{M}_{\text{BH}}$  distributions. In §5.1 we construct mean SEDs as a functions of the quasars’ intrinsic colors and  $E(B - V)$  and correct them for dust extinction. Using the  $M_{\text{BH}}$  sample presented in §2.6, §5.2 explores how a quasar’s SED and  $BC_{2500 \text{ \AA}}$  change as functions of  $M_{\text{BH}}$  and the Eddington ratio ( $L/L_{\text{Edd}}$ ; a proxy for  $\dot{M}_{\text{BH}}$ ). Finally we conclude in §5.3.

### 5.1 Dust Corrected Mean SEDs

In §4.1.4 we showed that our quasars span a range of intrinsic colors and  $E(B - V)$  values. In particular, our sample was split over a  $10 \times 10$  grid in the parameter space span by  $E(B - V)$  and  $2.5\Delta(\alpha_\lambda)$ <sup>1</sup>. Given the uncertainties in the measurements of these quantities, this binning is weighted by the probability of a particular quasar belonging to any given bin (see §4.2 for more details). Using these bins and weights we have constructed mean SEDs as a function of both dust extinction and intrinsic color.

These mean SEDs were constructed in the same manner as the subsamples in §3.2: the observed data were shifted to the rest frame, placed on a common grid in  $\log(\nu)$ , missing data were gap-filled, and kriging was used to interpolate the data onto the rest of the grid. The SEDs were initially gap-filled using the mid-luminosity mean SED from §3.2.2 and mean SEDs were made for each bin in color– $E(B - V)$  space. To ensure the gap-filling is based on the observed properties of the quasars within each bin and not on the gap-filling model chosen, the resulting mean SEDs in each bin were used to gap-fill their respective bin. This process was repeated for 10 iterations, after which the mean SEDs did not change significantly.

To get an idea of how large of an effect the dust corrections have, we present the SEDs as a function of color and reddening both before and after dust correction. Since we will be using estimates of  $M_{\text{BH}}$  later in our analysis, we restrict our sample to the non-BAL quasars from Chapter 4. Figure 5.1 shows the resulting SEDs for each bin grouped by common intrinsic color before applying the extinction correction. Unlike Figure 4.11, here we are showing the full SED from the multi-wavelength photometry (as in Chapter 3) and not the composite spectra. To highlight differences in the mid-IR and optical regions, each mean SED has been normalized at the minimum value of their dip near  $1 \mu\text{m}$ . As seen in Chapter 4, there are very few non-BAL blue quasars with heavy reddening (see left panel of Figure 4.8). The clearest trend in these SEDs is the change in the optical–UV region where the SEDs with more dust extinction show more curvature than the SEDs

---

<sup>1</sup> $\Delta(\alpha_\lambda) = \alpha_{\lambda, \text{mode}} - \alpha_\lambda$  (see §4.1.2)

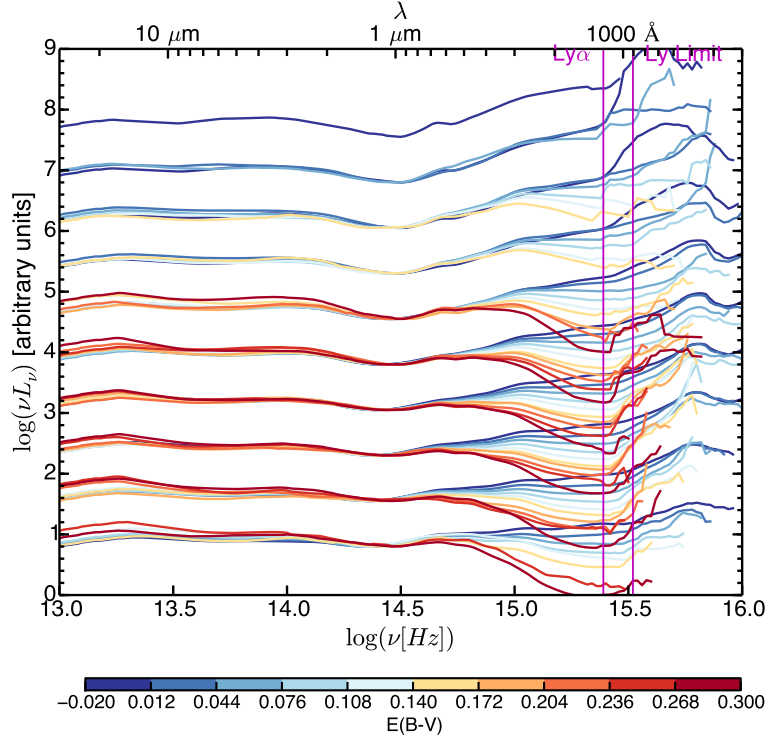


Figure 5.1 Mean SEDs for quasars grouped by intrinsic color with the intrinsically bluest quasars on top and the intrinsically reddest quasars on the bottom. The colors indicate the  $E(B - V)$  for each SED and the vertical magenta lines indicate the  $\text{Ly}\alpha$  and Ly Limit for reverence. As seen in Chapter 4, there are very few blue quasars with heavy reddening. All SEDs have been normalized at their minimum value near  $1 \mu\text{m}$ , and each grouping has been offset vertically for clarity.

with no extinction. There is also a slight trend in the mid-IR where the spectral index between  $7\text{--}11 \mu\text{m}$  becomes redder for the quasars with more dust extinction.

Figure 5.2 takes the same SEDs from Figure 5.1 but groups the SEDs by common  $E(B - V)$ . When grouped in this manner, there is a clear trend in the mid-IR where the intrinsically blue quasars have more hot dust emission than intrinsically red ones. This is similar to the trend seen in the high luminosity quasars from §3.2.2 and the high luminosity quasars from Gallagher et al. (2007). Additionally, the bluer quasars show more residual<sup>2</sup>  $\text{H}\alpha$  emission ( $6563 \text{\AA}$ ), consistent with the stacked spectra from §4.2.

The top group of Figure 5.2 are the SEDs that need the smallest correction for dust extinction. These SEDs provide reassurance that the binning from Chapter 4 worked as expected. As  $2.5\Delta(\alpha_\lambda)$  increases the SEDs become bluer, and these SEDs do not show any evidence of curvature in the optical–UV region.

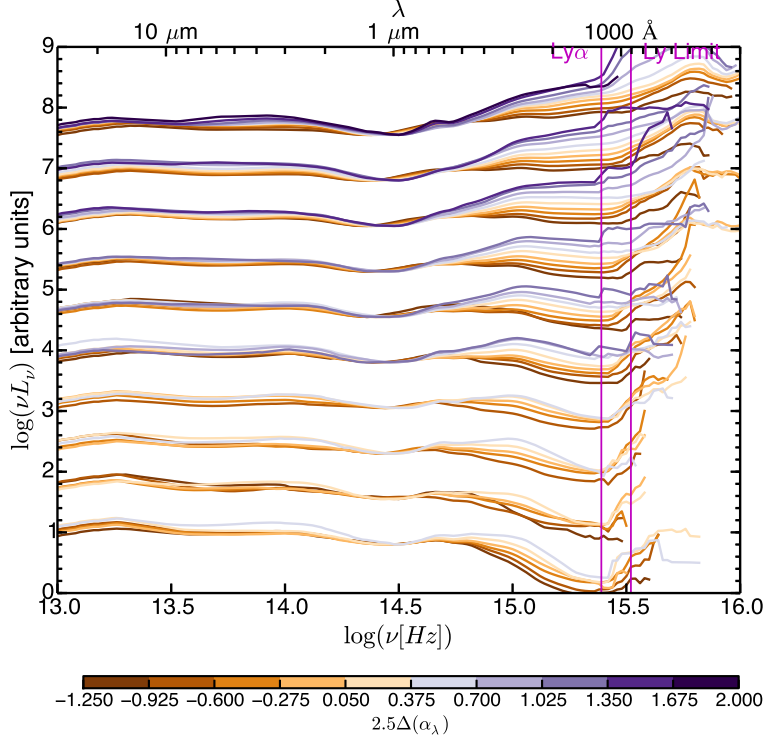


Figure 5.2 The same SEDs from Figure 5.1 grouped by  $E(B - V)$  with least reddened quasar on top and the most reddened quasars on the bottom. The colors indicate the intrinsic color for each SED and the vertical magenta lines indicate the  $\text{Ly}\alpha$  and Ly Limit for reference. There is a clear trend in the mid-IR with the blue quasars having more hot dust than the red quasars. The blue quasars also show a residual flux in the  $\text{H}\alpha$  line ( $6563 \text{ \AA}$ ). All SEDs have been normalized at their minimum value near  $1 \mu\text{m}$ , and each grouping has been offset vertically for clarity.

### 5.1.1 Applying Dust Corrections

With the SEDs gap-filled according to their observational properties, we can write Equation 1.17 in terms of the unreddened luminosity and use it to remove the effects of the dust extinction in the SEDs:

$$\log(\nu L_{\nu, \text{int}}) = \log(\nu L_{\nu, \text{obs}}) + E(B - V) \frac{R_{\lambda}}{2.5} \quad (5.1)$$

where  $\nu L_{\nu, \text{int}}$  is the quasar's intrinsic luminosity,  $\nu L_{\nu, \text{obs}}$  is its observed luminosity,  $E(B - V)$  is the extinction in the  $B - V$  color, and  $R_{\lambda}$  is a function that is dependent on the type of dust causing the reddening. To construct SEDs that are free from dust reddening, we began with the individual quasar SEDs from §5.1. Taking the SMC  $E(B - V)$  values from Chapter 4, we adjust the luminosities to their intrinsic values using Equation 5.1. For the uncertainties on  $E(B - V)$  we adopted the mean of the upper and lower  $1\sigma$  limits from Table 4.2 and added them in quadrature to the uncertainty in the luminosity for each filter. This dust correction was applied on top of the corrections from §3.1<sup>3</sup>.

<sup>2</sup>In §3.1.2 we remove the mean contribution of spectral lines in the SEDs.

<sup>3</sup>We only apply the correction for dust reddening up to the  $\text{Ly}\alpha$  line to avoid extrapolating the SMC reddening law into the EUV

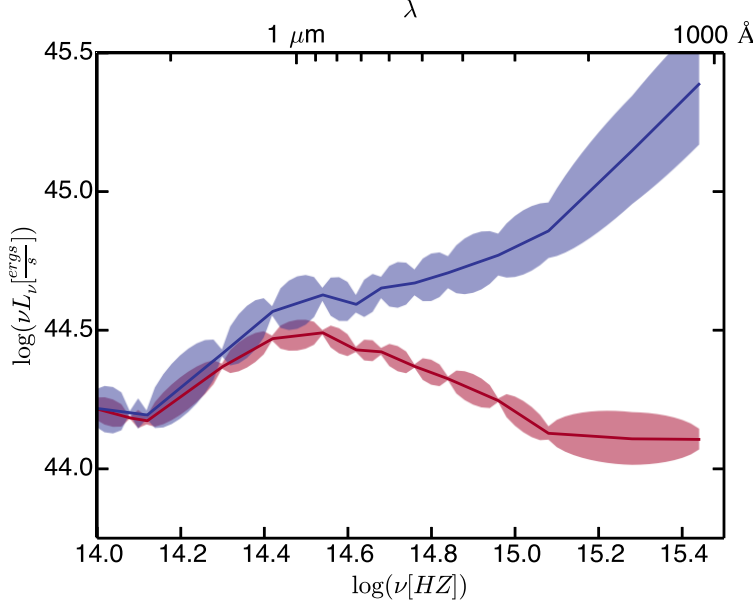


Figure 5.3 The optical–UV portion of a heavily reddened quasar’s SED before (red) and after (blue) correcting for dust reddening. The (kriged)  $1\sigma$  uncertainty regions are shaded in for both SEDs. Less than 0.1% of our sample needs a correction this extreme ( $E(B - V) = 0.2$ ).

Figure 5.3 shows an example of a heavily reddened SED before (red) and after (blue) correcting for dust reddening. The SED shown has an  $E(B - V) = 0.2$ ; less than 0.1% of our sample have corrections this extreme.

To calculate  $L_{bol}$  the SEDs need to be extended into the EUV and connected up with the X-ray. As discussed in detail in §3.4, there are many ways to extend SED into the EUV: connecting the last observed data point to the X-ray with a powerlaw, estimating the 500 Å point based on luminosity (Scott et al., 2004), or using a more theoretical model (Casebeer et al., 2006). To avoid making additional assumptions about our data, we adopt the first of these methods. For our luminosity integration range we used 1 μm–2 keV.

### 5.1.2 A Uniform Sample

As mentioned in §2.5, we are only using the uniformly selected quasars from SDSS DR7 (Richards et al., 2006b). One of the criteria for this sample is a uniform cut on the *observed i*-band magnitude of  $m_i < 19.1$ . Although this works well for creating a uniform sample in the observed-frame, using the  $L_{2500 \text{ \AA}}$  values for each quasar, we found this sample is not uniform in the rest-frame. This non-uniformity can be seen in Figure 5.4 where we show the (extinction corrected)  $L_{2500 \text{ \AA}}$  vs. redshift with the color of the data points representing the intrinsic spectral index. For  $z < 2$  we see that the redder quasars are seen down to a lower luminosity than bluer quasars, a direct artifact of the cut on  $m_i$ . The reason for this is that  $z < 2$  very blue objects with  $m_i = 19.1$  necessarily have a larger  $L_{2500 \text{ \AA}}$  values than red objects with the same *i*-band magnitude, and for  $z > 2$  the trend is reversed. To create a uniform sample in the rest-frame we define  $m_{2500}$  to be the (AB) magnitude

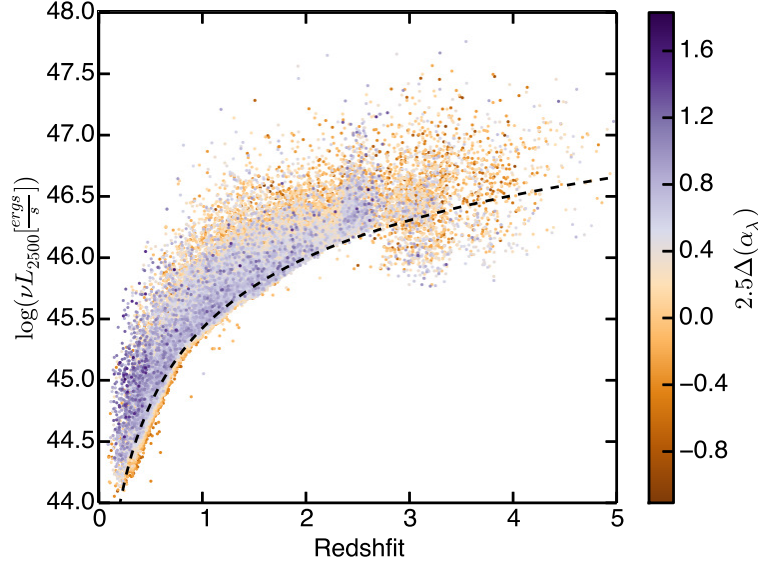


Figure 5.4  $L_{2500\text{\AA}}$  vs. redshift for our sample of quasars. The colors indicate the spectral index compared to the mode (see Chapter 4). The effects of cutting the sample on  $m_i < 19.1$  can be clearly seen for  $z < 2$  in that the redder quasars are seen down to lower intrinsic luminosities than the bluer ones. The black dashed line shows the cut used to remove this bias.

associated with  $L_{2500\text{\AA}}$ :

$$m_{2500} = 2.5 \times \left[ 0.738 + 2 \log \left( \frac{D_L}{m} \right) - \log(1+z) - \log \left( \frac{\nu L_{2500\text{\AA}}}{\text{erg s}^{-1}} \right) \right] \quad (5.2)$$

where the first term is a constant associated with the AB system,  $D_L$  is the luminosity distance, and  $z$  is the redshift. Applying the cut  $m_{2500} < 19.1$  (black dashed line in Figure 5.4) removes the bias caused by the cut on the  $i$ -band magnitude.

### 5.1.3 Extinction Corrected SEDs

With this newly defined uniform sample and extinction corrected SEDs we are able to explore the mean SEDs as functions of color and extinction. Figure 5.5 shows the mean SEDs based on  $E(B-V)$  (*left*) and intrinsic color (*right*) after marginalizing over the other variable (e.g. the blue line in the left panel shows the mean SED for all quasars with  $E(B-V) < 0.012$  regardless of intrinsic color). To ensure the differences seen in the mean SEDs are being caused by the variable of interest, the redshift distribution for each SED have been matched within each panel. When making the uniform redshift distributions we dropped the three bins with the most dust extinction and the two intrinsically bluest bins due to low number counts ( $< 100$  quasars in the bin).

With the fully stacked SEDs, the trend in  $E(B-V)$  seen in the mid-IR from Figure 5.1 has become stronger. The spectral index from 5–11  $\mu\text{m}$  becomes redder as the amount of dust extinction increases. The differences in these SEDs indicate there is a sample selection and/or intrinsic effect that is a function of  $E(B-V)$ . If this was not the case, all differences in the SEDs would be averaged

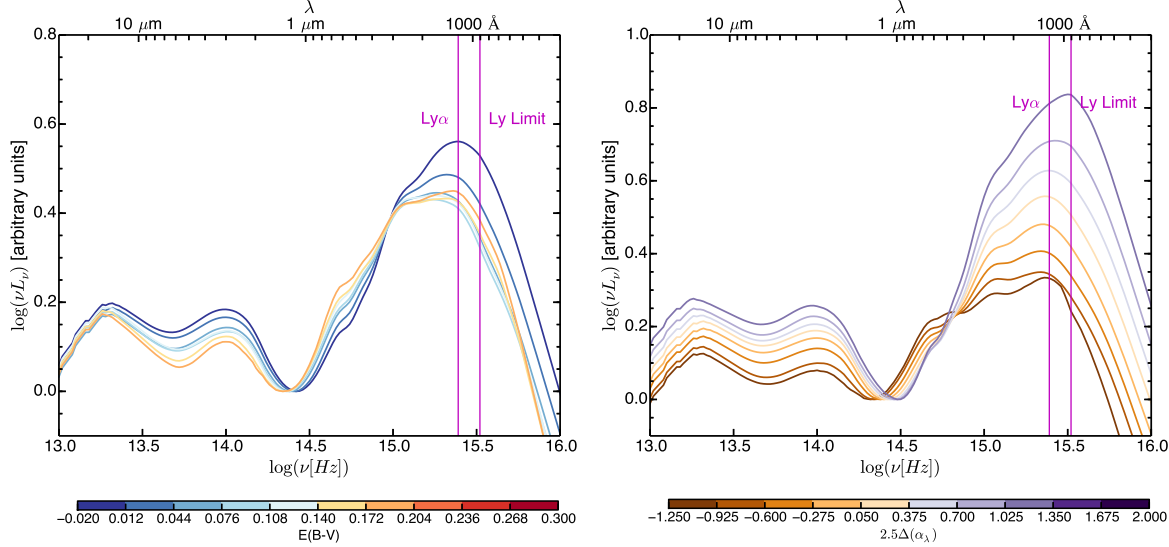


Figure 5.5 Redshift matched and extinction corrected SEDs as a function of  $E(B - V)$  (*left*) and intrinsic color (*right*). *Left:* SEDs with more dust extinction show less hot dust and a redder spectral index between  $5\text{--}11\,\mu\text{m}$ . *Right:* Intrinsically bluer quasars show more hot dust emission and have their BBBs peak at shorter wavelengths than the red quasars. The bluest mean SED has  $\alpha_\nu \sim 0.03$ . All SEDs have been normalized at their minimum value near  $1\,\mu\text{m}$ .

away. A full analysis of the possible causes for these differences is beyond the scope of this work.

As in Figure 5.2, we find bluer quasars have more hot dust emission than redder quasars. Additionally, their big blue bumps (BBBs) also peak at shorter wavelengths, consistent with the bluer quasars having a hotter accretion disk. However, this seems to be in contention with the stacked spectra from §4.2 where the bluer quasars had weaker ionized spectral lines, indicating they have less ionizing radiation in the range of  $\sim 200\text{--}1000\,\text{\AA}$  ( $\sim 12\text{--}60\,\text{eV}$ ). If the bluer quasars have their BBB peak at shorter wavelengths we would naively expect them to also have more ionizing radiation, and stronger ionized spectral lines.

One possible explanation for this discrepancy is inclination angle. As the inclination angle is increased from face-on to edge-on, the apparent SED becomes bluer,  $L_{2500\,\text{\AA}}$  becomes smaller, and the BBB is shifted to shorter wavelengths (Sun & Malkan, 1989). These changes are correlated such that  $L_{\text{bol}}$  is independent of inclination, resulting in an increase in  $BC_{2500\,\text{\AA}}$ . Although the observed SED has more ionizing radiation, the broad line region (BLR) is seeing the accretion disk closer to face-on, and as a result, sees *less* ionizing radiation. This idea that the BLR sees a different continuum than we do is not a new one; Korista et al. (1997) was lead to the same conclusion when trying to reconcile the emission lines of Mrk 335 with the observed EUV continuum. However, not all of the changes in the intrinsic color SEDs can be attributed to inclination, since the  $L_{2500\,\text{\AA}}$  distribution is the same for all of the color bins (see Figure 5.6).

Using these SEDs we also look at the distributions for  $L_{2500\,\text{\AA}}$  and  $BC_{2500\,\text{\AA}}$  as functions of intrinsic color and  $E(B - V)$ . This was done by modeling the probability distribution for the parameter of interest (e.g.  $L_{2500\,\text{\AA}}$  or  $BC_{2500\,\text{\AA}}$ ) as a normal distribution centered on the measured value and

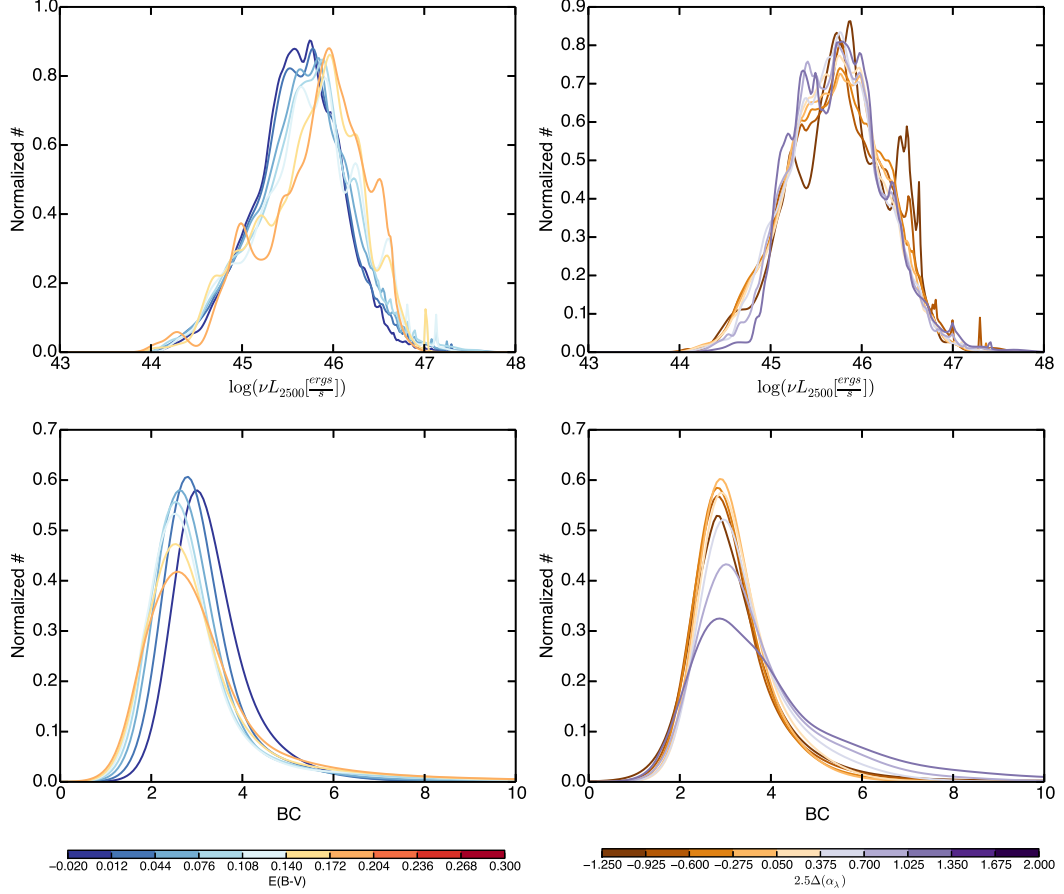


Figure 5.6 The fully marginalized  $L_{2500 \text{ \AA}}$  (*top*) and  $BC_{2500 \text{ \AA}}$  (*bottom*) distributions for  $E(B-V)$  bins (*left*) and for intrinsic color bins (*right*). From the  $L_{2500 \text{ \AA}}$  plots we can see that the dusty quasars are intrinsically more luminous while there are no trends in luminosity with intrinsic color. The  $BC_{2500 \text{ \AA}}$  plots show a trend for more reddened quasars have smaller  $BC_{2500 \text{ \AA}}$ , while intrinsic color shows bluer quasars have larger  $BC_{2500 \text{ \AA}}$ .

having a width given by the  $1\sigma$  uncertainty. This distribution is weighted by the likelihood that the quasar belongs to a given color or  $E(B-V)$  bin and all distributions belonging to a common bin are summed together and the result is normalized such that it integrates to unity.

Figure 5.6 show the resulting marginalized distributions for  $L_{2500 \text{ \AA}}$  (*top*) and  $BC_{2500 \text{ \AA}}$  (*bottom*) for  $E(B-V)$  bins (*left*) and intrinsic color bins (*right*). For  $L_{2500 \text{ \AA}}$  we only see a tend with  $E(B-V)$ . There are (relatively) more high luminosity quasars with high dust extinction than low dust extinction.

For both parameters we see trends in the *corrected*  $BC_{2500 \text{ \AA}}$  distributions. In the lower left panel of Figure 5.6 we see  $BC_{2500 \text{ \AA}}$  becomes smaller as  $E(B-V)$  increases, a result of their higher  $L_{2500 \text{ \AA}}$  distribution. Looking at the trends with intrinsic color we see the bluer quasars have higher  $BC_{2500 \text{ \AA}}$ . As stated earlier, this trend could be caused by inclination effects, where some of the bluer quasars are viewed closer to edge-on.

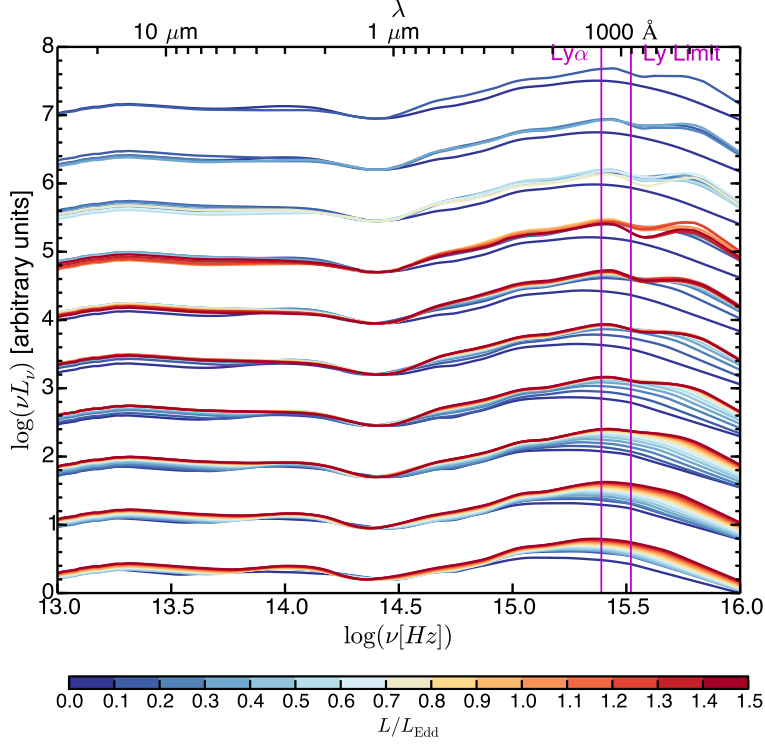


Figure 5.7 Mean SEDs for quasars grouped by  $M_{\text{BH}}$  with the most massive SEDs on the top and the colors indicating  $L/L_{\text{Edd}}$ . As  $L/L_{\text{Edd}}$  increases the peak of the BBB shifts to lower wavelengths, indicating a hotter accretion disk. All SEDs have been normalized at their minimum near  $1 \mu\text{m}$  and each grouping has been offset vertically for clarity.

## 5.2 SEDs Based on $M_{\text{BH}}$ and $L/L_{\text{Edd}}$

The standard optically-thick geometrically-thin accretion disk from Shakura & Sunyaev (1973, see §1.1 for a review of the  $\alpha$ -disk model) predicts that the temperature of the disk is proportional to the accretion rate ( $\dot{M}/\dot{M}_{\text{Edd}}$ ) and inversely proportional to  $M_{\text{BH}}$  (see Equation 1.1). If a quasar's spectral index is heavily influenced by the turnover in the BBB, the  $\alpha$ -disk model would predict quasars with higher accretion rates to be bluer and quasars with higher  $M_{\text{BH}}$  to be redder. We can test this prediction by constructing SEDs based on our estimated values of  $M_{\text{BH}}$  (§2.6) and using the Eddington fraction:

$$\frac{\dot{M}}{\dot{M}_{\text{Edd}}} = \frac{L}{L_{\text{Edd}}} = \frac{L_{\text{bol}}}{L_{\text{Edd}}} \propto \frac{L_{\text{bol}}}{M_{\text{BH}}} \quad (5.3)$$

as a proxy for the accretion rate (see §1.1.2). From the final proportionality we can see that the accretion rate is also inversely proportional to  $M_{\text{BH}}$ , so to isolate changes in the quasar's SEDs that are only caused by changes  $M_{\text{BH}}$  or  $L/L_{\text{Edd}}$  it is important to hold the other variable in a fixed range.

As we did for the quasars' color and dust properties in §5.1, we bin our data based on the measured values for  $\log(M_{\text{BH}})$  and  $L/L_{\text{Edd}}$ . Since these parameters are correlated (see Equation 5.3) and not

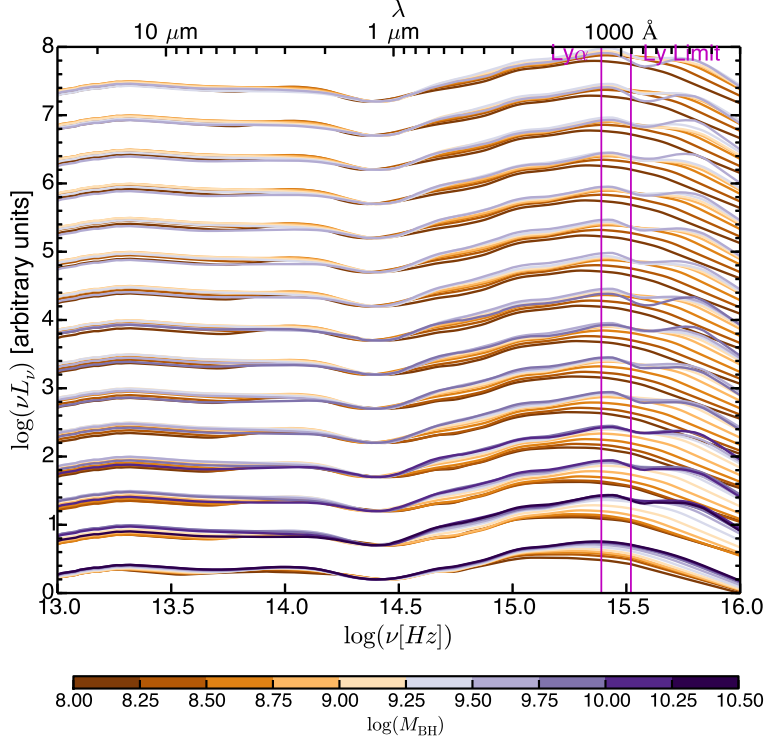


Figure 5.8 Mean SEDs for quasars grouped by  $L/L_{\text{Edd}}$  with the largest ratio on the top and the colors indicating  $M_{\text{BH}}$ . The higher mass SEDs show an initial peak in the BBB at shorter wavelengths than the low mass SEDs and also show an extra bump in the EUV (see text). All SEDs have been normalized at their minimum near  $1 \mu\text{m}$  and each grouping has been offset vertically for clarity.

known to high accuracy, we weight each quasar by its probability of belonging to each bin. To find these weights we use a Monte Carlo (MC) method: for each quasar we simulate 10,000  $\log(M_{\text{BH}})$  and  $\log(L_{\text{bol}})$  values taken from (uncorrelated) normal distributions centered on the measured values and having widths equal to the  $1\sigma$  uncertainties. Each pair of simulated values were used to calculate a simulated  $L/L_{\text{Edd}}$ , keeping intact the covariance between  $L/L_{\text{Edd}}$  and  $\log(M_{\text{BH}})$ . The fraction of simulated points landing in each bin gives an estimate for the probability of the quasars belonging to that bin.

For our sample we used 10 bins in  $\log(M_{\text{BH}})$  (between 8–10.5) and 15 bins in  $L/L_{\text{Edd}}$  (between 0–1.5). The resulting SEDs grouped by  $\log(M_{\text{BH}})$  are shown in Figure 5.7 and the same SEDs grouped by  $L/L_{\text{Edd}}$  are shown in Figure 5.8. As expected, we see for a given  $\log(M_{\text{BH}})$  bin the quasars with higher  $L/L_{\text{Edd}}$  have more hot dust emission in the mid-IR and their BBB peaks at shorter wavelengths, both consistent with the accretion disk having a higher temperature. We also note that the higher  $\log(M_{\text{BH}})$  bins show an additional bump in the EUV. This bump is highly dependent on the EUV extrapolation and gap-filling method used, and more work needs to be done to determine if this trend is real or just an artifact of our data analysis. When grouping the quasars by  $\log(M_{\text{BH}})$  we see a similar trend where more massive quasars are consistent with having a hotter accretion disk, the opposite trend that the  $\alpha$ -disk theory predicts.

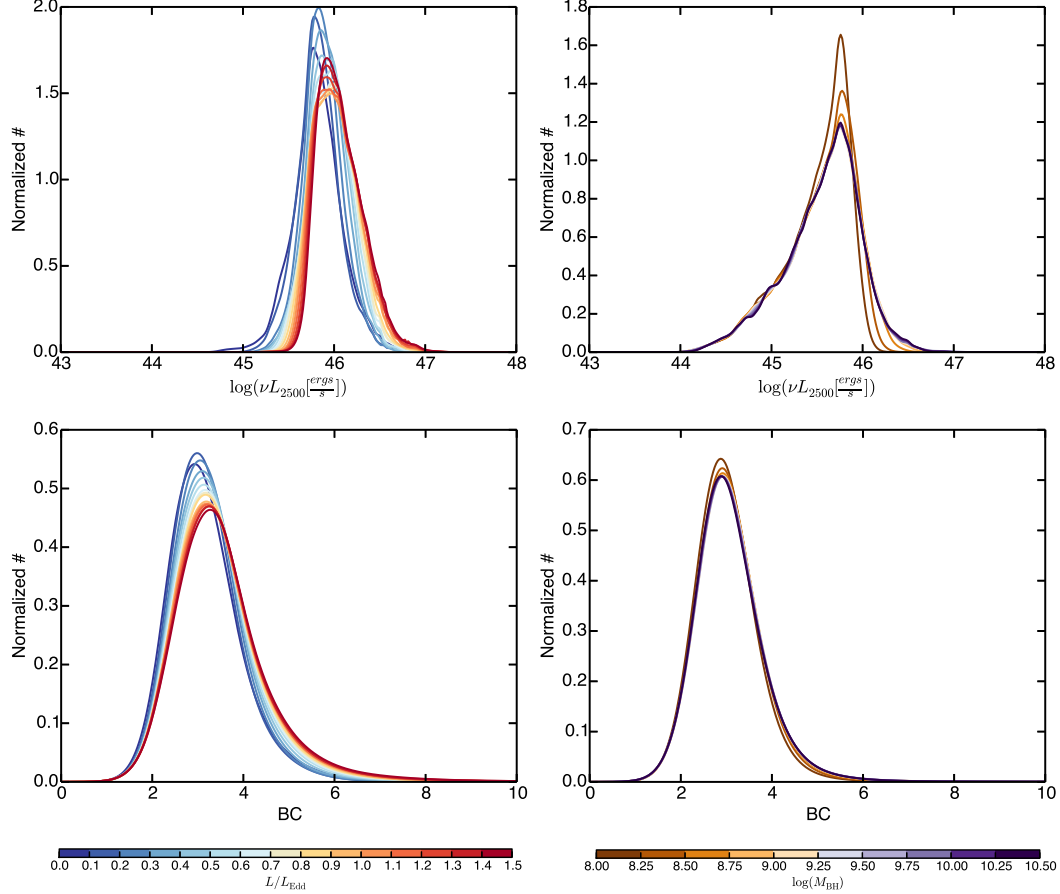


Figure 5.9 The fully marginalized  $L_{2500 \text{ \AA}}$  (top) and  $\text{BC}_{2500 \text{ \AA}}$  (bottom) distributions grouped by common  $L/L_{\text{Edd}}$  (left) and  $M_{\text{BH}}$  (right). As expected both  $L_{2500 \text{ \AA}}$  and  $\text{BC}_{2500 \text{ \AA}}$  are positively correlated with  $L/L_{\text{Edd}}$ . There is a slight trend for higher  $M_{\text{BH}}$  quasars to have higher  $L_{2500 \text{ \AA}}$ , and there are no trends with  $\text{BC}_{2500 \text{ \AA}}$ .

Figure 5.9 shows the marginalized distributions for  $L_{2500 \text{ \AA}}$  and  $\text{BC}_{2500 \text{ \AA}}$  based on  $\log(M_{\text{BH}})$  and  $L/L_{\text{Edd}}$  after picking sub-samples with common redshift distributions. Both  $\text{BC}_{2500 \text{ \AA}}$  and  $L/L_{\text{Edd}}$  are proportional to  $L_{\text{bol}}$ , so we expect these two values to be correlated, and  $L/L_{\text{Edd}}$  to increase with luminosity. Both of these trends are seen clearly in the data. Looking at  $\log(M_{\text{BH}})$  we see  $L_{2500 \text{ \AA}}$  becomes slightly larger for more massive quasars and we find no significant changes in  $\text{BC}_{2500 \text{ \AA}}$ .

### 5.3 Conclusions

Using the individual quasar's SEDs from Chapter 3 and the extinction characterized in Chapter 4 we corrected the observed SEDs for dust reddening. With these corrected SEDs we found trends with both intrinsic color and  $E(B - V)$ . Bluer quasars show stronger emission around  $3 \mu\text{m}$  and a shift in the minimum near  $1 \mu\text{m}$  to shorter wavelengths (right panel of Figure 5.5), both evidence for stronger hot dust emission. These quasars also have their BBB peak further into the UV, indicative

of a hotter accretion disk, and have a higher BC<sub>2500 Å</sub>° distribution (bottom right panel of Figure 5.6). The shift in the BBB and increase in BC<sub>2500 Å</sub>° could also be explained if some of the blue quasars are actually intrinsically red, but are seen closer to edge-on, an explanation that helps to reconcile the weak ionizing lines seen in the composite spectra with the relatively hard SEDs seen in the EUV. We also find evidence for either an observational bias or intrinsic effect that changes the shape of the SED as a function of E(B – V). Although, it is unclear at this time what the cause of these changes are.

Using these corrected SEDs as a stepping stone, we constructed mean SEDs based on log( $M_{\text{BH}}$ ) and  $L/L_{\text{Edd}}$  (a proxy for accretion rate). Quasars with larger  $L/L_{\text{Edd}}$  were bluer, had BBB that peaked at shorter wavelengths, and more hot dust emission in the mid-IR. All of these trends are expected from the  $\alpha$ -disk model where large  $L/L_{\text{Edd}}$  corresponds with a hotter accretion disk. If the  $\alpha$ -disk model is correct, we would expect to see the opposite trend as log( $M_{\text{BH}}$ ) is increased. Instead, we see the same trends as we did with increasing  $L/L_{\text{Edd}}$ , indicating that the quasars with larger log( $M_{\text{BH}}$ ) also have hotter accretion disks. These large log( $M_{\text{BH}}$ ) SEDs also show an additional bump in the EUV, but it is unclear if this trend is real or an artifact of our data analysis. As expected, we found quasars with large  $L/L_{\text{Edd}}$  also had higher luminosities and larger BC<sub>2500 Å</sub>°. There was also a slight trend with higher mass quasars also having higher luminosities, but no trend was found between log( $M_{\text{BH}}$ ) and BC<sub>2500 Å</sub>°.

## Chapter 6: Conclusions

The physics that drives the accretion of matter onto the central black hole (in its simplest form) only relies on three parameters:  $M_{\text{BH}}$ ,  $\dot{M}_{\text{BH}}$ , and the spin of the central black hole. As such, constructing SEDs based on these quantities would provide the most insight into the physics of the quasar. Both  $M_{\text{BH}}$  and  $\dot{M}_{\text{BH}}$  can be estimated from the data, but to do so accurate *intrinsic*  $L_{\text{bol}}$  values must be obtained for each quasars in our sample.

Before looking for trends in quasar SEDs based on estimated quantities, in Chapter 3 we explored changes in our SEDs based our various observational properties. In particular, we looked at the observed luminosity ( $L_{\text{2500 \AA}}$ ) and properties of the C IV emission line. We created three luminosity-dependent mean SEDs and found the high-luminosity quasars had bluer optical continua and more hot dust emission than low-luminosity quasars. Additionally, we found  $\alpha_{\text{FUV}}$  to be dependent on luminosity in the sense that more luminous quasars have redder  $\alpha_{\text{FUV}}$  continua, consistent with Scott et al. (2004). When looking at the C IV properties, we saw differences in the Balmer continuum, Ly $\alpha$  and C IV (by construction) line strengths that are consistent with eigenvector 1 trends (Brotherton & Francis, 1999).

In addition to these mean SEDs, we also constructed individual SEDs and found bolometric corrections for each quasars. We found that the more significant contribution to the BC<sub>2500 Å</sub> distribution was not the observed IR–near-UV parts of the SED, but instead the unseen EUV part of the SED. Given these findings, it is important to consider potentially significant differences in the EUV part of the SED at the extrema of the quasars population.

One of the biggest secondary effects that change the shape of the observed SED in the optical–UV (and hence  $L_{\text{bol}}$ ) is dust extinction associated with the quasar. In Chapter 4 we used our mid-IR–UV photometric data to calculate the intrinsic colors and amount of extinction in each quasar assuming various dust reddening laws. Using a hierarchical Bayesian model we broke the degeneracy typically seen between these variables, and bounded them within a physical range. The majority of our data were well fit by an SMC reddening law, but a small set were just as well fit by the steeper multi-scattering law from Leighly et al. (2014). From the individual fits we found the BAL quasars tend to be slightly bluer and have more extinction then the non-BAL quasars, and in general the BAL fraction is very dependent on the intrinsic color and amount of extinction in the quasar sample.

Looking at composite spectra as functions for extinction and intrinsic color revealed trends in both the BAL and non-BAL samples. On average, we found the fit values based on the photometry do a good job of reproducing the slopes and curvatures seen in the composite spectra. With the BAL spectra we also found the width and depth of the C IV absorption troughs changed with both color and extinction.

To look for trends in the spectra based on a quasar’s intrinsic color, we compared the spectra in the lowest reddening bin. In general, the intrinsically red quasars have stronger ionized spectral lines (e.g. C IV, He II, C III], and [O II]), while the bluer quasars have stronger Balmer lines (e.g. H $\gamma$ , H $\beta$ , H $\alpha$ , and the SBB). These trends are consistent with the redder quasars having a harder SED in

the EUV than the bluer quasars. In the BAL spectra, similar trends were found, and additionally, the absorption troughs respond to changes in the underlying SED.

In Chapter 5 we extended the analysis of Chapter 4 by constructing full SEDs as function of color and extinction. Using the SMC extinction values, the effects of dust reddening were removed from the SEDs, allowing us to study the intrinsic SEDs. From these SEDs, we found trends with both color and extinction. Although the cause is unclear, we found evidence for either an observational bias or intrinsic effect that changes the SEDs as a function of  $E(B - V)$ . Additionally, the intrinsically bluer quasars have more hot dust, a BBB peaking at shorter wavelengths, and higher  $BC_{2500\text{\AA}}$ . In the EUV, the blue SEDs are harder than the spectra from Chapter 4 would suggest. In order to reconcile the SEDs with the spectra, we conclude that the BLR sees a very different continuum (face-on) than we do (edge-on).

These (internal) extinction corrected SEDs allowed us to shift our analysis to the more physical properties of  $M_{\text{BH}}$  and accretion rate (estimated with  $L/L_{\text{Edd}}$ ). As predicted by the  $\alpha$ -disk theory of Shakura & Sunyaev (1973), we found the quasars with high accretion rates have SEDs consistent with hotter accretion disks. As expected, these quasars were also more luminous and had higher  $BC_{2500\text{\AA}}$ . Contrary to the  $\alpha$ -disk theory, the quasars with large  $M_{\text{BH}}$  were also consistent with a hotter accretion disk. These SEDs were also slightly more luminous than the SEDs with smaller  $M_{\text{BH}}$ , and there were no significant trends in  $BC_{2500\text{\AA}}$ .

## Bibliography

- Annis, J., Soares-Santos, M., Strauss, M. A., et al. 2011, ArXiv e-prints, arXiv:1111.6619 [astro-ph.CO]
- Antonucci, R. 1993, *ARA&A*, 31, 473
- Ashby, M. L. N., Stern, D., Brodwin, M., et al. 2009, *ApJ*, 701, 428
- Assef, R. J., Kochanek, C. S., Brodwin, M., et al. 2010, *ApJ*, 713, 970
- Avni, Y., & Tananbaum, H. 1982, *ApJ*, 262, L17
- Baldwin, J. A. 1977, *ApJ*, 214, 679
- Baskin, A., Laor, A., & Hamann, F. 2013, *MNRAS*, 432, 1525
- Becker, R. H., White, R. L., Gregg, M. D., et al. 2000, *ApJ*, 538, 72
- Beckmann, V., & Shrader, C. R. 2012, Active Galactic Nuclei
- Bentz, M. C., Peterson, B. M., Netzer, H., Pogge, R. W., & Vestergaard, M. 2009, *ApJ*, 697, 160
- Bentz, M. C., Peterson, B. M., Pogge, R. W., Vestergaard, M., & Onken, C. A. 2006, *ApJ*, 644, 133
- Bentz, M. C., Denney, K. D., Grier, C. J., et al. 2013, *ApJ*, 767, 149
- Binney, J., & Merrifield, M. 1998, Galactic Astronomy (Princeton University Press)
- Boroson, T. A., & Green, R. F. 1992, *ApJS*, 80, 109
- Bovy, J., Myers, A. D., Hennawi, J. F., et al. 2011, ArXiv e-prints, arXiv:1105.3975 [astro-ph.CO]
- . 2012, *ApJ*, 749, 41
- Brotherton, M. S., & Francis, P. J. 1999, in Astronomical Society of the Pacific Conference Series, Vol. 162, Quasars and Cosmology, ed. G. Ferland & J. Baldwin, 395
- Budavári, T., Heinis, S., Szalay, A. S., et al. 2009, *ApJ*, 694, 1281
- Calzetti, D., Bohlin, R. C., Kinney, A. L., Storchi-Bergmann, T., & Heckman, T. M. 1995, *ApJ*, 443, 136
- Casebeer, D. A., Leighly, K. M., & Baron, E. 2006, *ApJ*, 637, 157
- Churchill, C., Steidel, C., & Kacprzak, G. 2005, in Astronomical Society of the Pacific Conference Series, Vol. 331, Extra-Planar Gas, ed. R. Braun, 387
- Collin-Souffrin, S., Dyson, J. E., McDowell, J. C., & Perry, J. J. 1988, *MNRAS*, 232, 539
- Croom, S., Boyle, B., Shanks, T., et al. 2004, in Multiwavelength AGN Surveys, ed. R. Mújica & R. Maiolino, 57
- Croom, S. M., Rhook, K., Corbett, E. A., et al. 2002, *MNRAS*, 337, 275
- Croom, S. M., Richards, G. T., Shanks, T., et al. 2009, *MNRAS*, 392, 19
- Denney, K. D. 2012, *ApJ*, 759, 44

- Denney, K. D., Pogge, R. W., Assef, R. J., et al. 2013, ApJ, 775, 60
- Deo, R. P., Richards, G. T., Nikutta, R., et al. 2011, ApJ, 729, 108
- Di Matteo, T., Springel, V., & Hernquist, L. 2005, Nature, 433, 604
- Djorgovski, S. G., Volonteri, M., Springel, V., Bromm, V., & Meylan, G. 2008, ArXiv e-prints, arXiv:0803.2862
- Done, C., Davis, S. W., Jin, C., Blaes, O., & Ward, M. 2012, MNRAS, 420, 1848
- Draine, B. T. 2003, ARA&A, 41, 241
- Elitzur, M., & Shlosman, I. 2006, ApJ, 648, L101
- Elvis, M., Wilkes, B. J., McDowell, J. C., et al. 1994, ApJS, 95, 1
- Fabian, A. C. 1999, Proceedings of the National Academy of Science, 96, 4749
- Ferland, G. J. 2002, Hazy, A Brief Introduction to Cloudy 96
- Fioc, M., & Rocca-Volmerange, B. 1997, A&A, 326, 950
- Foreman-Mackey, D., Hogg, D. W., Lang, D., & Goodman, J. 2013, PASP, 125, 306
- Fukugita, M., Ichikawa, T., Gunn, J. E., et al. 1996, AJ, 111, 1748
- Fynbo, J. P. U., Krogager, J.-K., Venemans, B., et al. 2013, ApJS, 204, 6
- Gallagher, S. C., Richards, G. T., Lacy, M., et al. 2007, ApJ, 661, 30
- Gaskell, C. M., & Goosmann, R. W. 2013, ApJ, 769, 30
- Gaskell, C. M., Goosmann, R. W., Antonucci, R. R. J., & Whysong, D. H. 2004, ApJ, 616, 147
- Gelman, A., & Hill, J. 2006, Data Analysis Using Regression and Multilevel/Hierarchical Models, 1st edn. (Cambridge University Press)
- George, I. M., Turner, T. J., Yaqoob, T., et al. 2000, ApJ, 531, 52
- Glikman, E., Helfand, D. J., White, R. L., et al. 2007, ApJ, 667, 673
- Goobar, A. 2008, ApJ, 686, L103
- Graham, A. W., Onken, C. A., Athanassoula, E., & Combes, F. 2011, MNRAS, 412, 2211
- Green, P. J., Aldcroft, T. L., Richards, G. T., et al. 2009, ApJ, 690, 644
- Gregg, M. D., Lacy, M., White, R. L., et al. 2002, ApJ, 564, 133
- Grupe, D., Komossa, S., Leighly, K. M., & Page, K. L. 2010, ApJS, 187, 64
- Hastings, W. K. 1970, Biometrika, 57, 97
- Heckman, T., & Best, P. 2014, ArXiv e-prints, arXiv:1403.4620 [astro-ph.GA]
- Hewett, P. C., & Foltz, C. B. 2003, AJ, 125, 1784
- Hewett, P. C., Warren, S. J., Leggett, S. K., & Hodgkin, S. T. 2006, MNRAS, 367, 454
- Hopkins, P. F., & Hernquist, L. 2009, ApJ, 694, 599
- Hopkins, P. F., Hernquist, L., Cox, T. J., et al. 2006, ApJS, 163, 1
- Hopkins, P. F., Strauss, M. A., Hall, P. B., et al. 2004, AJ, 128, 1112

- Hubeny, I., & Hubeny, V. 1997, ApJ, 484, L37
- Jarosik, N., Bennett, C. L., Dunkley, J., et al. 2011, ApJS, 192, 14
- Just, D. W., Brandt, W. N., Shemmer, O., et al. 2007, ApJ, 665, 1004
- Kaspi, S., Maoz, D., Netzer, H., et al. 2005, ApJ, 629, 61
- Kaspi, S., Smith, P. S., Netzer, H., et al. 2000, ApJ, 533, 631
- Kauffmann, G., & Haehnelt, M. 2000, MNRAS, 311, 576
- Kelly, B. C. 2011, Journal of Computational and Graphical Statistics, 20, 584
- Kelly, B. C., Shetty, R., Stutz, A. M., et al. 2012, ApJ, 752, 55
- Khare, P., vanden Berk, D., York, D. G., Lundgren, B., & Kulkarni, V. P. 2012, MNRAS, 419, 1028
- Kochanek, C. S., Eisenstein, D. J., Cool, R. J., et al. 2012, ApJS, 200, 8
- Korista, K., Ferland, G., & Baldwin, J. 1997, ApJ, 487, 555
- Kormendy, J., & Richstone, D. 1995, ARA&A, 33, 581
- Kozłowski, S., Kochanek, C. S., Udalski, A., et al. 2010, ApJ, 708, 927
- Kratzer, R. M., & Richards, G. T. 2014, ArXiv e-prints, arXiv:1405.2344
- Krawczyk, C. M., Richards, G. T., Mehta, S. S., et al. 2013, ApJS, 206, 4
- Krolik, J. H. 1999, Active galactic nuclei : from the central black hole to the galactic environment
- Krolik, J. H., & Begelman, M. C. 1988, ApJ, 329, 702
- Kruczek, N. E., Richards, G. T., Gallagher, S. C., et al. 2011, AJ, 142, 130
- Lacy, M., Wilson, G., Masci, F., et al. 2005, ApJS, 161, 41
- Lawrence, A. 2012, MNRAS, 423, 451
- Lawrence, A., Warren, S. J., Almaini, O., et al. 2007, MNRAS, 379, 1599
- Leighly, K., Halpern, J., & Jenkins, E. 2004, in Astronomical Society of the Pacific Conference Series, Vol. 311, AGN Physics with the Sloan Digital Sky Survey, ed. G. T. Richards & P. B. Hall, 277
- Leighly, K. M., & Moore, J. R. 2004, ApJ, 611, 107
- Leighly, K. M., Terndrup, D. M., Baron, E., et al. 2014, ApJ, 788, 123
- Lonsdale, C. J., Smith, H. E., Rowan-Robinson, M., et al. 2003, PASP, 115, 897
- Lusso, E., Comastri, A., Vignali, C., et al. 2010, A&A, 512, A34
- Lynden-Bell, D. 1969, Nature, 223, 690
- Lynds, R. 1971, ApJ, 164, L73
- Maddox, N., & Hewett, P. C. 2006, MNRAS, 367, 717
- Marconi, A., Risaliti, G., Gilli, R., et al. 2004, MNRAS, 351, 169
- Martin, D. C., Fanson, J., Schiminovich, D., et al. 2005, ApJ, 619, L1
- McLure, R. J., & Dunlop, J. S. 2004, MNRAS, 352, 1390

- Meiksin, A. 2006, MNRAS, 365, 807
- Ménard, B., Nestor, D., Turnshek, D., et al. 2008, MNRAS, 385, 1053
- Merloni, A., Bongiorno, A., Brusa, M., et al. 2014, MNRAS, 437, 3550
- Metropolis, N., Rosenbluth, A., Rosenbluth, M., Teller, A., & Teller, E. 1953, J. of Chem. Phys., 21, 1087
- Murray, N., Chiang, J., Grossman, S. A., & Voit, G. M. 1995, ApJ, 451, 498
- Nemmen, R. S., & Brotherton, M. S. 2010, MNRAS, 408, 1598
- Netzer, H., & Davidson, K. 1979, MNRAS, 187, 871
- Onken, C. A., Ferrarese, L., Merritt, D., et al. 2004, ApJ, 615, 645
- Park, D., Kelly, B. C., Woo, J.-H., & Treu, T. 2012, ApJS, 203, 6
- Park, D., Woo, J.-H., Denney, K. D., & Shin, J. 2013, ApJ, 770, 87
- Pei, Y. C. 1992, ApJ, 395, 130
- Peterson, B. M. 2011, ArXiv e-prints, arXiv:1109.4181 [astro-ph.CO]
- Peth, M. A., Ross, N. P., & Schneider, D. P. 2011, AJ, 141, 105
- Pier, E. A., & Krolik, J. H. 1992, ApJ, 401, 99
- Prochaska, J. X., O'Meara, J. M., & Worseck, G. 2010, ApJ, 718, 392
- Proga, D., Stone, J. M., & Kallman, T. R. 2000, ApJ, 543, 686
- Rafiee, A., & Hall, P. B. 2011, MNRAS, 415, 2932
- Reichard, T. A., Richards, G. T., Schneider, D. P., et al. 2003a, AJ, 125, 1711
- Reichard, T. A., Richards, G. T., Hall, P. B., et al. 2003b, AJ, 126, 2594
- Richards, G. T., Hall, P. B., Vanden Berk, D. E., et al. 2003, AJ, 126, 1131
- Richards, G. T., Lacy, M., Storrie-Lombardi, L. J., et al. 2006a, ApJS, 166, 470
- Richards, G. T., Strauss, M. A., Fan, X., et al. 2006b, AJ, 131, 2766
- Richards, G. T., Kruczak, N. E., Gallagher, S. C., et al. 2011, AJ, 141, 167
- Runnoe, J. C., Brotherton, M. S., & Shang, Z. 2012, ArXiv e-prints, arXiv:1201.5155 [astro-ph.CO]
- Rybicki, G. B., & Lightman, A. P. 1986, Radiative Processes in Astrophysics
- Rybicki, G. B., & Press, W. H. 1992, ApJ, 398, 169
- Sanders, D. B., Salvato, M., Aussel, H., et al. 2007, ApJS, 172, 86
- Schlafly, E. F., & Finkbeiner, D. P. 2011, ApJ, 737, 103
- Schlegel, D. J., Finkbeiner, D. P., & Davis, M. 1998, ApJ, 500, 525
- Schneider, D. P., Richards, G. T., Hall, P. B., et al. 2010, AJ, 139, 2360
- Scott, J. E., Kriss, G. A., Brotherton, M., et al. 2004, ApJ, 615, 135
- Shakura, N. I., & Sunyaev, R. A. 1973, in IAU Symposium, Vol. 55, X- and Gamma-Ray Astronomy, ed. H. Bradt & R. Giacconi, 155

- Shakura, N. I., & Sunyaev, R. A. 1976, MNRAS, 175, 613
- Shang, Z., Brotherton, M. S., Green, R. F., et al. 2005, ApJ, 619, 41
- Shang, Z., Brotherton, M. S., Wills, B. J., et al. 2011, ApJS, 196, 2
- Shen, Y., Richards, G. T., Strauss, M. A., et al. 2011, ApJS, 194, 45
- Silk, J., & Rees, M. J. 1998, A&A, 331, L1
- Skrutskie, M. F., Cutri, R. M., Stiening, R., et al. 2006, AJ, 131, 1163
- Sobolewska, M. A., Siemiginowska, A., & Źycki, P. T. 2004a, ApJ, 608, 80
- . 2004b, ApJ, 617, 102
- Sprayberry, D., & Foltz, C. B. 1992, ApJ, 390, 39
- Steffen, A. T., Strateva, I., Brandt, W. N., et al. 2006, AJ, 131, 2826
- Stern, J., & Laor, A. 2012, MNRAS, 2870
- Stern, J., Laor, A., & Baskin, A. 2014, MNRAS, 438, 901
- Sulentic, J. W., Bachev, R., Marziani, P., Negrete, C. A., & Dultzin, D. 2007, ApJ, 666, 757
- Sun, W.-H., & Malkan, M. A. 1989, ApJ, 346, 68
- Telfer, R. C., Kriss, G. A., Zheng, W., Davidsen, A. F., & Tytler, D. 2002, ApJ, 579, 500
- Tolea, A., Krolik, J. H., & Tsvetanov, Z. 2002, ApJ, 578, L31
- Trumpler, R. J. 1930, Lick Observatory Bulletin, 14, 154
- Turnshek, D. A., Grillmair, C. J., Foltz, C. B., & Weymann, R. J. 1988, ApJ, 325, 651
- Urry, C. M., & Padovani, P. 1995, PASP, 107, 803
- Vanden Berk, D. E., Richards, G. T., Bauer, A., et al. 2001, AJ, 122, 549
- Vanden Berk, D. E., Shen, J., Yip, C., et al. 2006, AJ, 131, 84
- Vasudevan, R. V., & Fabian, A. C. 2007, MNRAS, 381, 1235
- Vestergaard, M., & Osmer, P. S. 2009, ApJ, 699, 800
- Vestergaard, M., & Peterson, B. M. 2006, ApJ, 641, 689
- Wang, H., Wang, T., Zhou, H., et al. 2011, ApJ, 738, 85
- Wang, J.-G., Dong, X.-B., Wang, T.-G., et al. 2009, ApJ, 707, 1334
- Weymann, R. J., Morris, S. L., Foltz, C. B., & Hewett, P. C. 1991, ApJ, 373, 23
- Wilkes, B. J., Tananbaum, H., Worrall, D. M., et al. 1994, ApJS, 92, 53
- Wills, B. J., & Browne, I. W. A. 1986, ApJ, 302, 56
- Woo, J.-H., Schulze, A., Park, D., et al. 2013, ApJ, 772, 49
- Woo, J.-H., Treu, T., Barth, A. J., et al. 2010, ApJ, 716, 269
- Worseck, G., & Prochaska, J. X. 2011, ApJ, 728, 23
- Wright, E. L., Eisenhardt, P. R. M., Mainzer, A. K., et al. 2010, AJ, 140, 1868

- Wyder, T. K., Martin, D. C., Schiminovich, D., et al. 2007, ApJS, 173, 293
- Yip, C. W., Connolly, A. J., Vanden Berk, D. E., et al. 2004, AJ, 128, 2603
- York, D. G., Adelman, J., Anderson, Jr., J. E., et al. 2000, AJ, 120, 1579
- York, D. G., vanden Berk, D., Richards, G. T., et al. 2005, in IAU Colloq. 199: Probing Galaxies through Quasar Absorption Lines, ed. P. Williams, C.-G. Shu, & B. Menard, 58
- York, D. G., Khare, P., Vanden Berk, D., et al. 2006, MNRAS, 367, 945
- Yu, Y., & Meng, X.-L. 2011, Journal of Computational and Graphical Statistics, 20, 531
- Zakamska, N. L., Strauss, M. A., Krolik, J. H., et al. 2003, AJ, 126, 2125
- Zdziarski, A. A., Johnson, W. N., Done, C., Smith, D., & McNaron-Brown, K. 1995, ApJ, 438, L63

## Appendix A: Bayesian Model

In the Bayesian framework, the fit parameters for a model are not assumed to be fixed value, but instead, these parameters are assumed to come from some probability distribution. Bayes' theorem tells us how to express this probability distribution in terms of the likelihood of the *data* given a set of model parameters and any prior information we have about the model parameters. Applying Bayes' theorem to a toy model that has a set of  $n$  model parameters,  $\vec{\phi} = \{\phi_0, \phi_1, \dots, \phi_n\}$ , and measured data,  $D$ , gives:

$$P(\vec{\phi}|D) \propto P(\vec{\phi})P(D|\vec{\phi}) \quad (\text{A.1})$$

Or in words: the posterior distribution for  $\vec{\phi}$  is proportional to the prior distribution of  $\vec{\phi}$  times the likelihood of the data, given  $\vec{\phi}$ .

In hierarchical Bayes, the prior distribution,  $P(\vec{\phi})$ , is not known or assumed beforehand, but instead is a function of another set of  $m$  parameters,  $\vec{\theta} = \{\theta_0, \theta_1, \dots, \theta_m\}$ , known as hyperparameters. This leads to the joint posterior distribution for  $\vec{\phi}$  and  $\vec{\theta}$  of:

$$P(\vec{\theta}, \vec{\phi}|D) \propto P(\vec{\theta})P(\vec{\phi}|\vec{\theta})P(D|\vec{\phi}) \quad (\text{A.2})$$

where  $P(\vec{\theta})$  are the hyperpriors that are placed on  $\vec{\theta}$ .

With the posterior distribution defined by Bayes' theorem, Markov Chain Monte Carlo (MCMC) sampling methods can be used to simulate data points drawn from it, providing the full joint probability distribution for all parameters and hyperparameters given the observed data. When using a hierarchical model, care must be taken to make sure that the sampling method is self consistent; that is, when  $\vec{\phi}$  changes,  $\vec{\theta}$  changes to match the new distribution of  $\vec{\phi}$ . This can be achieved by using a Gibbs sampler (Gelman & Hill, 2006).

### A.1 Gibbs Sampling

In Gibbs sampling, sample points are drawn from the posterior by drawing from the *conditional probabilities* for each parameter (or set of parameters) in turn. These conditional probabilities are found by taking the posterior distribution and holding all but one (or a small set of) parameters fixed. As an example, take a model that has two parameters,  $A$  and  $B$ , being estimated. Given initial values,  $A_0$  and  $B_0$ , the Gibbs sampler updates these values by alternating between drawing a new  $A$  value from the posterior holding  $B$  fixed,  $A_{i+1} \sim P(A|B_i, D)$ , and then drawing a new  $B$  value from the posterior holding  $A$  fixed at its new value,  $B_{i+1} \sim P(B|A_{i+1}, D)$ , where “~” is read “distributed as”. After a sufficient number of iterations, known as the burn-in period, each step of the Gibbs sampler will simulate a draw from the joint distribution  $P(A, B|D)$ .

For some models these conditional probabilities have known distributions. One such model is estimating the mean,  $\mu$ , and standard deviation,  $\sigma$ , when given a set of  $n$  normally distributed observations  $\vec{x}$ . The conditional probabilities from this model are:

$$P(\mu|\sigma, \vec{x}) \sim N\left(\frac{\sum_i^n x_i}{n}, \frac{\sigma}{\sqrt{n}}\right) \quad (\text{A.3})$$

$$P(\sigma^2|\mu, \vec{x}) \sim \frac{(n-1) \sum_i^n (x_i - \mu)^2}{n} \frac{1}{\chi_{n-1}^2} \quad (\text{A.4})$$

where  $N(a, b)$  is a normal distribution with mean  $a$  and standard deviation  $b$ , and  $\chi_{n-1}^2$  is a chi-square random variable with  $n-1$  degrees of freedom (Gelman & Hill, 2006).

When the conditional probability cannot be represented by a known distribution, draws can still be simulated by using another MCMC sampler. Typically, a Metropolis-Hastings (MH; Hastings,

1970) step is used, resulting in a method called Metropolis-within-Gibbs sampling (Metropolis et al., 1953), but *any* MCMC sampler can be used to draw from the conditional. In this work, we use the affine invariant MCMC ensemble sampler `emcee`, described in Foreman-Mackey et al. (2013)<sup>1</sup>, to form an `emcee`-within-Gibbs sampler. This sampler efficiently samples distributions with degenerate variables, and it only has one tuning parameter, unlike the MH sampler, which has one tuning parameter for each fit parameter and is slow to converge for degenerate variables.

The `emcee` sampler works by simulating  $N$  simultaneous draws from the conditional distribution, where each draw is known as a walker. The proposal distribution for each walker is based on the current positions of all the remaining walkers. In each step, a new position is proposed for each walker by “walking” it along the vector connecting it to another randomly selected walker. If the likelihood of the conditional is higher at this proposed value, the step is accepted; if it is not, it is accepted with a probability related to the ratio of the likelihoods at its current position and the proposed position (see Foreman-Mackey et al. (2013) for more details). Because this sampler uses an ensemble of walkers, at every step of the algorithm it produces  $N$  estimates for each parameter.

To form a `emcee`-within-Gibbs sampler some care must be taken in choosing the number of walkers,  $N$ , needed. The general rule of thumb is  $N$  should be larger than twice the number of parameters being estimated. With hierarchical models, the number of parameters can grow to be very large. If every parameter was estimated in the same step (i.e. when not using Gibbs sampling) then  $N$  would be too large to make the `emcee` sampler a practical solution. When placing the `emcee` sampler within a Gibbs step, the number of parameters being estimated in each conditional is small (3 for the model considered here), meaning  $N$  only needs to be larger than twice the dimensionality of the largest conditional, bringing  $N$  down to a reasonable size.

## A.2 The Model

For this paper we create a hierarchical model we use to estimate the slopes and curvatures for each quasar in our sample. We start by modeling each observed  $\Delta m_{ij}$  as coming from a Student’s  $t$ -distribution with 3 degrees of freedom centered on the model given by Equation 4.1(b), with components  $\vec{m}_0$ ,  $2.5\vec{\Delta}(\alpha_\lambda)$ , and  $E(B - V)$ , and with a width given by the observed measurement error,  $\sigma_{ij}$ , combined with an unknown term  $S$  representing the error in the modal magnitudes:

$$\Delta m_{ij} \sim T(3, \Delta m_{ij}^{\text{model}}, \sqrt{\sigma_{ij}^2 + S^2}), \quad (\text{A.5})$$

where the  $t$ -distribution is:

$$T(\nu, \mu, \sigma) \propto \frac{1}{\sqrt{\nu\pi}\sigma} \left(1 + \frac{\mu^2}{\sigma^2\nu}\right)^{-(\nu+1)/2}, \quad (\text{A.6})$$

$\Delta m_{ij}^{\text{model}}$  is the model for  $\Delta m$  given in Equation 4.1(b),  $S$  can be thought of as a “calibration” error in our model,  $i$  is used to index each quasar, and  $j$  is used to index each filter. We use a Student’s  $t$ -distribution instead of a normal distribution to make our model more robust against outliers. A value of  $\nu = 3$  degrees of freedom implies  $\sim 6\%$  of the data are outliers by more than  $3\sigma$  (Kelly et al., 2012).

With the likelihood of our data given the model defined, we next model the prior distributions for our set of fit parameters  $\phi = \{\vec{m}_0, 2.5\vec{\Delta}(\alpha_\lambda), E(B - V)\}$ . The collection of powerlaw slopes,  $2.5\vec{\Delta}(\alpha_\lambda)$ , are modeled as coming from a normal distribution with unknown mean,  $\mu_\alpha$ , and standard deviation,  $\sigma_\alpha$ . This distribution was chosen since we expect to see just as many intrinsically blue as intrinsically red quasars. Unlike Hopkins et al. (2004) we do not assume  $\mu_\alpha$  is zero; this way we account for differences between the *observed* modal quasar and the necessarily bluer *intrinsic* modal quasar (i.e. the modal quasar after correcting for dust reddening). We additionally limit the values of  $2.5\vec{\Delta}(\alpha_\lambda)$  to stay in the range  $[-1.25, 5.75]$ , where the lower limit is equivalent to a quasar with

---

<sup>1</sup>python code available at <http://dan.iel.fm/emcee/current/>

$\alpha_\lambda \sim -1.22$  (a very red quasar) and the upper limit is equivalent to a quasar with  $\alpha_\lambda \sim -4$  (an infinite temperature blackbody).

The collection of reddening amounts,  $E(\vec{B} - V)$ , are modeled as coming from exponentially modified Gaussian (EMG) with unknown shape parameters. This distribution is the result of summing together random variables drawn from a normal distribution with mean  $\mu_{\text{dust}}$  and standard deviation  $\sigma_{\text{dust}}$ , and random variables drawn from a exponential distribution with rate parameter  $\lambda_{\text{dust}}$  (smaller values indicate a heavier tail). This is very similar to the half-normal half-exponential distribution Hopkins et al. (2004) found to work well for quasars. As with the  $2.5\Delta(\alpha_\lambda)$  distribution, we do not assume  $\mu_{\text{dust}}$  is zero beforehand.

To normalize our data, we have set the  $i$  band  $\Delta m$  to zero for all quasars. Under this normalization the offset parameters,  $\vec{m}_0$ , will be normally distributed with mean zero and standard deviation  $\sqrt{\sigma_{i\text{band}}^2 + S^2}$ . For our data the observed  $i$  band errors are small compared to  $S$ , allowing us to drop the  $\sigma_{i\text{band}}$  term.

Using these distributions, our priors are:

$$\begin{aligned} m_{0,i} &\sim N(0, S) \\ 2.5\Delta(\alpha_\lambda)_i &\sim N(\mu_\alpha, \sigma_\alpha) \\ E(B - V)_i &\sim N(\mu_{\text{dust}}, \sigma_{\text{dust}}) + E(\lambda_{\text{dust}}) \end{aligned} \quad (\text{A.7})$$

where  $E(\lambda)$  is an exponential distribution with rate parameter  $\lambda$ . To complete defining our model, we place uninformative hyperpriors on the hyperparameters  $\theta = \{\mu_\alpha, \sigma_\alpha, \mu_{\text{dust}}, \sigma_{\text{dust}}, \lambda_{\text{dust}}, S\}$ :

$$\begin{aligned} \mu_\alpha &\sim U(-5, 5) \\ \sigma_\alpha &\sim U(0, 10) \\ \mu_{\text{dust}} &\sim U(-5, 5) \\ \sigma_{\text{dust}} &\sim U(0, 10) \\ \lambda_{\text{dust}} &\sim U(0, 40) \\ S &\sim U(0, 10) \end{aligned} \quad (\text{A.8})$$

where  $U(a, b)$  is a uniform distribution between the values  $a$  and  $b$ .

As written, equation A.5 is dependent on both  $\phi$  and  $\theta$ . Leaving it like this can lead to instabilities in our sampler. These instabilities can be removed by introducing a set of nuisance parameters,  $\delta_{ij}$ , into  $\phi$  that represent the normally distributed noise introduced by  $S$ . Equation A.5 now becomes:

$$\Delta m_{ij} \sim T(3, \Delta m_{ij}^{\text{model}} + \delta_{ij}, \sigma_{ij}) \quad (\text{A.9})$$

and one more prior is added to equation A.7:

$$\delta_{ij} \sim N(0, S) \quad (\text{A.10})$$

### A.3 Conditional Likelihoods

To make use of a Gibbs sampler to estimate both  $\phi$  and  $\theta$ , the conditional likelihoods for each parameter (or set of parameters) need to be found. Taking the model defined in §A.2, several of the

fit parameters have conditionals with analytic forms:

$$\mu_\alpha \sim N\left(\frac{\sum_i^n 2.5\Delta(\alpha_\lambda)_i}{n}, \frac{\sigma_\alpha}{\sqrt{n}}\right) \quad (\text{A.11})$$

$$\sigma_\alpha^2 \sim \frac{(n-1)\sum_i^n (2.5\Delta(\alpha_\lambda)_i - \mu_\alpha)^2}{n} \frac{1}{\chi_{n-1}^2} \quad (\text{A.12})$$

$$S^2 \sim \frac{\sum_i^n \sum_j^m (\delta_{ij} + m_{0,i})^2}{2} \frac{1}{\chi_{nm}^2} \quad (\text{A.13})$$

$$\delta_{ij} \sim N\left(\frac{S^2}{S^2 + \sigma_{ij}^2} (\Delta m_{ij} - \Delta m_{ij}^{\text{model}}), \frac{S^2 \sigma_{ij}^2}{S^2 + \sigma_{ij}^2}\right) \quad (\text{A.14})$$

For the remaining conditionals it is useful to define the probability density functions for the exponentially modified Gaussian distribution and the normal distribution:

$$\begin{aligned} \text{EMG}(x|\mu, \sigma, \lambda) &= \frac{\lambda}{2} \exp\left(\frac{\lambda}{2}(2\mu + \lambda\sigma^2 - 2x)\right) \\ &\quad \text{erfc}\left(\frac{\mu + \lambda\sigma^2 - x}{\sqrt{2}\sigma}\right) \end{aligned} \quad (\text{A.15})$$

$$N(x|\mu, \sigma) = \frac{1}{\sqrt{2\pi}\sigma} \exp\left(-\frac{(x-\mu)^2}{2\sigma^2}\right) \quad (\text{A.16})$$

where erfc is the complementary error function. The remaining conditional probabilities are:

$$\begin{aligned} P(\mu_{\text{dust}}, \sigma_{\text{dust}}, \lambda_{\text{dust}} | E(B-V)) &\propto P(\mu_{\text{dust}})P(\sigma_{\text{dust}}) \\ &\quad P(\lambda_{\text{dust}}) \prod_i \text{EMG}(E(B-V)_i | \mu_{\text{dust}}, \sigma_{\text{dust}}, \lambda_{\text{dust}}) \end{aligned} \quad (\text{A.17})$$

$$\begin{aligned} P(\phi_i | \theta, \vec{\Delta m}_i) &\propto \text{EMG}(E(B-V)_i | \mu_{\text{dust}}, \sigma_{\text{dust}}, \lambda_{\text{dust}}) \\ &\quad N(2.5\Delta(\alpha_\lambda)_i | \mu_\alpha, \sigma_\alpha) N(m_{0,i} | 0, S) \\ &\quad \prod_j T(\Delta m_{ij} | 3, \Delta m_{ij}^{\text{model}} + \delta_{ij}, \sigma_{ij}) \end{aligned} \quad (\text{A.18})$$

By breaking up the conditionals in this manner, the largest number of parameters being estimated in any given `emcee` step is 3. As discussed in §4.1.3, this means a few hundred walkers are sufficient to fully sample the space.

In order to increase the efficiency of our MCMC sampler, we use an Ancillarity-Sufficiency Interweaving Strategy (ASIS) similar to the one used in Kelly (2011) (see also Yu & Meng, 2011). The ASIS works by introducing the following change of variables for Equation A.18:

$$\tilde{\delta}_{ij} = \Delta m_{ij}^{\text{model}} + \delta_{ij} \quad (\text{A.19})$$

$$\tilde{\delta}_{ij} \sim T(3, \Delta m_{ij}^{\text{model}}, S) \quad (\text{A.20})$$

This change allows for a second way of updating the individual fit parameters  $\vec{m}_0$ ,  $2.5\vec{\Delta}(\alpha_\lambda)$ , and  $E(B-V)$  that is not directly dependent on the observed data:

$$\begin{aligned} P(\phi_i | \theta, \tilde{\delta}_{ij}) &\propto \text{EMG}(E(B-V)_i | \mu_{\text{dust}}, \sigma_{\text{dust}}, \lambda_{\text{dust}}) \\ &\quad N(2.5\Delta(\alpha_\lambda)_i | \mu_\alpha, \sigma_\alpha) N(m_{0,i} | 0, S) \\ &\quad \prod_j T(\tilde{\delta}_{ij} | 3, \Delta m_{ij}^{\text{model}}, S) \end{aligned} \quad (\text{A.21})$$

ASIS replaces the update step given by Equation A.18 with the following steps:

1. Update  $\vec{m}_0$ ,  $2.5\vec{\Delta}(\alpha_\lambda)$ , and  $E(\vec{B} - \vec{V})$  using Equation A.18
2. Find  $\tilde{\delta}_{ij}$  using Equation A.19 and the current values for the fit parameters
3. Update  $\vec{m}_0$ ,  $2.5\vec{\Delta}(\alpha_\lambda)$ , and  $E(\vec{B} - \vec{V})$  using Equation A.21
4. Find the new values for  $\delta_{ij}$  associated with these parameters by apply the inverse of the transformation given in Equation A.19

In our analysis we used 200 walkers with a 2000 step burn-in and 400 steps of sampling. In Chapter 4 we refer to  $\theta$  as the population parameters and  $\phi$  as the individual parameters.

## Vita

### **Coleman M. Krawczyk**

#### **Education**

- Drexel University, Philadelphia, Pennsylvania USA
  - Ph.D., Physics, September 2014
  - M.S., Physics, June 2010
- University of Massachusetts at Amherst, Amherst, Massachusetts USA
  - B.S., Astrophysics, May 2008
  - B.S., Mathematics, May 2008

#### **Publications**

- “Dusty Quasars”, 2014
- “Mean Spectral Energy Distributions and Bolometric Corrections for Luminous Quasars”, ApJS, 206, 4, 2013
- “C IV Emission and the Ultraviolet through X-Ray Spectral Energy Distribution of Radio-quiet Quasars”, AJ, 142, 130, 2011
- “The Sloan Digital Sky Survey Quasar Catalog. V. Seventh Data Release”, AJ, 139, 2360, 2010
- “Re-Examining Larson’s Scaling Relationships in Galactic Molecular Clouds”, ApJ, 699, 1092, 2008

#### **Awards**

- NSF Graduate Research Fellowship Program, Honorable Mention, 2009
- Mary Dailey Irvine Prize, 2008

#### **Teaching Experience**

- **Teaching Assistant** *September 2008 to May 2010*

*Autumn 2008 to Spring 2009* – Introductory Physics I–III  
*Autumn 2009 to Spring 2010* – Contemporary Physics I–III

- **Tutor**

*Spring 2006 to Spring 2008* – Astronomy Help Desk

- **Supplemental Instructor** *Spring 2007 to Spring 2008*

*Spring 2007 and 2008* – SI for Techniques of Theoretical Physics  
*Autumn 2008* – SI for Mechanics

#### **Public Outreach**

- **The Franklin Institute** *January 2009 to July 2014*
- **Carver Science Fair** *February 19th, 2014*
- **UMass Science Outreach** *September 2004 to May 2008*

